NONLINEAR APPROXIMATE AEROELASTIC ANALYSIS OF FLAPPING WINGS IN HOVER AND FORWARD FLIGHT

by

Abhijit Gogulapati

**A dissertation submitted in partial fulfillment
of the requirements for the degree of
Doctor of Philosophy
(Aerospace Engineering)
in the University of Michigan
2011**

Doctoral Committee:

**Professor Peretz P. Friedmann, Chair
Professor Carlos E. Cesnik
Associate Professor Luis P. Bernal
Associate Professor Bogdan Epureanu**

To Amma, Nanna, Madhu, and Vidya

ACKNOWLEDGEMENTS

I will be ever grateful to my advisor Prof. Peretz Friedmann for being a friend and a mentor through the various stages of my doctoral studies. His emphases on clarity of thought, quality of research, and thoughtful presentation, have provided valuable lessons that I am unlikely to forget.

I acknowledge support from the Air Force Office of Scientific Research (AFOSR), which sponsored this research through the Multi-University Research Initiative (MURI) grant with Dr. Douglas R. Smith as program director. I am thankful also to Prof. Carlos Cesnik, Prof. Luis Bernal, and Prof. Bogdan Epureanu, for serving on my thesis committee.

I have been fortunate to collaborate with several excellent researchers during the course of this work. I thank them for their vital contributions to this thesis: Dr. Hikaru Aono for generating the CFD based results for the rigid wings; Dr. Patrick Trizila, Dr. Li Liu, and Ashwani Padthe, for the rigid airfoil cases; Eugene Kheng and Paul Davidson for prompt help in conducting experiments on the CAPRAN film; Dr. Satish Chimakurthi for providing results for the isotropic wings; and Dr. Pin Wu and Robert Love from the University of Florida at Gainsville for providing samples and results for the anisotropic wings, material properties, and discussions. Special thanks also go to Prof. Carlos Cesnik, Prof. Anthony Waas, Dr. Hikaru Aono, and

Chang-Kwon Kang for the illuminating discussions and timely inputs that nudged me in the right direction, and Prof. Wei Shyy for his initiative in bringing together several research groups that were working on the flapping wing problem.

It was an absolute pleasure to share the working environment with Dr. Li Liu, Nicholas Lamorte, Ashwani Padthe, Dr. Bryan Glaz, and Eric Muir. I could not have asked for better officemates and thank them for putting up with my 'thinking-out-loud' sessions. Denise Phelps, Suzanne Smith, Cindy Enoch, and Michelle Shepherd, also deserve considerable praise for their ever friendly attitude and making sure the administrative side of things went without incident. Thanks also to Dave McClean for excellent computer-related advice.

I owe a great debt of gratitude to friends - Amit Salvi, Paul Davidson, Christian Heinrich, Nalin Chaturvedi, Shiladitya Basu, and several more - who have made my stay in Ann Arbor so enjoyable, enriching, and memorable. Life was always upbeat and never dull with you around. Finally, to my parents, sister Madhulika, and fiance Vidya, who have been my source of strength throughout this journey: none of this would have been possible without the unconditional support and love you have given me.

TABLE OF CONTENTS

LIST OF FIGURES

Figure

LIST OF TABLES

Table

LIST OF APPENDICES

Appendix

NOMENCLATURE

Symbol	Description
$\mathbf{A},\mathbf{B},\mathbf{a},\mathbf{b},\mathbf{c},\mathbf{d},\mathbf{g}$	Complex numbers
$A_1 - A_{11}$	Coefficients derived in the aerodynamic formulation
A_f, B_f	Filter coefficients
A_w	Wing area
$\boldsymbol{dA}_{sp}$	Instantaneous area vector in the (X_{SP}, Y_{SP}, Z_{SP}) coordinate system
a	Distance between pitch axis of airfoil and mid-chord, shown in Figure 3.8
$\mathbf{B}_L, \mathbf{B}_{NL}$	Transformation matrices derived from shape function matrices
b	Semi-chord
$\boldsymbol{C}$	Tangent stiffness matrix or tensor of material constants
C_{ikjl}	Components of the tangent stiffness matrix
C_D	Drag coefficient
C_F	Force coefficient
C_L	Lift coefficient
C_M	Moment coefficient
C_T	Thrust coefficient
c_r	Root chord
c	Airfoil chord; function of the span location
D	Drag
$\boldsymbol{E}_{con}$	Residual vector due to constraints
${}^t\mathbf{E}_{res}$	Residual vector at time t
E	Elastic modulus
E_{ij}	Elastic moduli of an orthotropic material
$\hat{\mathbf{e}}, \hat{\boldsymbol{e}}$	Cartesian unit vectors; subscript identifies the axis
$\hat{\mathrm{e}}_x, \hat{\mathrm{e}}_x, \hat{\mathrm{e}}_z$	Cartesian components of $\hat{\mathbf{e}}$
e_{ij}	Cartesian components of the Cauchy strain tensor
$\mathbf{F}_\sigma$	Force vector obtained from stress in the equations of motion

Symbol	Description
$\boldsymbol{F}$	Force, complex number
${}^{t}\mathbf{F}_{in}$	Vector of internal forces at time t
$\boldsymbol{F}_{sp}$	Force vector in the (X_{SP}, Y_{SP}, Z_{SP}) coordinate system
F_h, F_v	Components of aerodynamic force in the horizontal and vertical directions
$F_{inertial}$	Virtual work done by inertial forces
F_h, F_v	Components of the aerodynamic forces in the horizontal and vertical directions
f	Flapping frequency
G_{ij}	Shear moduli of an orthotropic material
$\boldsymbol{H}$	Matrix of displacement gradients
h	Plunge degree of freedom
$\boldsymbol{I}$	Impulse of vorticity, complex number
$\mathscr{I}$	Imaginary part
I_m	Moment of impulse of vorticity
i, j	Indices
$\boldsymbol{K}_{con}$	Contribution of constraints to the global tangent stiffness matrix of the structure
$\boldsymbol{K}_{ij}$	for $i = 1,2$ and $j = 1,2$. Components of the $\boldsymbol{K}_{con}$
$\mathbf{K}, \mathbf{K}_L, \mathbf{K}_{NL}$	Stiffness matrices in the equation of motion
k_{pe}	Penalty stiffness
k_λ	A scaling coefficient in the augmented Lagrange multiplier method
L	Lift
L_C	Circumference of the airfoil contour
L_{wk1}, L_{wk2}	Lengths of the shears layers emanating from the airfoil
l	Lead lag degree of freedom
l_0	Lead lag amplitude
M	Aerodynamic Moment
m_f	Order of the filter
$\boldsymbol{N}$	Shape function matrices used to interpolate displacements
N_θ	Airfoil discretization
$N_{section}$	Number of wing sections
N_t	Number of time steps per cycle

Symbol	Description
N_v	Number of shed vortices in the system
$n_{wksubit}$	Number of wake sub-iterations
n_c	Airfoil discretization in the structural dynamic model
n_{press}	p_{limit}/p_{ref}
O, O_w	Stationary and wing-fixed Cartesian coordinate systems
O_1, O_2	Intermediate orientations of the wing fixed coordinate system
$\mathcal{O}$	Order of magnitude
p	Local static pressure on the airfoil
p_∞	Free stream pressure
$p_{applied}$	Pressure that is applied on the wing
$p_{computed}$	Pressure that is computed using the unsteady Bernoulli principle
p_{limit}	An upper bound value for pressure
p_{ref}	Reference pressure
$\boldsymbol{q}$	Velocity on the normal cylinder
$\boldsymbol{q_c}$	Vector of constraints in the augmented Lagrange multiplier method
$\hat{\boldsymbol{R}}$	Rotation tensor
$\tilde{\mathbf{R}}$	Vector associated with virtual work due to distributed body forces and surface tractions
Re	Reynolds number
$\mathscr{R}$	Real part
$\tilde{R}$	Integral associated with virtual work due to distributed body forces and surface tractions
R_0	Radius of the circle in the complex plane
R_j	Radial location of j^{th} wing section
$\hat{R}_{ij}$	Components of the rotation tensor
R_{span}	Wing span
r_c	Vortex core radius
r_v	Distance between shed vortex and point of interest
$\underline{r}_v$	Normalized distance between shed vortex and point of interest
S_{ij}	Cartesian components of the second Piola-Kirchoff (PK2) stress tensor
S	Area

Symbol	Description
s	Arc coordinate
s_0	Origin of the curve that is used to integrate along the airfoil
s_{wk1}, s_{wk2}	Arc coordinates of the shear layers emanating from the airfoil
T	Thrust
t	Time
t_h	Thickness
Δt	Time increment
t_v	Age of a shed vortex
$\underline{t}_v$	Non-dimensional age of a shed vortex
$\boldsymbol{U}_0$	Translation velocity of the non-rotating coordinate system
$\boldsymbol{U}_I$	Free stream velocity vector on the flattened normal cylinder, shown in Figure 3.8: $\boldsymbol{U}_I = u_I \boldsymbol{e}_{\xi^I} + v_I \boldsymbol{e}_{\eta^I}$
$\boldsymbol{U}_\infty$	Free stream velocity vector
U_I	Magnitude of $\boldsymbol{U}_I$
U_{ref}	Reference speed
U_{tip}	Maximum tip speed
U_∞	Magnitude of $\boldsymbol{U}_\infty$
$\boldsymbol{u}$	Vector of displacements
$\boldsymbol{u_c}$	Vector of constraints
$\Delta \boldsymbol{u}$	Vector of incremental displacements
u_∞, v_∞	Components of free stream velocity resolved parallel and normal to the stroke plane
u_E, v_E	Components of free stream velocity in the vortex wake model
u_I, v_I	Components of free stream velocity on the airfoil-wake plane, shown in Figure 3.8
$\underline{\mathbf{u}}$	Vector of nodal displacements from time t to $t + \Delta t$
$\Delta \underline{\mathbf{u}}$	Increments in $\underline{\mathbf{u}}$ used in the Newton-Raphson iteration from time t to $t + \Delta t$
V_w	Wing volume
v_{ind}	Velocity induced by a vortex
v_r	Radial component of fluid velocity on the complex circle
v_ξ, v_η	Airfoil velocities, measured in the $\xi - \eta$ coordinate system

Symbol	Description
v_θ	Tangential component of fluid velocity on the complex circle
$\Delta v_\xi^{flex}, \Delta v_\eta^{flex}$	Incremental components of velocity due to airfoil flexibility, measured in the $\xi - \eta$ coordinate system
Δv	Incremental velocity
(X_{SP}, Y_{SP}, Z_{SP})	Coordinate system fixed to the stroke plane, shown in Figure 3.5
(X_w, Y_w, Z_w)	Wing fixed coordinate system, shown in Figure 3.2
$\boldsymbol{x}, \boldsymbol{x}_w$	Position vectors in stationary and wing-fixed Cartesian coordinate systems
$\boldsymbol{x}_{sp}$	Instantaneous position vector of a point on the wing in the (X_{SP}, Y_{SP}, Z_{SP}) coordinate system
$y_{filtered}, y_{unfiltered}$	Filtered and unfiltered signals
$\boldsymbol{z}_{wk}^v$	Coordinate of a shed vortex on the complex plane

Greek Symbols

Symbol	Description
α	Pitch angle, counterclockwise positive
α_0	Pitch amplitude
α_{fs}	Angle between $\boldsymbol{U}_I$ and $\boldsymbol{e}_{\xi^I}$, shown in Figure 3.8, clockwise positive
α_r	Feathering angle in hawkmoth kinematics
α_{sj}, α_{cj}	Fourier coefficients in hawkmoth kinematics
α_{tot}	Instantaneous angle of attack
α_{zll}	Zero lift angle of attack
β	Flap angle
β_0	Flap amplitude
β_j	Angle used in computation of zero lift angle and camber
β_{sp}	Angle between stroke plane and free stream velocity vector
Γ	Circulation
Γ_{fs}	Circulation due to free stream and instantaneous angle of attack
Γ_0	Quasi-steady circulation

Symbol	Description
$d\Gamma$	Circulation of a discrete vortex
γ	Vorticity
γ_b	Bound vorticity
γ_{fs}	Component of vorticity due to free stream and instantaneous angle of attack
γ_{us}	Component of vorticity due to airfoil velocities
γ_{wi}	Component of vorticity that is induced by the wake
ϵ_Γ	Circulation limit
$\boldsymbol{\epsilon}$	Vector of mid-plane strains
$\boldsymbol{\varepsilon}$	$\tau - \iota\sigma$
$\epsilon_{ij}, \varepsilon_{ij}$	Cartesian components of the Green-Lagrange strain tensor
$\boldsymbol{\zeta}$	$\xi + \iota\eta$
Θ_r	Elevation angle in hawkmoth kinematics
$\Theta_0, \Theta_{sj}, \Theta_{cj}$	Fourier coefficients in hawkmoth kinematics
θ	Angular coordinate on the circle in the complex plane
μ	Advance ratio
ν	Poisson's ratio
ν_∞	Kinematic viscosity of the fluid
ξ, η	Coordinates in an airfoil fixed frame; superscript identifies coordinate system
$\boldsymbol{\lambda}$	Lagrange multipliers in the constraint equations
Π_{res}	Energy functional
π	3.14259
ρ	Density of the material
ρ_∞	Free stream density
$\boldsymbol{\sigma}$	Vector of stresses in a composite element
σ	Camber parameter
σ_{ij}	Components of the Cauchy stress tensor
ς	Dummy variable representing angular coordinate
τ	Thickness parameter
$\boldsymbol{\Phi}_c$	Matrix of constraints
Φ_r	Sweep angle in hawkmoth kinematics
$\Phi_0, \Phi_{sj}, \Phi_{cj}$	Fourier coefficients in hawkmoth kinematics
ϕ	Velocity potential

Symbol	Description
φ	Angular position of a vortex in $\xi^{fa} - \eta^{fa}$
$\tilde{\varphi}$	Angular position of a vortex or airfoil section on the normal cylinder, measured in $X_{SP} - Y_{SP}$
φ_α	Phase
$\imath$	$\sqrt{-1}$
$\boldsymbol{\zeta}$	Coordinate of a point on the flattened normal cylinder, measured in an airfoil coordinate system
$\boldsymbol{\psi}$	Rotation vector
$\Delta\boldsymbol{\psi}$	Incremental rotation vector
ψ	Magnitude of rotation
ω	Circular frequency
$\boldsymbol{\chi}$	Vector of mid-plane curvatures in the material model

Subscripts

Symbol	Description
$(\,)\big\|_{aero}$	Quantity computed during aerodynamic analysis
$(\,)\big\|_{inviscid}$	Inviscid quantity
$(\,)\big\|_{viscous}$	Viscous quantity
$(\,)_b$	Airfoil bound quantity
$(\,)_{edge}$	Quantity corresponding to leading or trailing edge of the airfoil
$(\,)_{fs}$	Free stream component
$(\,)_{latest}$, $(\,)_{previous}$	Latest and previously shed vortices
$(\,)_r$	Radial component on the circle
$(\,)\big\|_{struc}$	Quantity applied on the structure
$(\,)_{us}$	Component calculated from airfoil velocities
$(\,)_{wi}$	Wake induced component
$(\,)_{wk1}$	Corresponds to vortices shed from the trailing edge
$(\,)_{wk2}$	Corresponds to vortices shed from the leading edge
$(\,)_{wk}$	Corresponds to all shed vortices
$(\,)_\theta$	Angular component on the circle

Superscripts

Symbol	Description
$\dot{(\ )}, \ddot{(\ )}$	Derivatives with respect to time
$\bar{(\ )}$	Averaged quantity
$(\ )^*$	Complex conjugate
$(\ )^A$	Quantity in the coordinate system whose origin is at leading edge of the airfoil
$(\ )^{af}$	Property of an airfoil
$(\ )^{fa}$	Quantity in the coordinate system whose origin is at center of rotation of the airfoil.
$(\ )^{flex}$	Quantity corresponding to a flexible airfoil
$(\ )^I$	Quantity in the stationary coordinate system fixed to the normal cylinder
$(\ )^{nr}$	Quantity in the non-rotating coordinate system
$(\ )^{rigid}$	Quantity corresponding to a rigid airfoil
$(\ )^T$	Transpose
$(\ )^t$	Quantity at time t

Miscellaneous symbols

Symbol	Description
$\lvert\ \rvert$	Absolute value of a complex number
$\lVert\ \rVert$	Magnitude or L2 norm of a vector

CHAPTER I

Introduction, Literature Review, and Objectives

During the last 15 years, there has been considerable interest in micro air vehicles (MAVs) aimed at several low altitude, short duration, civilian and military missions [1]. Based on operational requirements, MAVs typically have maximum geometric dimensions of 15 cm, maximum weight of 100 grams, and an endurance of 30 min at low forward flight speeds (< 18 m/s) [2]. The next generation MAVs, called nano air vehicles (NAVs), are envisioned to have maximum geometric dimensions of 8 cm and weight of 20 g. The specifications of MAVs and NAVs places them in a low Reynolds number regime ($\mathcal{O}(10^2) < \text{Re} < \mathcal{O}(10^4)$) that is shared by smaller birds and larger insects as depicted in Figure 1.1.

1.1 Existing Micro Air Vehicles

Existing MAVs may be based on fixed, rotary, or flapping wings [1]. While fixed and rotary wing MAVs benefit from available fixed and rotary wing aircraft technologies, flapping wing MAVs (FWMAVs) are fundamentally different and are inspired from biological flyers such as insects, hummingbirds, and small bats.

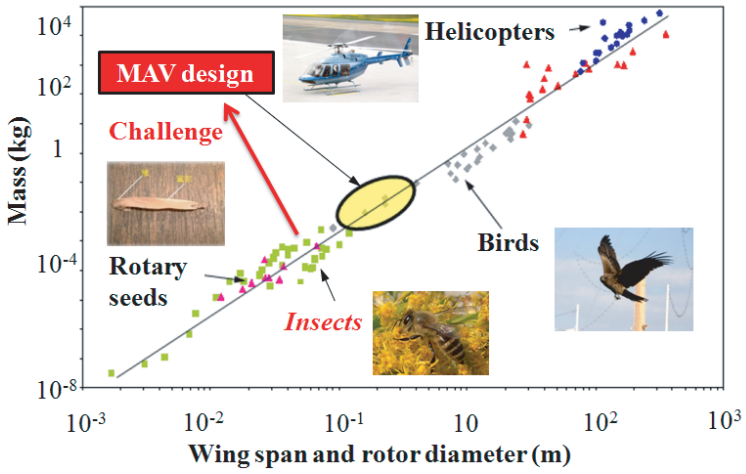

Figure 1.1: Insect, birds, and MAVs [3]

Fixed Wing Designs

The development of fixed wing MAVs has been significantly faster than rotary and flapping wing MAVs due to the simplicity introduced by decoupling the thrust and lift generating components in the vehicle. The success of several conventional designs [1], such as the Black Widow [4] and the MicroSTAR [1], has spurred the development of advanced designs that benefit from aeroelastic tailoring [5] or have improved low speed capabilities [6]. Fixed wing designs are incapable of hovering flight and have limited maneuverability in confined spaces; this has generated interest in hover capable designs based rotary and flapping wings.

Rotary Wing Designs

A limited number of rotary wing MAVs (RWMAVs), such as the MICROR [7], mesicopter [8], and the Hoverfly [1], have demonstrated hover endurance of 10 min

[1] http://www.janes.com/articles/Janes-Unmanned-Aerial-Vehicles-and-Targets/BAE-Systems-MicroSTAR-United-States.html

with no payload. The development of rotary wing designs has been impeded due to several factors associated with the aerodynamic environment of micro rotors, such as dominant boundary layers and separated flow [7, 9–11], due to which RWMAVs suffer from lower lift-to-drag ratio and increased profile power losses compared to conventional helicopters. The low hover efficiency of existing micro rotors indicates that the aerodynamic mechanisms used by conventional rotors are less effective at low Reynolds numbers, highlighting a need for unconventional design strategies.

Flapping Wing Designs

Biological flyers, which have exceptional flight capabilities, are based exclusively on flapping wings. The goal of developing MAVs that offer the best performance at low Reynolds number has led to considerable interest in bio-inspired FWMAVs.

Based on wing kinematics, FWMAVs may be broadly classified as ornithopters and insect-based designs. Ornithopters, which are bird-like, utilize wing flapping primarily for propulsion and the lift is generated due a combination of forward speed and wing flapping. Consequently, ornithopters cannot hover. On the other hand, insects flap their wings in a nearly horizontal plane and execute large changes in wing pitch to produce lift in the absence of forward velocity. Similar wing motions are observed in hover capable birds such as thrips and hummingbirds. Thus, insect-based designs represent hover-capable and highly maneuverable solutions for FWMAVs.

Numerous FWMAVs are in currently in development; some examples include the ornithopter Microbat [12], and hover capable concepts such as the Mentor [13], the Delfly [14], and the Microrobotic fly [15]. While several hover capable concepts have demonstrated flight, the utility of these designs in realistic missions has been severely limited due to low force generation capacity and hover endurance (< 5 min). This has motivated research on understanding and improving the aerodynamic performance of bio-inspired wings.

A Comparison of Rotary and Flapping Wings

Rotary and flapping wing vehicles represent competing hover capable designs for MAV missions; however, a comparative evaluation of these vehicles has received limited attention. Preliminary comparisons of the power requirements of micro rotors and representative flapping wings were presented in Refs. [16, 17]. The induced and profile power were computed using available data for micro rotors, aerodynamic calculations for flapping wings using an unsteady panel method [16], and geometric scaling laws [17]. Calculations indicate that power requirements of the rotary and flapping wing vehicles are somewhat similar. However, these studies [16, 17] highlighted the simplicity of the analysis tools used, and emphasized that refined aerodynamic analysis tools are needed to draw meaningful quantitative comparisons.

1.2 The Aeroelastic Analysis of Flapping Wings

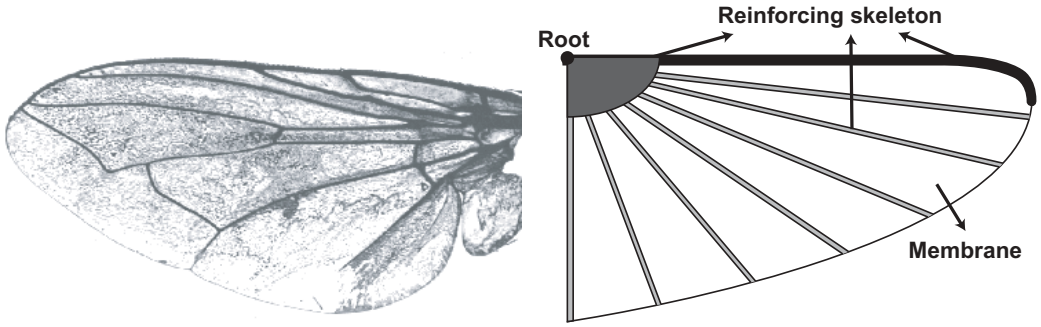

Figure 1.2: Insect and bio-inspired wings

Improving the aerodynamic performance of flapping wings is essential to the development of hover capable FWMAVs. Practical bio-inspired wings, which are based on insect wings as depicted in Figure 1.2, are expected to be light-weight anisotropic constructions that deform during flight. Therefore, the design of bio-inspired wings based

on aeroelastic considerations is an important goal; since designs that benefit from flexibility are preferred, a crucial step in achieving this goal involves understanding the influence of wing flexibility on the performance of flapping wings. The aeroelastic problem associated with flapping wings involves several kinematic, structural, and aerodynamic variables. Computational approaches, which allow a more rapid exploration of the parameter space, are better suited for this problem than experimental approaches. Therefore, the emphasis of this dissertation is on the aeroelastic analysis of flapping wings using computational tools. The important structural and aerodynamic considerations for flapping wing problems, which influence the selection of modeling tools, are identified in this section.

1.2.1 Structural Dynamic Considerations

Typical bio-inspired wings, composed of membrane reinforced by a skeleton as depicted in Figure 1.2, are actuated at the root and deform during flapping. Therefore, the structural dynamic modeling of flapping wings requires the treatment of wing kinematics combined with the flexibility in anisotropic wings.

Wing Kinematics

Experiments on hover capable biological flyers [18–26], where the wings and bodies of flyers are tracked using high speed photo or video equipment, show that the wings are actuated using a time dependent rotation that is imposed at the root. The kinematics, typically represented using Euler angles [18–26], may be described as the combination of a predominant flapping or sweep motion that describes a stroke plane (SP), a feathering motion that produces wing pitch, and a comparatively small elevation motion that describes the movement of the feathering axis out of the SP as indicated in Figure 1.3. Each flapping cycle is composed of two translatory strokes, called the upstroke and downstroke, and two rotations, called supination and

pronation, respectively. In particular, hover kinematics are characterized by a nearly horizontal SP and large changes in the wing pitch angle.

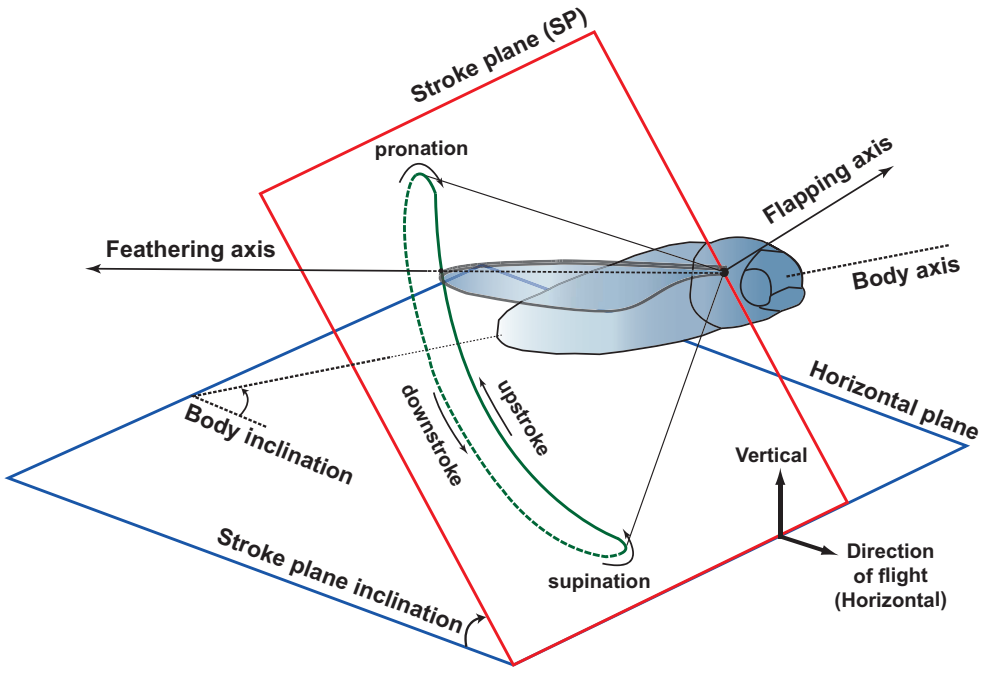

Figure 1.3: Insect flapping stroke

Note that the kinematic data of live flyers are obtained by tracking, and subsequently averaging, the motions of various wing sections. Therefore, the measured stroke amplitudes include the effect of wing flexibility. The data obtained from flyers in hover and forward flight [19–21, 26] indicates: (1) the flapping frequency, which is typically specific to a given flyer, is nearly constant (variation $< 5\%$) for the range of kinematics exhibited by the flyer; (2) the flapping amplitude decreases with increase in forward flight speed; however the decrease is minor ($< 15\%$); and (3) the SP and body inclinations, indicated in Figure 1.3, increase and decrease respectively with increase in forward flight speed. These trends suggest that a transition from hover to forward flight includes tilting the SP while flapping at constant frequency.

Wing Flexibility

Insect wings, composed of veins and membranes, are known to undergo moderate-to-large flexible deformation during flight [27]. Preliminary attempts to assess the importance of flexibility in biological wings, based on simple physical models [28] and experiments using insect wings [29], indicate that inertia loads are important. Reference [28] estimated the bending moment acting at the root of insect wings assuming that the aerodynamic loads are equal to the weight of the insect. An important finding of this study [28] was that a dominant component of the loading on biological flapping wings is due to inertia loads. Experiments [29], conducted using hawkmoth wings that were actuated using representative hover kinematics, showed that the spatial and temporal deformation patterns of wings in air were identical to those in helium. Since the densities of air and helium are substantially different, this observation implies that the effect of aerodynamic loads on the deformation pattern may be negligible. The findings of Refs. [28, 29] were corroborated by the flapping tests in air and vacuum using bio-inspired wings [30]. Wings composed of membranes reinforced by metal frames were actuated using a combined flap-pitch motion up to a frequency of 12 Hz [30]. Measurements, using a load cell at the root, showed that aerodynamic loads were small compared to inertia loads.

These studies [28–30], which highlight the importance of inertia loads, indicate that the development of accurate structural dynamic models is essential for the aeroelastic analysis of flapping wings. In particular, the treatment of moderate-to-large deformation of anisotropic flapping wings is an important consideration.

1.2.2 Unsteady Aerodynamic Mechanisms

A significant portion of the research on hover capable flapping wing vehicles has focused on understanding the mechanisms that generate unsteady aerodynamic forces. This research [2, 31–37] has identified leading edge vortices (LEVs), clap and fling,

wing rotation, and wake capture, as the primary force generating mechanisms. The following summary of these mechanisms is based on the descriptions provided in Ref. [37].

Leading edge vortices are formed following the separation of flow from the leading edge (LE) of a flapping wing. Stable LEVs, which form over the span and remain attached to the wing during the flapping stroke, have been observed for several biological flyers in hover and low speed forward flight as well as on rigid scaled insect and representative flapping wings undergoing hover kinematics. Experimental investigations using the rigid scaled insect wings show that stable LEVs are formed for Reynolds numbers between $\mathcal{O}(10^2)$ and $\mathcal{O}(10^4)$, which represents the range relevant to FWMAV flight. These LEVs are stabilized by a variety of mechanisms which include spanwise flow and downwash due to tip vortices. The presence of dominant LEVs for a wide range of kinematics, wing configurations, and Reynolds numbers, has led to the hypothesis that LEVs are the primary unsteady aerodynamic force generating mechanism in hover capable flyers.

The clap and fling, which is modified to a clap and peel for flexible wings, is a two step kinematic pattern that is employed by various insects, either during regular flight or rapid maneuvers, to increase the force output at the beginning or ends of the stroke. This mechanism involves clapping the wings together, which produces a downward jet, followed by flinging the wings open, which augments the circulation of the LEV that is formed during the fling.

Rapid wing rotation, which occurs in most insect wings at the end of each flapping stroke, has a two fold effect on the generation of aerodynamic forces: (1) the rapid rotation increases the quasi-steady (wake-independent) circulation developed by the wing; (2) the phase difference between the wing translation and rotation influences the extent of the wake capture.

Wake capture, which occurs immediately following stroke reversal, is an unsteady force augmentation mechanism that involves the interaction of a wing with the LEVs generated during the previous cycle. The extent and effectiveness of wake capture depends on the wing configuration, kinematics, and Reynolds number. However, no clear trends have been identified.

The work presented in this dissertation examines the aerodynamic and aeroelastic performance of an isolated flapping wing. Therefore, the clap and fling, which involves two wings executing a set of synchronized motions, is considered. Thus, the selection of the aerodynamic analysis tool is based on its ability to model the effects of LEVs, wing rotation, and wake capture respectively.

1.3 Review of Literature

The following topics are reviewed in this section: (1) treatment of wing flexibility, (2) aerodynamic analysis tools, and (3) aeroelastic studies that examine the importance of wing flexibility in flapping wings.

1.3.1 Modeling Wing Flexibility

Early attempts to model flexibility in flapping wings included experimental studies that used geometrically scaled wings and computational studies that used simple physical models [28, 38]. These studies suggested that wing flexibility is an important factor in enhancing the aerodynamic efficiency of a flapping wing. Previous treatment of wing flexibility of anisotropic flapping wings using numerical approaches has been based on linear [39–41], and nonlinear finite element (FE) formulations based on commercial FE packages [29, 42, 43] or in-house codes [44–48]. The wing models used in these studies are summarized in Table 1.1.

References [39–41], which examined the aeroelastic behavior of flexible flapping

Reference	Wing Model based on	Software	Type of finite elements used
[39, 40]	hawkmoth	in-house	beam and membrane
[41]	bio-inspired	in-house	plate
[42]	dragonfly	ABAQUS 6.5	beam and shell
[29, 43]	hawkmoth	MSC MARC 2001	shell
[44]	dragonfly	in-house	shell
[45, 46]	bio-inspired (Zimmerman)	in-house and MSC MARC 2007	shell
[47, 48]	dragonfly	in-house	shell

Table 1.1: Summary of finite element wing models

wings, considered structural models in which wing flexibility was incorporated either using linear strain-displacement relations [39, 40] or free vibration modes for order reduction [41]. Structural models of hawkmoth wings, in which the geometric and material properties were obtained from available experimental data, were considered in Refs. [39, 40]. The structural model developed in Ref. [41] was validated with experiments conducted on an aluminum plate undergoing sinusoidal flapping motion. This study noted that linear approaches do not capture the centrifugal stiffening effect due to flapping, and incorporated this effect in the formulation by modifying the expressions that pertain to in-plane deformation. The tip displacements obtained using the modified model showed good agreement with a previously published result for the case of a flexible plate undergoing prescribed rotational acceleration.

The treatment of flexibility using nonlinear approaches [29, 42–48] has been based on formulations that utilize geometrically nonlinear strain displacement relations and the assumption of small strains.

Finite element models of dragonfly wings, based on detailed geometric measure-

ments using a micro computed tomography (micro-CT) technique, were developed in Ref. [42]; the material properties of various components of the wing were obtained from previously published data on insect wings. The FE models, developed in ABAQUS 6.5, were used to examine the deformation of flapping wings under several applied loading conditions that crudely approximated inertia and aerodynamic loads; in these simulations, the wings were actuated using a sinusoidal flap motion wherein the amplitude and frequency were close to realistic values of hovering dragonflies. This study mentions that the wing deformations obtained using linear and nonlinear structural dynamic models were nearly the same; consequently, it is emphasized that a linear structural model is adequate for the cases considered.

In Refs. [29, 43], structural models based on MSC MARC were developed to complement experimental studies conducted using insect wings. These studies attempted to approximate the aeroelastic response of flapping hawkmoth wings using structural dynamic models that incorporated suitable modifications in the material properties. In particular, Ref. [29] considered structurally damped wings to simulate the effect of aerodynamic damping, and Ref. [43] considered several spanwise distributions of elastic properties to obtain the bending patterns observed in real insect wings. The results suggest that the coupled aeroelastic problem of flapping wings may be reasonably approximated by uncoupled simulations using equivalent structural dynamic models.

An anisotropic shell model based on the updated Lagrangian approach is described in Ref. [44]. The primary focus of Ref. [44] was the formulation and implementation of the shell model. However, this study discussed a preliminary qualitative study in which the tip displacements of isotropic wings, which have varying Young's moduli, undergoing dragonfly kinematics were compared; specifically, the results showed that increasing the elastic modulus decreased the magnitude of wing deformation.

The formulation and implementation of an isotropic shell model based on a co-

rotational approach is described in Ref. [45]. The shell model, which was subsequently employed to simulate the aeroelastic behavior of plunging wings, was verified by comparing the tip displacements with previously published results and computations using a nonlinear shell model based on MSC MARC. The test cases included plates subjected to static end moments and lateral loads, and those undergoing sinusoidal flap motion with an amplitude of 17° for a range of frequencies. For all cases, the shell formulation showed excellent agreement with independently obtained computational results. Reference [46] extended the isotropic formulation [45] to incorporate composite materials. This study, which simulated anisotropic wings undergoing prescribed flap motion in vacuum, noted that the tip deformations computed using the extended shell model showed reasonable correlation with the experimental results published in Ref. [49]. An important conclusion of this work [46] was that the extended formulation was suitable for subsequent aeroelastic studies of anisotropic wings.

In Refs. [47, 48], shell formulations based on the total Lagrangian approach were used to simulate the aeroelastic behavior of dragonfly based wings undergoing prescribed sinusoidal motion. These studies considered isotropic wing models in which the thickness distribution was modified so as to simulate the experimentally measured spanwise and chordwise bending stiffness of insect wings; additional verification/validation of the structural models was not discussed.

1.3.2 Aerodynamic Modeling

As mentioned, the primary force generating aerodynamic mechanisms in flapping wings have been identified. Recent emphasis has been on investigating the interaction of the various mechanisms with kinematics. For example, water tunnel experiments conducted using airfoils undergoing combined pitch-plunge motion showed that the behavior of LEVs was dependent on the reduced frequency for a given effective angle of attack [50]; in these tests flow field measurements were done using particle

induced velocimetry (PIV), and the effective angle of attack was defined based on the combined pitch-plunge motion. Attempts to model the aerodynamic environment in a quantitative manner have been based on two approaches: (1) computational fluid dynamics (CFD) simulations based on the solution of the Navier Stokes (NS) equations and (2) approximate modeling based on surrogates and potential flow solutions.

Simulations using CFD, which yield the best resolution of the unsteady flow field, have shown good qualitative and quantitative agreement with experimental measurements for rigid airfoils and wings undergoing prescribed motion. Consequently, CFD based approaches have been employed to conduct numerous follow-up as well as independent investigations into the aerodynamics of flapping wings [2, 31, 36, 37]. The present study is focused on approximate aerodynamic models. Therefore, the review presented in this section is limited to a summary of select references and general observations/conclusions that are relevant to the work presented in this dissertation.

Investigations using CFD based tools have examined constrained [51] and unconstrained flight of hover capable flyers [52], and isolated wings [53], using rigid body models. Reference [51], which presented a comparative study of the hovering aerodynamics of various biological flyers ($\mathcal{O}(10) < Re < \mathcal{O}(10^3)$), noted that the mechanisms that stabilized the LEVs were dependent on Re. Specifically, increased spanwise flow gradients and stronger tip vortices were observed as Re increased. The importance of rapid wing rotation in augmenting the forces was more prominent at lower Re than at higher Re. Reference [53] examined the effect of wing rotation using fruit-fly wing models ($Re = \mathcal{O}(10^2)$) undergoing prescribed hover kinematics. Calculations showed that the forces generated were sensitive to wing rotation, indicating that an insect could easily maneuver by changing the timing of its wing rotation. In Ref. [52], hover and rapid maneuvering of fruit flies was simulated using a six degree of freedom model; the wing and body kinematics were obtained via experiments on free flying fruit flies. The forces generated were sensitive to wing kinematics, suggesting that a subtle change in wing and body kinematics was sufficient to allow an insect to execute

rapid maneuvers.

General comments, which may be gleaned from the substantial amount of literature on CFD based studies, are:

1. The unsteady aerodynamic forces obtained from CFD simulations have shown good quantitative correlation with experimental results for a variety of configurations, kinematics, and flow conditions. Therefore, results obtained from CFD based computations may be used in the absence of experimental data to examine the accuracy of approximate approaches.

2. Simulations using CFD support the hypothesis that LEVs are the most prevalent unsteady mechanism in hover capable flyers for Reynolds number in the range of $\mathcal{O}(10^2)$ to $\mathcal{O}(10^4)$.

3. Quantitative trends pertaining to the effect of wing geometry, kinematics, and Reynolds number, on the behavior of LEVs, spanwise flow, and tip vortices, have not been identified. This highlights a need for continued parametric studies on flapping wings.

4. Increasing the Reynolds number from $\mathcal{O}(10^2)$ to $\mathcal{O}(10^3)$ will increase in the intensity of spanwise flow and yield an increased contribution of tip vortices to forces generated by the wing.

Computations based on CFD require substantial amounts of computer time and are not suitable for parametric studies. Therefore approximate approaches, which offer a compromise between accuracy and computational efficiency, are important for trend and design studies. Approximate approaches that have been employed to model flapping wings include surrogate modeling based on CFD data and unsteady aerodynamic formulations based on potential flow.

Surrogate modeling involves the construction of computationally efficient approximations, called surrogates, of an expensive system by interpolating the input/output

data obtained from a limited number of full order evaluations. The surrogates replace the expensive computations to predict loads at points that were not included in the initial set of fitting points. In the context of flapping wing aerodynamics, surrogate models based on CFD data were used to investigate the impact of LEVs and tip vortices on the lift and thrust generated by a rectangular wing undergoing prescribed translation and pitching motions [54, 55]. The surrogates were constructed by interpolating the time averaged forces generated by the wing as a function of the amplitudes and phase difference of wing motions at $Re = 100$. These studies [54,55] noted that the impact of tip vortices on force generation is dependent on kinematics, and identified regions of the parameter space where tip vortices had a beneficial effect.

The approximate unsteady aerodynamic theories, based on potential flow, used for flapping wing problems can be classified as assumed (or prescribed) wake and free wake models. Formulations that have practical value have to be able to model the effect of LEVs and wake capture. It is important to note that these approximate models are incapable of representing the physics of flow separation and re-attachment. Therefore, they are based on an ad hoc assumption regarding the onset of flow separation as well as the location of the separation point.

Assumed wake models are classical unsteady models such as Theodorsen's theory [56]. In Ref. [30], the effect of the LEVs in Theodorsen's theory was incorporated by modifying the unsteady aerodynamic lift and moment expressions using the Polhamus leading edge suction analogy [57] that was originally proposed for steady separated flow on delta wings. This model [30], which was compared to experiments, was capable of predicting the trends in aerodynamic forces.

Free wake models account for evolution of the wake, thereby providing a reasonable approximation to the development of the unsteady wake during a flapping cycle. Free wake models that account for LEVs are two-dimensional formulations that are based on a discrete vortex representation of the wake [58–62]. These formulations are

applied in a strip theory manner, and are suitable for flapping wings in hover following simplifying assumptions on the geometry of the shed wake.

In Ref. [58] the flow field around a rigid thin airfoils was obtained by solving the boundary integral associated with the velocity field. The velocity field was expressed as a linear combination of Chebyshev polynomials, wherein the corresponding coefficients are determined during the solution process. This model showed reasonable agreement with previously published experimental data for plunging airfoils; however, numerical instabilities were encountered in simulations when a pitching airfoil interacted with its own wake. Reference [60] extended the approach described in Ref. [58] to include flexible airfoils undergoing prescribed rigid body plunge motion and prescribed deformation. It was noted that additional work was required before the formulation could be used for aeroelastic studies.

Reference [59] considered a flow field description based on the velocity potential, and outlined a method of solution based on similarity expansion that is valid when the geometric scale of the LEV is small compared to the airfoil chord. In this approach, the circulation of the vortices shed from the leading and trailing edges are assumed to have the same magnitude but opposite signs; the positions are assumed to be symmetric with respect to the mid chord line. The unsteady loads computed using this model showed reasonable correlation with those obtained from NS computations for an accelerating elliptic airfoil at fixed angle of incidence.

A thin airfoil theory that accounts for chordwise flexibility and separation close to the leading edge was developed in Ref. [61]. The chordwise location of the separation point, obtained using independent computations or experiments, is explicitly incorporated into the formulation. The model compared well with experimental data for airfoils in steady flow [61], and was employed in Ref. [63] to calculate the forces generated by a wing undergoing prescribed pitch and plunge motions in the presence of a free stream. Comparisons showed that the unsteady loads computed using the

approximate model showed reasonable correlation with those obtained from CFD calculations based on FLUENT (a commercial software); however, results indicated that the effect of LEVs was minor for the cases considered.

The development and implementation of a discrete vortex model (DVM) that is applicable to rigid insect-like flapping wings in hover is presented in Refs. [62, 64]. This model, which extended the airfoil theory developed in Refs. [65–67] to incorporate LEVs, accounts for wing thickness and camber, and includes a free wake model. It was assumed in Refs. [62, 64] that the separation point was at the leading edge; however, the formulation is sufficiently general to incorporate flow separation at any other point on the airfoil. The implementation involved applying the airfoil theory on rigid flapping wings in a stripwise manner. The spanwise stations, called radial chords in Ref. [62], were marked using circular arcs of varying radii. The model was used to simulate rigid airfoils and scaled fruit-fly wings in hover, and for the cases considered, showed reasonable agreement with experimental data [64].

1.3.3 Aeroelastic Studies and Effect of Wing Flexibility

The importance of wing flexibility for enhancing the force producing capability of flapping wings has been suggested in several studies. Attempts to examine this issue in a systematic manner include experimental [49, 68–74] and computational studies [39, 40, 48, 70, 75–81].

Several studies [68, 72, 73, 75, 76] have examined the influence of wing flexibility using aeroelastic tests/simulations in water or other media. Although these attempts fall under the general category of flapping wing aeroelasticity, it is important to recognize that interplay between wing flexibility, inertia loads, and aerodynamic loads, obtained in these studies [68, 72, 73, 75, 76] does not capture the interactions in biological and bio-inspired flapping wings that operate in air.

References [68, 75] examined plunging wings in forward flight. The combinations

of kinematics and flow conditions considered in these studies are more representative of aquatic propulsion than of flapping wing flight. Reference [75] simulated thin foils undergoing prescribed pitch and plunge motions in air and water. The aeroelastic model was obtained by coupling an isotropic thin plate model with an unsteady panel method. Results showed that wing flexibility that had a beneficial effect in air could be detrimental in water, and vice versa. Water tunnel tests, which examined the effect of spanwise flexibility on the thrust, lift, and propulsive efficiency of plunging wings, are described in Ref. [68]. The wings were actuated using a prescribed sinusoidal motion for $10,000 < Re < 30,000$ at several reduced frequencies. Measurements showed that aerodynamic force generation capacity of the wings was non-monotonic with respect to flexibility.

Experiments in water, in which the aerodynamic forces generated by rigid and flexible geometrically scaled hawkmoth wings in hover were measured, are described in Refs. [72, 73]. The conclusions of these studies are somewhat qualitative and indicate that only a limited amount of flexibility is beneficial. In Ref. [72], several wing configurations were actuated using representative hover kinematics $Re \sim 7500$ at a frequency of 0.15 Hz. Measurements showed that increasing flexibility caused a significant drop in forces compared to the rigid wing. In Ref. [73], flexible wings that closely approximated hawkmoth wings were actuated using several simplified versions of insect hover kinematics at a frequency of 0.9 Hz. The results showed that the thrust generated by the flexible wings was significantly larger than that generated by the rigid wings for all the cases considered.

The earliest attempt to examine the influence of wing flexibility in insect wings using computational tools was based on coupling FE models of hawkmoth wings with an unsteady panel method [39, 40]. Wing flexibility was incorporated using linear strain displacement relations and the effect of LEVs and wake-capture were neglected in the aerodynamic calculations. The wings were actuated using a sinusoidal flap motion in which the amplitude and frequency were close to realistic values of the corresponding

insect. Results indicated that wing flexibility had a beneficial, but minor, effect on force generation. This study concluded that improved aerodynamic analysis tools were needed to examine the aeroelastic behavior under realistic operating conditions.

References [30, 70] describe a combined experimental and computational study using bio-inspired wings that are composed of a mylar membrane stretched over a metal skeleton. Several configurations were tested up to flapping frequencies of 12 Hz where $\mathcal{O}(10^3) < Re < \mathcal{O}(10^5)$. The experiments, conducted in air and vacuum, showed that inertia loads constituted the major portion of loads acting on the flapping wings. The thrust generated by the wings was found to decrease substantially at higher flapping frequencies. The aeroelastic simulations were conducted using an approximate model that was obtained by combining an in-house linear plate based FE solver with an unsteady approximate aerodynamic model that is based on Theodorsen's theory modified using Polhamus analogy. Wing flexibility was incorporated using via free vibration modes. Two sets of simulations were performed: an uncoupled analysis in which the effect of aerodynamic loads on wing was ignored when computing the response of the wing, and a coupled analysis in which the aerodynamic loads were considered when computing the wing response. The results, which showed acceptable correlation with experiments for the cases considered, indicated that wing flexibility had a beneficial impact on force generation. The thrust predicted by the coupled and uncoupled analyses was similar; however, the bending moment and magnitude of tip deformation were significantly different. An important conclusion of this study was that the impact of aerodynamic loads cannot be neglected when estimating the magnitude of wing deformation.

References [49, 69] presented a comprehensive experimental study in which the aeroelastic behavior and thrust generation of anisotropic flapping wings was characterized based on their material properties, static and dynamic response, and aerodynamic environment. The wings, which were based on a Zimmerman planform, were composed of a membrane that was reinforced by a spar-batten skeleton that was constructed us-

ing composite prepreg material. Several wing configurations were obtained by varying the number of prepreg layers in the spar and battens. The experiments included static bending tests, frequency response measurements in air, and flapping tests in vacuum and air. In the flapping tests, the wings were actuated using a sinusoidal motion that had amplitude of 35° for frequencies ranging from 5 Hz to 40 Hz and the loads were measured using a force transducer at the root. Thrust measurements indicated that the choice of the best flexible configuration was dependent on the flapping frequency; specifically, the more flexible wings produced maximum thrust at lower frequencies whereas the stiffer wings were more effective at higher frequencies. A peak in thrust was obtained when the excitation frequency was close to the resonant frequency of the wings. Moreover, the tip deformation patterns of the wings flapping in vacuum were significantly different from those measured in air, suggesting that the aerodynamic loads may be comparable to inertia loads for the cases considered.

Reference [71] examined the influence of flexibility in biological wings by conducting static and flapping tests using freshly cut and aged hawkmoth wings. Static bending tests, in which the wings were treated as beams, showed that the spanwise bending stiffness of the aged wings was considerably greater than that of freshly cut wings. In subsequent flapping tests, flow field measurements using DPIV showed that the induced velocity generated by the fresh wings was considerably larger than that of the aged wings. The wings used in this study were actuated using a flap motion that approximated the hover kinematics in hawkmoths. Larger induced velocities of flexible wings implies greater lift generation capacity; therefore, this study concluded that insects benefited from wing flexibility.

Reference [76] simulated isotropic plunging wings, which were offset by a constant flap rotation, in hover for $Re = 100$. The aeroelastic model was obtained by coupling a viscous incompressible fluid description based on a lattice Boltzmann model to a structural description based on a lattice spring model. Wing flexibility was incorporated using linear springs. The lift and power coefficients, and lift-to-power ratio (efficiency),

were characterized using mass ratio and frequency that is normalized using the resonant frequency of the structure in the viscous fluid. Results showed that a peak in lift coefficient was obtained for a normalized frequency of 0.95 for all values of mass ratio; moreover increasing the mass ratio decreased the magnitude of the peak. Peak efficiency was obtained at a frequency ratio of 1.25 and the magnitude of the peak increased with increased in mass ratio. Also, specific combination of parameters for which the lift generated was sufficient to support the weight of a realistic insect were identified. Consequently, this study concluded that wing flexibility and kinematics could be tailored so as to generate a desired amount of lift.

In Ref. [48], the fluid-structure interaction in representative dragonfly wings in hover was simulated using a finite element analysis based on the arbitrary Lagrangian-Eulerian method. The unsteady aerodynamic loads were computed using CFD based model. The structural models were based on data obtained from geometric and static bending tests on dragonfly wings. Simulations were conducted for three cases: flexible and rigid wings undergoing hover kinematics, and a rigid wing undergoing kinematics that are modified to match the tip motion of the flexible wing. The results showed that the average energy consumption and lift of the flexible wing was approximately equal to that of the rigid wing with modified kinematics; however, the rigid wing required 19% more peak torque and 34% more peak power, indicating that wing flexibility had a beneficial effect on power consumption.

Numerical simulations, based on NS calculation on a deforming mesh, were used to examine the effect of wing deformation on the aerodynamic performance in hoverflies [77]. The aerodynamic forces were computed using a wing that is undergoing prescribed spanwise and chordwise deformations, wherein the time history of the deformations were obtained via measurements on hoverflies in free flight. The simulations, conducted for $Re = 800$, showed that the deforming wing generated 10% more lift and required 5% less power compared to a rigid wing. The increase in lift and decrease in power were attributed to the camber deformation and spanwise twist

respectively, thus leading to a conclusion that wing flexibility was beneficial to insects.

References [78, 79] describe the development of a computational aeroelastic framework obtained by combining geometrically nonlinear beam and shell based structural dynamic models with a CFD based flow field. The framework, which was validated by simulating the experiments in Ref. [68] and comparing with aeroelastic simulations that utilized a structural dynamic model based on MSC MARC, was employed in Ref. [82] to simulate isotropic Zimmerman wings in hover. In this study [82], the wings were actuated using a sinusoidal flap motion at a frequency of 10 Hz. For the cases considered, the tip displacements and pressure distribution computed using the aeroelastic model showed reasonable correlation with corresponding experimentally measured quantities. The variation in lift due to flexibility by varying the elastic modulus of the wings was also examined. The results showed that the lift was non-monotonic, i.e. first increased and then decreased, with flexibility. Therefore, this study concluded that only a limited amount of flexibility was beneficial for thrust generation.

Impact of flexibility on the soaring and forward flight performance of ornithopter wings was examined using wind tunnel tests [74] and simulations [80, 81]. Measurements using nylon- and latex-based wings that are reinforced by a metal frame [74], for $Re = 20,000$ to $Re = 80,000$ and advance ratios ranging from 0.3 to 8, showed that increasing chordwise flexibility improved the lift-to-drag ratio of wings in soaring and high speed forward flight, whereas the influence of spanwise flexibility was more prominent at lower advance ratios. Membrane wings, undergoing prescribed flap and torsion at $Re = 10^3$ and advance ratio of 0.5, were simulated using an aeroelastic model that is obtained by coupling a linear elastic membrane solver with an unsteady LES (Large Eddy Simulation) flow solver [80]. Calculations, in which effect of inertia forces was neglected, showed that the flexible camber prolonged the attachment of LEVs on the wing surface compared to a rigid wing, thereby increasing the thrust and lift considerably. Reference [81] simulated rigid and flexible flapping wings in

forward flight (advance ratios of 0.5 to 4) using an aeroelastic model that combined a commercially available flow solver (CFD-ACE+) with a structural dynamics solver (FEMSTRESS). Results, obtained for wings that are composed of a parylene membrane reinforced with a titanium leading edge spar, showed that stiffness distribution was a key parameter in thrust production; specifically, a stiffer outboard region enhanced lift whereas a more flexible inboard region enhanced thrust.

1.4 Objectives

Based on a review of literature presented, it is evident that a detailed understanding of the influence of wing flexibility in flapping wings in hover and forward flight is still an unsolved problem. While several studies have found that a certain amount of wing flexibility is beneficial, a quantitative characterization of this issue has been inconclusive. Also, a systematic treatment of moderate-to-large deformation of anisotropic flapping wings in the context of their aeroelastic behavior has not been considered. Therefore, the primary objective of this dissertation is to contribute towards the quantitative and qualitative understanding of the effect of flexibility on the performance of anisotropic insect-based flapping wings in hover and forward flight.

Due to the large parameter space associated with the aeroelastic problem of flapping wings, computational tools that allow a rapid exploration of the space are extremely useful. To date, approximate aeroelastic modeling of insect-based flapping wings has been considered in Refs. [30, 70]. The aeroelastic model developed in these studies incorporated wing flexibility in a linear manner, employed an assumed wake model that does not incorporate the effect of wake capture, and is limited to wings in hover. Therefore, a nonlinear approximate aeroelastic model that is suitable for flexible anisotropic wings in hover and forward flight is developed in this dissertation. The aeroelastic model is obtained by coupling a nonlinear finite element (FE) model of the wing based on the MARC code [83] with an approximate unsteady aerodynamic

model that is based on potential flow. The approximate aerodynamic model, which is based on the formulation originally developed in Refs. [62, 64] for rigid wings in hover, incorporates the effect of LEVs, wake capture, wing flexibility, effect of Reynolds number, and effect of free stream due to forward flight. The specific objectives of the dissertation are as follows:

1. Present a summary of the nonlinear aeroelastic model.
2. Describe the modifications to the aerodynamic model.
3. Determine the suitability of MARC for modeling flexible anisotropic flapping wings.
4. Describe the development of structural dynamic models for anisotropic wings.
5. Compare results obtained using the approximate aerodynamic model with those obtained using CFD for cases in which LEVs occur.
6. Compare results obtained using the approximate aeroelastic model with CFD based and/or available experimental data for flapping wings in hover.
7. Examine the influence of wing flexibility on the performance and behavior of anisotropic flapping wings in hover and forward flight.

1.5 Novel Contributions of the Dissertations

The main new contributions made in this dissertation are:

1. The development of a reliable and computationally efficient approximate aeroelastic tool that is suitable for flexible insect-based flapping wings in hover and forward flight. The model accounts for moderate-to-large wing deformation, LEVs, and wake-capture.

2. Determined the suitability of the structural dynamic model in MSC MARC to address the flapping wing problem.

3. Modification of the original aerodynamic formulation [62,64] to account for wing flexibility, effect of viscosity, and the effect of free stream due to forward flight.

4. Correlation with experimental data generated in Refs. [49,69].

5. Extensive trend studies on rigid and flexible flapping wings in hover and forward flight.

CHAPTER II

Structural Dynamic Modeling

The structural dynamic models of MAV wings are developed in MARC [83] using shell elements that are capable of undergoing large amplitude rigid body motion as well as moderate-to-large flexible deformation. The shell elements are used in conjunction with kinematic constraints and a variety of constitutive laws to model isotropic as well as anisotropic flapping wings. A discussion on wing kinematics and material modeling is provided in this chapter.

2.1 Wing Kinematics

Wing kinematics of a bio-inspired flapping wing include large amplitude, time dependent rigid body rotations imposed at the base (root) of the wing. These kinematics are usually represented by Euler angles or a similar approach for accounting large rotations.

2.1.1 Representation of Rigid Body Rotations

Representation of large rigid body rotations, also called *finite rotations*, has been treated extensively in literature [84–86]. Any general rotation in three dimensional (3D) Euclidean space may be represented as a proper orthogonal tensor, and the

operation of rotation on a vector space is equivalent to multiplication by this tensor. However, parametric representation of rotations leads to efficient formulation of the dynamics. Such parameterizations are broadly classified as *vectorial* and *non-vectorial* [84, 86]. A minimum of three parameters are required to fully define a rotation in 3D space; therefore, parameterizations are further classified into minimal (characterized by three parameters) or non-minimal (characterized by more than three parameters) representations. Vectorial representations are minimal in nature and form a geometric vector in 3D space; these include representation using Caley, Gibbs, Rodrigues, Wiener, or Milenkovic parameters [84]. While rotations are represented as vectors, they do not behave as vectors except for small or incremental rotations. Non-vectorial representations use a matrix representation for rotations. They are either minimal, such as Euler angles, or non-minimal, such as the matrix of direction cosines, representations based on Euler-Rodrigues, or Caley-Klein parameters.

Euler angles, used to describe the flight dynamics of fixed wing aircraft, have been used to describe the wing kinematics of flapping wing flyers [18–26]. In MARC, rigid body rotations may be imposed as boundary conditions either using the rotation vector or as displacements at two or more nodes [83]. A brief discussion on these representations is presented next.

Rotation Vector

Any rotation about a fixed pivot can be uniquely described using a rotation vector shown in Eq. (2.1).

$$\boldsymbol{\psi}(t) = \psi(t)\,\hat{\mathbf{e}}(t) \tag{2.1}$$

$$\text{where} \quad \hat{\mathbf{e}}(t) = \begin{Bmatrix} \hat{e}_x(t) \\ \hat{e}_y(t) \\ \hat{e}_z(t) \end{Bmatrix} \qquad \text{and} \qquad \|\hat{\mathbf{e}}\| = \sqrt{\hat{e}_x^2 + \hat{e}_y^2 + \hat{e}_z^2} = 1$$

where $\hat{\mathbf{e}}(t)$ and $\psi(t)$ denote the time dependent axis of rotation measured in an inertial Cartesian coordinate system and the angle of rotation respectively. The effect of the rotation $\boldsymbol{\psi}$ is defined as multiplication by a rotation tensor $\hat{\boldsymbol{R}}_{(\boldsymbol{\psi})}$, where:

$$\hat{\boldsymbol{R}}_{(\boldsymbol{\psi})} = \begin{bmatrix} c_\psi + \hat{e}_x^2(1-c_\psi) & -\hat{e}_z s_\psi + \hat{e}_x\hat{e}_y(1-c_\psi) & \hat{e}_y s_\psi + \hat{e}_x\hat{e}_z(1-c_\psi) \\ \hat{e}_z s_\psi + \hat{e}_x\hat{e}_y(1-c_\psi) & c_\psi + \hat{e}_y^2(1-c_\psi) & -\hat{e}_x s_\psi + \hat{e}_y\hat{e}_z(1-c_\psi) \\ -\hat{e}_y s_\psi + \hat{e}_x\hat{e}_z(1-c_\psi) & \hat{e}_x s_\psi + \hat{e}_y\hat{e}_z(1-c_\psi) & c_\psi + \hat{e}_z^2(1-c_\psi) \end{bmatrix} \tag{2.2}$$

Here the contracted notation $c_\psi = \cos\psi$, and $s_\psi = \sin\psi$ is used. Inverse relations, using which components of the rotation vector can be computed from a given rotation tensor, are:

$$\begin{aligned} \psi &= \cos^{-1}\left[\frac{\hat{R}_{11} + \hat{R}_{22} + \hat{R}_{33} - 1}{2}\right] \\ \hat{e}_x &= \frac{(\hat{R}_{32} - \hat{R}_{23})}{2\sin\psi} \\ \hat{e}_y &= \frac{(\hat{R}_{13} - \hat{R}_{31})}{2\sin\psi} \\ \hat{e}_z &= \frac{(\hat{R}_{21} - \hat{R}_{12})}{2\sin\psi} \end{aligned} \tag{2.3}$$

where $\hat{R}_{ij}$, $i,j = 1,2,3$, denote the elements of the rotation tensor.

The following example illustrates the use of rotation vectors in the context of flapping wings. Let O and O_w represent non-rotating (stationary) and wing-fixed Cartesian coordinate systems that coincide at the start of the rotation ($t = 0$). Let $\boldsymbol{x}$ and $\boldsymbol{x}_w$ denote position vectors, measured in O and O_w respectively, of a point P that is fixed on the wing. Note that $\boldsymbol{x}_w$ is a constant vector and $\boldsymbol{x}(0) = \boldsymbol{x}_w$. After a

rotation $\boldsymbol{\psi}$ that describes the time dependent wing kinematics, the position vector of P measured in O is:

$$\boldsymbol{x}(t) = \hat{\boldsymbol{R}}_{(\boldsymbol{\psi})} \boldsymbol{x}_w \tag{2.4}$$

Euler Angles

Euler angles correspond to successive rotations that are performed about non-parallel body-fixed axes [86]. Rotation using Euler angles is specified using three angles, and a sequence of axes about which each successive rotation is performed. Each Euler rotation can the conveniently represented as a rotation vector that has a fixed axis of rotation in the body fixed coordinate system. The complete rotation is obtained by multiplying the rotation tensors corresponding to each rotation vector as illustrated by the following example.

Consider a sequence of Euler angles given by $\psi_1(t)$ about Y_w, $\psi_2(t)$ about X_w, and $\psi_3(t)$ about Z_w, where X_w, Y_w, and Z_w are the wing-fixed axes. Using the previous example of O, O_w, the intermediate orientations of the body-fixed frame after each rotation are identified: O_1 is obtained from O following the first rotation; O_2 is obtained from O_1 following the second rotation; and O_w is obtained from O_2 following the third rotation. At any time, the position vectors of P are $\boldsymbol{x}$, $\boldsymbol{x}_1$, $\boldsymbol{x}_2$, and $\boldsymbol{x}_w$, measured in O, O_1, O_2, and O_w respectively. These vectors are related as:

$$\begin{aligned}
\boldsymbol{x} &= \hat{\boldsymbol{R}}_{(\boldsymbol{\psi}_1)} \boldsymbol{x}_1 \qquad \text{where } \boldsymbol{\psi}_1 \text{ is defined in } O \\
\boldsymbol{x}_1 &= \hat{\boldsymbol{R}}_{(\boldsymbol{\psi}_2)} \boldsymbol{x}_2 \qquad \text{where } \boldsymbol{\psi}_2 \text{ is defined in } O_1 \\
\boldsymbol{x}_2 &= \hat{\boldsymbol{R}}_{(\boldsymbol{\psi}_3)} \boldsymbol{x}_3 \qquad \text{where } \boldsymbol{\psi}_3 \text{ is defined in } O_2
\end{aligned} \tag{2.5}$$

Note that $\boldsymbol{\psi}_1$ is a rotation about the Y axis in O, $\boldsymbol{\psi}_2$ is a rotation about the X axis in

O_1, and $\boldsymbol{\psi}_3$ is a rotation about the Z axis in O_2. Therefore:

$$\boldsymbol{\psi}_1(t) = \psi_1(t)\begin{Bmatrix}0\\1\\0\end{Bmatrix} \qquad \boldsymbol{\psi}_2(t) = \psi_2(t)\begin{Bmatrix}1\\0\\0\end{Bmatrix} \qquad \boldsymbol{\psi}_3(t) = \psi_3(t)\begin{Bmatrix}0\\0\\1\end{Bmatrix} \tag{2.6}$$

Combining Eqs. (2.5) gives:

$$\begin{aligned} \boldsymbol{x}(t) &= \hat{\boldsymbol{R}}_{(\boldsymbol{\psi}_1)}\hat{\boldsymbol{R}}_{(\boldsymbol{\psi}_2)}\hat{\boldsymbol{R}}_{(\boldsymbol{\psi}_3)}\boldsymbol{x}_w \\ &= \hat{\boldsymbol{R}}_{(\boldsymbol{\psi}_1,\boldsymbol{\psi}_2,\boldsymbol{\psi}_3)}\boldsymbol{x}_w \end{aligned} \tag{2.7}$$

where each $\hat{\boldsymbol{R}}_{(\boldsymbol{\psi}_j)}$, $j = 1,2,3$, is obtained by substituting $\boldsymbol{\psi}_j$ into Eq. (2.2), and $\hat{\boldsymbol{R}}_{(\boldsymbol{\psi}_1,\boldsymbol{\psi}_2,\boldsymbol{\psi}_3)}$ is the rotation tensor corresponding to the complete rotation.

It is important to note that different sequences of rotation may result in the same rotation tensor. Therefore, Euler angles that correspond to a given rotation tensor are not unique. A comprehensive discussion on the procedure to compute Euler angles from a given rotation tensor by assuming different sequences is presented in Ref. [86].

The following terminology is used in this dissertation: a time dependent rotation about a fixed axis of rotation is referred to as a two dimensional (2D) rotation; pure flapping or pure pitching motions fall into this category. The most general case of a rotation in which magnitude as well as the axis of rotation are time dependent are called three dimensional (3D) rotations. Thus, insect-like kinematics, which are described by a combination of two or three Euler angles, are 3D rotations.

2.1.2 Implementation in MARC

In MARC, time dependent rigid body rotations may be input either as rotation boundary conditions (BCs) at a single node or as displacement BCs at selected nodes [87]. The time history of the BCs is specified either directly in the input file or via

the FORCDT user subroutine. When specified in the input file, the values of the DOFs at the node(s) are provided for each time step. When specified in the FORCDT subroutine, incremental values of DOFs are provided.

The incremental rotation vector is:

$$\Delta\boldsymbol{\psi}(t) = \boldsymbol{\psi}(t+\Delta t) - \boldsymbol{\psi}(t) \tag{2.8}$$

where $\boldsymbol{\psi}(t)$ is calculated for a given $\hat{\boldsymbol{R}}(t)$ using Eq. (2.3). The components of $\boldsymbol{\psi}(t)$ or $\Delta\boldsymbol{\psi}(t)$ are specified as the rotation BCs at the node. The displacement DOFs at the node are constrained when specifying rotation BCs.

The displacements and incremental displacements are:

$$\boldsymbol{u}(t) = \boldsymbol{x}(t+\Delta t) - \boldsymbol{x}(t) \quad \text{and} \quad \Delta\boldsymbol{u}(t) = \boldsymbol{u}(t+\Delta t) - \boldsymbol{u}(t) \tag{2.9}$$

where $\boldsymbol{x}(t)$ is the time dependent position vector of a point in the unrotated coordinate system as discussed in the preceding examples. The components of $\boldsymbol{u}(t)$ or $\Delta\boldsymbol{u}(t)$ are specified as the displacement BCs at the selected nodes. The rotational DOFs of the nodes are not constrained when specifying displacement BCs.

2.1.3 Kinematic and Rigid Body Constraints

In MARC, the kinematic BCs and rigid body constraints are enforced using an augmented Lagrange multiplier method that is also employed in the nonlinear solver 'SOL 400' in MSC NASTRAN [87]. The augmented Lagrange multiplier (ALM) method, described in Chapter 3 of Ref. [87], is summarized next.

The kinematic constraints imposed on the nodal DOFs in the global structure, represented in matrix form, are:

$$\boldsymbol{\Phi}_c(\boldsymbol{u}) = \boldsymbol{u_c} \tag{2.10}$$

Using the ALM method, the constraints are included as an additional contribution, Π_{con}, to the elastic strain energy of the structure, where:

$$\Pi_{con} = k_\lambda \, \boldsymbol{\lambda}^T (\boldsymbol{\Phi}_c - \boldsymbol{u_c}) + \frac{1}{2} (\boldsymbol{\Phi}_c - \boldsymbol{u_c})^T \, k_{pe} \, (\boldsymbol{\Phi}_c - \boldsymbol{u_c}) \tag{2.11}$$

In Eq. (2.11), the first and second terms are the contribution of the Lagrange multipliers and the added penalty term to the strain energy respectively, and k_{pe} is a penalty stiffness. In traditional penalty methods, the penalty stiffness is typically an order or more higher than the stiffness of the structure and may result in stiff equations and ill-posed matrices. Using the ALM method, it is noted that a k_{pe} of the order of the structural stiffness is adequate, thus representing an advantage over traditional penalty formulations [88, 89]. The energy due to the constraints may be expressed as the work done by an internal force $\boldsymbol{E}_{con}$ that is obtained following a first variation of Π_{con}:

$$\begin{aligned}
\delta\Pi_{con} &= \delta \boldsymbol{u}^T \boldsymbol{H}^T \left(k_{pe} (\boldsymbol{\Phi}_c - \boldsymbol{u_c}) + k_\lambda \boldsymbol{\lambda} \right) + \delta \boldsymbol{\lambda}^T k_\lambda (\boldsymbol{\Phi}_c - \boldsymbol{u_c}) \\
&= \left\{ \delta \boldsymbol{u}^T \quad \delta \boldsymbol{\lambda}^T \right\} \begin{Bmatrix} \boldsymbol{H}^T \left(k_{pe} (\boldsymbol{\Phi}_c - \boldsymbol{u_c}) + k_\lambda \tilde{\boldsymbol{\lambda}} \right) \\ k_\lambda (\boldsymbol{\Phi}_c - \boldsymbol{u_c}) \end{Bmatrix} \qquad (2.12) \\
&\equiv \left\{ \delta \boldsymbol{u}^T \quad \delta \boldsymbol{\lambda}^T \right\} \boldsymbol{E}_{con} \qquad (2.13)
\end{aligned}$$

where

$$\boldsymbol{H} = \frac{\partial}{\partial \boldsymbol{u}} (\boldsymbol{\Phi}_c - \boldsymbol{u_c}) = \frac{\partial \boldsymbol{\Phi}_c}{\partial \boldsymbol{u}} \tag{2.14}$$

and

$$\boldsymbol{E}_{con} = \begin{Bmatrix} \boldsymbol{H}^T \left(k_{pe} (\boldsymbol{\Phi}_c - \boldsymbol{u_c}) + k_\lambda \boldsymbol{\lambda} \right) \\ k_\lambda (\boldsymbol{\Phi}_c - \boldsymbol{u_c}) \end{Bmatrix} = \begin{Bmatrix} \boldsymbol{E}^{\boldsymbol{u}}_{con} \\ \boldsymbol{E}^{\boldsymbol{\lambda}}_{con} \end{Bmatrix} \tag{2.15}$$

The contribution of the constraints to the strain energy vanishes if the constraints are imposed in an exact manner. Therefore, imposing the constraints in a numerical manner involves minimizing $\boldsymbol{E}_{con}$. Consider a first order Taylor expansion of $\boldsymbol{E}_{con}$:

$$\boldsymbol{E}_{con}(\boldsymbol{u}+\Delta\boldsymbol{u},\boldsymbol{\lambda}+\Delta\boldsymbol{\lambda}) = \boldsymbol{E}_{con}(\boldsymbol{u},\boldsymbol{\lambda}) + \boldsymbol{K}_{con}(\boldsymbol{u},\boldsymbol{\lambda}) \begin{Bmatrix} \Delta\boldsymbol{u} \\ \Delta\boldsymbol{\lambda} \end{Bmatrix} \tag{2.16}$$

The corresponding tangent stiffness matrix is:

$$\boldsymbol{K}_{con} = \begin{bmatrix} \boldsymbol{K}_{11} & \boldsymbol{K}_{12} \\ \boldsymbol{K}_{21} & \boldsymbol{K}_{22} \end{bmatrix} \tag{2.17}$$

where

$$\begin{aligned}
\boldsymbol{K}_{11} &= \frac{\partial \boldsymbol{E}^{\boldsymbol{u}}_{con}}{\partial \boldsymbol{u}} = \boldsymbol{H}^T(\boldsymbol{u}) k_{pe} \boldsymbol{H}(\boldsymbol{u}) + \frac{\partial \boldsymbol{H}^T}{\partial \boldsymbol{u}}(\boldsymbol{u}) \left(k_{pe} \left(\boldsymbol{\Phi}_c(\boldsymbol{u}) - \boldsymbol{u_c} \right) + k_\lambda \boldsymbol{\lambda} \right) \\
\boldsymbol{K}_{12} &= \frac{\partial \boldsymbol{E}^{\boldsymbol{u}}_{con}}{\partial \boldsymbol{\lambda}} = k_\lambda \boldsymbol{H}^T(\boldsymbol{u}) \\
\boldsymbol{K}_{21} &= \frac{\partial \boldsymbol{E}^{\boldsymbol{\lambda}}_{con}}{\partial \boldsymbol{u}} = k_\lambda \boldsymbol{H}(\boldsymbol{u}) \\
\boldsymbol{K}_{22} &= \frac{\partial \boldsymbol{E}^{\boldsymbol{\lambda}}_{con}}{\partial \boldsymbol{\lambda}} = 0
\end{aligned} \tag{2.18}$$

Here, $\boldsymbol{E}_{con}$ and $\boldsymbol{K}_{con}$ represent the contribution of the constraints to the residual force vector and the tangential stiffness matrix of the constrained elastic structure respectively. These are incorporated during the assembly of the global residual force and global stiffness matrix of the structure, and the residual force vector is minimized using a Newton-Raphson algorithm as outlined in Section 4.1.

2.2 Modeling Composite Materials

The constitutive laws used to model composite materials in MARC are discussed in Volume A of Ref. [83]. The shell elements available in MARC are based on thin and thick shell formulations. The specific forms of the constitutive law used in these

formulations are given in Eqs. (2.19) and (2.20), and the stress-strain relations for a composite element are given in Eq. (2.21). Thin shell elements utilize a plane stress assumption to calculate the stresses and strains through the thickness of the element. Thick shell elements, on the other hand, consider the effect of transverse shear explicitly in the formulation. In both shell formulations, the numerical integration through the thickness is performed using Simpson's rule for isotropic materials and trapeziodal rule for composite materials. In this dissertation, anisotropic wings are modeled using thick shell elements based on an assumption that explicit treatment of transverse shear may improve accuracy when modeling the structural dynamic behavior of composite structures. Isotropic wings are also modeled using thick shell elements, although the differences between predictions using thick and thin shells is expected to be small for these wings.

For thick shell elements

$$\begin{Bmatrix} \epsilon_{11} \\ \epsilon_{22} \\ \gamma_{12} \\ \gamma_{23} \\ \gamma_{31} \end{Bmatrix} = \begin{bmatrix} \frac{1}{E_{11}} & \frac{-\nu_{21}}{E_{22}} & 0 & 0 & 0 \\ \frac{-\nu_{12}}{E_{11}} & \frac{1}{E_{22}} & 0 & 0 & 0 \\ 0 & 0 & \frac{1}{G_{12}} & 0 & 0 \\ 0 & 0 & 0 & \frac{1}{G_{23}} & 0 \\ 0 & 0 & 0 & 0 & \frac{1}{G_{31}} \end{bmatrix} \begin{Bmatrix} \sigma_{11} \\ \sigma_{22} \\ \tau_{12} \\ \tau_{23} \\ \tau_{31} \end{Bmatrix} \tag{2.19}$$

For thin shell elements

$$\begin{Bmatrix} \epsilon_{11} \\ \epsilon_{22} \\ \gamma_{12} \end{Bmatrix} = \begin{bmatrix} \frac{1}{E_{11}} & \frac{-\nu_{21}}{E_{22}} & 0 \\ \frac{-\nu_{12}}{E_{11}} & \frac{1}{E_{22}} & 0 \\ 0 & 0 & \frac{1}{G_{12}} \end{bmatrix} \begin{Bmatrix} \sigma_{11} \\ \sigma_{22} \\ \tau_{12} \end{Bmatrix} \tag{2.20}$$

where the 1, 2, and 3 directions are shown in Figure 2.1, and

$$\nu_{21} = \nu_{12}\left(\frac{E_{22}}{E_{11}}\right)$$

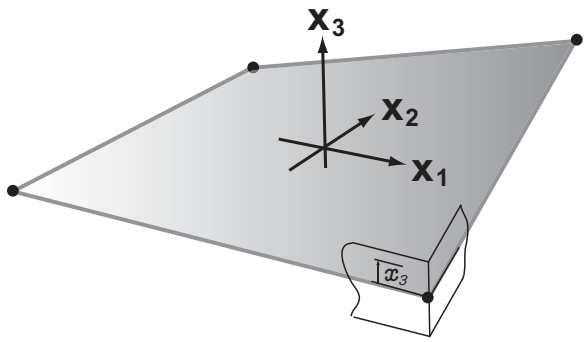

Figure 2.1: Mid-plane of a 4-noded shell element and local coordinate system.

In both shell formulations, the stresses $\boldsymbol{\sigma}$ in a laminated composite element, which is composed of one of more layers of the orthotropic material, are obtained from the mid-plane stresses and strains using classical lamination theory:

$$\boldsymbol{\sigma} = \boldsymbol{C}(\boldsymbol{\epsilon} - x_3\boldsymbol{\chi}) \tag{2.21}$$

where $\boldsymbol{\epsilon}$ is the vector of mid-plane strains, x_3 is the thickness coordinate measured from the mid-plane as indicated in Figure 2.1, and $\boldsymbol{\chi}$ is the vector of curvatures at the mid-plane. Equation (2.21), which represents the constitutive law for the composite element, is incorporated when formulating the equations of motions using the updated Lagrangian (UL) approach.

CHAPTER III

The Approximate Aerodynamic Model

The unsteady loads generated by representative MAV wings are obtained using an approximate aerodynamic model that was originally developed in Refs. [62, 64]. Several modifications to the original formulation to incorporate wing flexibility, effect of Reynolds number, and free stream velocity due to forward flight, have been introduced in this dissertation. The final version of the aerodynamic formulation is described in this chapter. The assumptions and limitations of the original formulation, as well as the modifications introduced, are carefully identified so that the improvements are clear.

3.1 Summary of the Original Model

The aerodynamic model described in Refs. [62, 64] consists of two components: (1) a discrete vortex based airfoil theory that incorporates LEVs and a free wake model, and (2) application of the airfoil theory to rigid insect-like flapping wings in hover.

The airfoil theory, based on the approach originally proposed by von Karman and Sears [90], involves representing the bound and shed vorticity in an airfoil-wake system using vortex pairs. The momentum per unit span of the system is obtained as the sum of the momentum of the vortex pairs. The expressions for aerodynamic lift

and moment in Ref. [90] were derived for thin airfoils undergoing small amplitude pitch-plunge motions, assuming attached flow over the airfoil and a planar (flat) wake. In Refs. [65, 67], the classical approach [90] was generalized to include thick cambered airfoils undergoing large amplitude pitch, plunge, and lead-lag motions, and a discrete vortex based free wake model. References [62, 64] extended the formulation described in Refs. [65, 67] to include the effect of LEVs, and applied the airfoil theory in a strip theory manner to compute the aerodynamic loads generated by a flapping wing. An overview of the formulation [62, 64] follows.

3.1.1 Overview of the Aerodynamic Formulation

The overall approach is summarized in Figure 3.1. First, the wing is divided into several spanwise stations, as shown in Figure 3.2, where each section is represented as an airfoil. For each airfoil, an airfoil-wake surface that captures the airfoil degrees of freedom (DOF), and approximates the geometry of the shed wake, is identified. Next, the airfoil and the airfoil-wake surface are transformed to a circle in the complex plane using a conformal mapping. Thus, the airfoil bound and shed wake vorticity are computed on the complex plane. The quasi-steady component of vorticity is obtained by neglecting the effect of the shed wake. The strength of shed vorticity is computed by enforcing a stagnation condition at the leading edge (LE) and a Kutta condition at the trailing edge (TE). The airfoil bound vorticity is obtained as a sum of the quasi-steady and wake-induced vorticity on the airfoil. Next, the vorticity in the complex plane is transformed back to the airfoil-wake surface (physical plane) using an inverse transform. The unsteady loads acting on the airfoil are obtained from the total vorticity. Finally, the shed vorticity is convected using the Rott-Birkhoff equation, which is derived from Biot-Savart law for two dimensional flow.

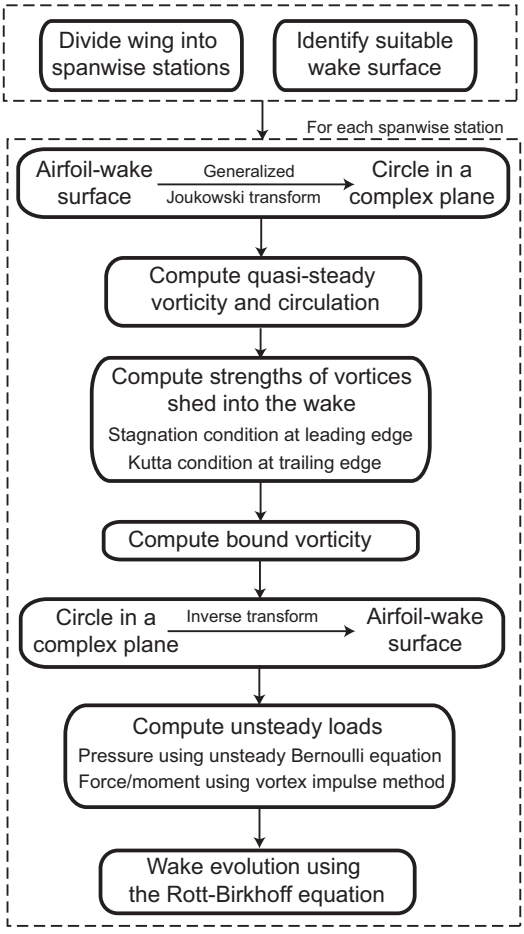

Figure 3.1: Schematic of the aerodynamic formulation.

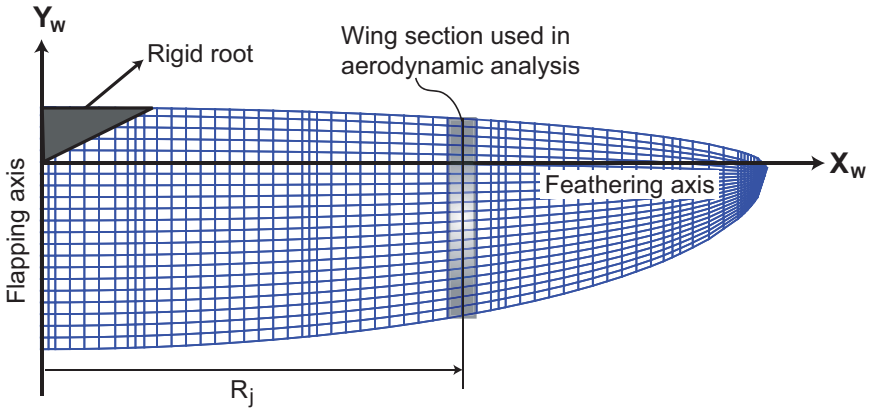

Figure 3.2: Spanwise sections and wing-fixed axes.

3.1.2 Assumptions

Important assumptions and limitations of the aerodynamic model developed in Refs. [62, 64] are summarized below:

1. The wings are rigid, thin (zero thickness), and planar (flat plate).
2. The onset of flow separation, and the separation point, are assumed in an ad hoc manner. The flow is assumed to be either attached or separated at all times.
3. The formulation is based on potential flow (inviscid, irrotational, and incompressible).
4. The aerodynamic interaction between the various wing sections is neglected.
5. The effects of spanwise flow and tip vortices are not modeled.
6. The spanwise stations on the wing are described by circular arcs called radial chords, as shown in Figure 3.3. Reference [62] justifies the use of radial chords by the arguing that, due to the flapping motion of the wing, spanwise sections that are viewed by the oncoming flow are better approximated using a radial chord than a straight chord.
7. The airfoil and its shed wake are confined to the NC that is described by the motion of the airfoil.
8. The effect of a free stream velocity due to forward flight is not incorporated during implementation. Consequently, the model described in Refs. [62, 64] is limited to flapping wings in hover.
9. The unsteady aerodynamic loads are computed using the vortex impulse method. This approach, which yields the integrated aerodynamic force and moment on the airfoil, is unsuitable for aeroelastic analyses involving plate- or shell-like structures that require pressure loading on the structure.

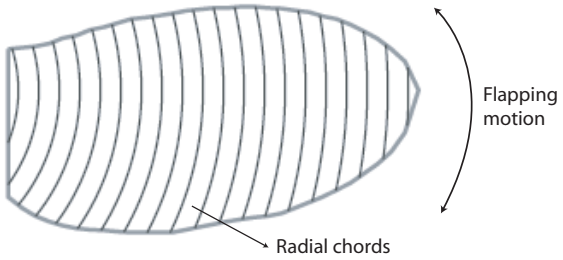

Figure 3.3: Radial chords used in the original approach.

3.1.3 Modifications Introduced

The modifications incorporated in the current study, including the sections of this thesis where they are described are:

1. Wing flexibility is incorporated using a time dependent radius of the airfoil-wake surface (Section 3.2.2). Effect of chordwise flexibility is incorporated in two steps: (1) calculating the zero lift angle due to camber (Eq. (3.2)) and (2) including airfoil velocities in the calculation of the quasi-steady vorticity (Section 3.2.3).

2. Effect of free stream velocity due to forward flight is incorporated (Section 3.2.3).

3. The effect of Reynolds number is incorporated in a partial manner by including the effect of viscosity in the expression of induced velocity due to shed vorticity (Sections 3.2.5, 3.2.6, and 3.3.2).

4. The unsteady Bernoulli equation is used to calculate the aerodynamic pressure on the airfoil, as described in Section 3.3.2. Thus, the aerodynamic model is suitable for aeroelastic analysis of wings modeled using plate or shell elements.

5. In Refs. [62, 64], the inverse of the conformal mapping was obtained using an asymptotic approach that was described in Ref. [67]. In the current study, the inverse is calculated using a direct approach (Page 58).

6. The spanwise stations on the wing are assumed to be straight and normal to the feathering axis of the wing, as shown in Figure 3.2.

3.2 Description of the Modified Approach

The modified formulation, and its implementation for flapping wings in hover and forward flight, closely follow the approach described in Section 3.1.1 and shown in Figure 3.1 and are described next.

Definition of the Airfoil-Wake Surface

Wing kinematics of biological flyers, in both hover and forward flight, consists of a predominant sweep or flap motion in the stroke plane (SP), pitching about the feathering axis, and a comparatively small elevation angle, as indicated in Figure 1.3 [21]. Therefore, the feathering axis of the wing is assumed to move on the stroke plane (SP) [62] and the surface described by the airfoil motion is a cylinder that is normal to the stroke plane; this normal cylinder (NC) is depicted in Figures 3.4 and 3.5.

In hover [62], the shed wake is assumed to be confined to the NC; therefore, NC is a convenient choice for the airfoil-wake surface. For the case of forward flight, the vortices shed into the wake are carried away with the free stream due to velocity of forward flight and therefore a suitable approximation to the wake surface has to be identified.

3.2.1 Extension to Forward Flight

Forward flight is characterized by a free stream velocity vector assumed to lie in the $Y_{SP} - Z_{SP}$ plane as depicted in Figure 3.4. A complete description of the free stream velocity involves two independent parameters u_∞ and v_∞, which are defined

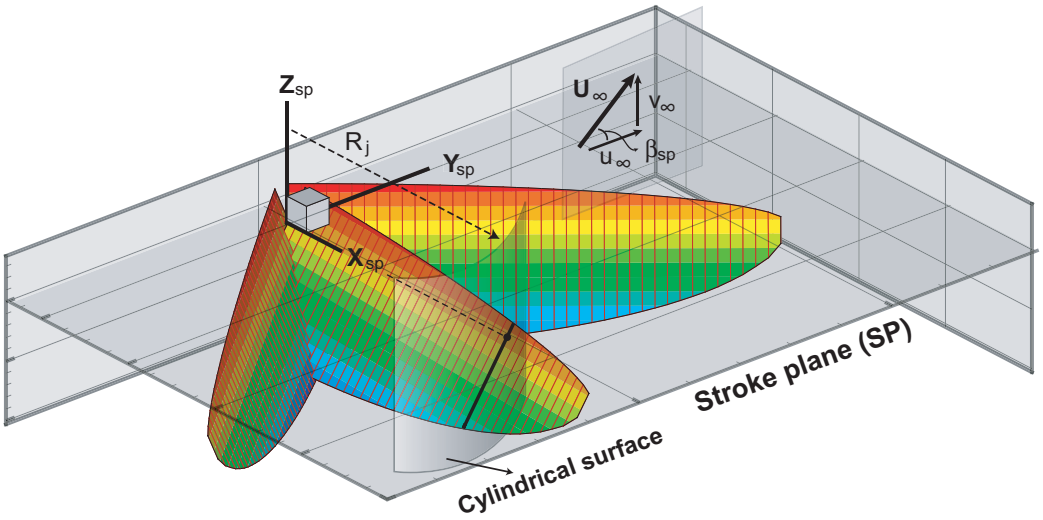

Figure 3.4: Coordinate system that is fixed to the stroke plane. Free stream velocity vector and cylindrical surface are also shown.

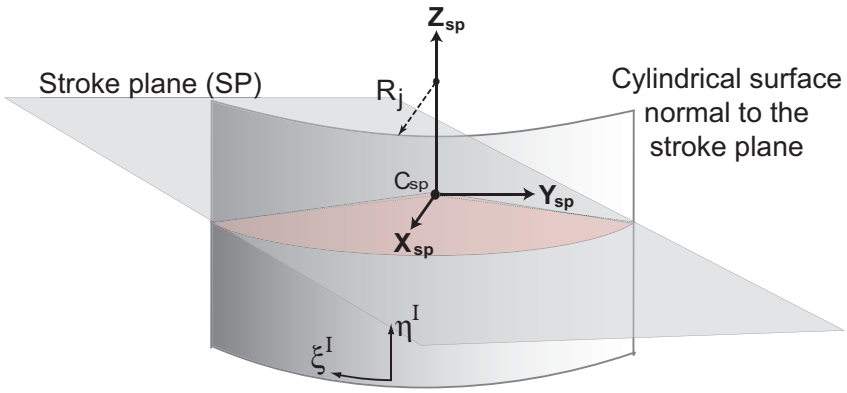

Figure 3.5: Normal cylinder described by the wing section.

as positive along Y_{SP} and Z_{SP} respectively. These quantities are determined from the tip speed, advance ratio, and stroke plane inclination angle, using Eq. (3.1).

$$\mu = \frac{-u_\infty}{U_{tip}} \quad \text{so that} \quad u_\infty = -\mu U_{tip} \quad \text{and} \quad v_\infty = u_\infty \tan\left(\beta_{sp}\right) \tag{3.1}$$

where u_∞, v_∞, and β_{sp} are shown in Figure 3.4. For the direction of flight assumed in this study, indicated in Figure 1.3, u_∞ and v_∞ are negative due to the sign convention adopted to describe the free stream velocity. The advance ratio is defined as a positive number. Therefore, the negative sign in Eq. (3.1) ensures that $\mu > 0$ yields negative values of u_∞ and v_∞.

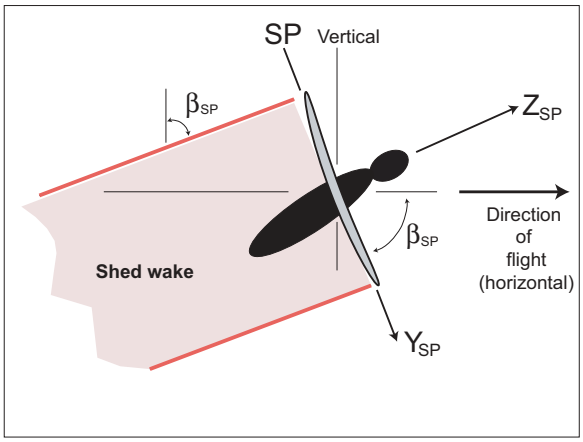

Figure 3.6: Flapping wing vehicle in forward flight. Shaded region indicates shed wake surface.

As mentioned earlier, experimental observations on live flyers suggest that a transition from hover to forward flight includes tilting the SP. It is expected that a wake surface suitable for wings in forward flight is tilted with respect to the free stream velocity in a similar manner. In this study, it is assumed that the wake surface is cylindrical and is tilted such that it remains normal to the SP as depicted in Figure 3.6. Thus, the NC, which is used for hover, is also used to approximate the geometry of the shed wake in forward flight. The effect of free stream due to forward flight

is incorporated by modifying the expressions used to determine the quasi-steady component of vorticity and the vortex wake model as described later.

Airfoil Coordinate Systems and Geometric Parameters

Several rectangular coordinate systems, which are defined on the flattened NC, are used in the analysis of each airfoil section. These coordinate systems, shown in Figures 3.7 and 3.8, are listed below, where the unit vectors corresponding to the axes are denoted by $\hat{\boldsymbol{e}}$ with an appropriate subscript:

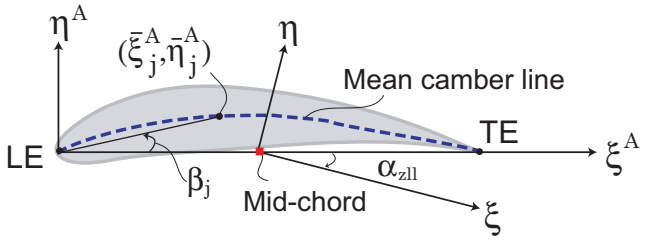

Figure 3.7: Coordinate systems used in the computation of airfoil camber.

1. (ξ^A, η^A): LE fixed coordinate system. Origin at LE; $\hat{\boldsymbol{e}}_{\xi^A}$ along the chord; $\hat{\boldsymbol{e}}_{\eta^A}$ normal to the chord; identified by superscript A.

2. (ξ, η): Zero lift coordinate system. Origin at the mid-chord; $\hat{\boldsymbol{e}}_{\xi^A}$ along the zero lift line (ZLL); $\hat{\boldsymbol{e}}_{\eta^A}$ normal to ZLL.

3. (ξ^I, η^I): Stationary coordinate system fixed to the NC; also shown in Figure 3.5. $\hat{\boldsymbol{e}}_{\xi^I}$ is parallel to the stroke plane; $\hat{\boldsymbol{e}}_{\eta^I}$ is parallel to Z_{SP}; identified by superscript I.

4. (ξ^{nr}, η^{nr}): Non-rotating coordinate system that translates with the airfoil. Origin at the intersection of the feathering axis of the wing and the normal cylinder. $\hat{\boldsymbol{e}}_{\xi^{nr}}$ and $\hat{\boldsymbol{e}}_{\eta^{nr}}$ are parallel to the stroke plane and $\hat{\boldsymbol{e}}_{\eta^I}$ respectively; identified by superscript nr.

5. (ξ^{fa}, η^{fa}): Coordinate system fixed to the center of rotation of the airfoil. Origin at the intersection of the feathering axis of the wing and the normal cylinder. $\hat{\boldsymbol{e}}_{\xi^{fa}}$ and $\hat{\boldsymbol{e}}_{\eta^{fa}}$ are parallel to $\hat{\boldsymbol{e}}_{\xi}$ and $\hat{\boldsymbol{e}}_{\eta}$ respectively; identified by superscript fa.

6. Complex plane ($\mathcal{Z}$): Obtained via transformation of $\xi - \eta$; an airfoil of chord c is transformed to a circle of radius R_0 so that polar coordinates, i.e. (R_0, θ), are used to identify points on the airfoil. The LE is located at $(-R_0, \pi)$ and TE is located at $(R_0, 0)$.

An important step in the aerodynamic formulation is the transformation of the airfoil to a circle on the complex plane via conformal mapping, the coordinates of the airfoil and shed wake referred to the $\xi - \eta$ coordinate system are transformed. Therefore, the zero lift line is identified as follows. For each airfoil section, $(\bar{\xi}_j^A, \bar{\eta}_j^A)$, $j = 1, ..., n_c$, denotes coordinates of the mean camber line of the airfoil as shown in Figure 3.7, and the zero-lift angle of attack, denoted by α_{zll}, is obtained from thin airfoil theory (pp. 68, Ref. [91]) as follows :

$$\alpha_{zll} = -\frac{2}{\pi} \sum_{j=2}^{n_c} \frac{\bar{\eta}_j^A}{c} \frac{\Delta\beta_j}{(1 + \cos(\beta_j))} \tag{3.2}$$

where $\beta_j = \tan^{-1}(\bar{\eta}_j^A / \bar{\xi}_j^A)$; $\beta_1 = 0$; and $\Delta\beta_j = \beta_j - \beta_{j-1}$. Then, $(\hat{\boldsymbol{e}}_{\xi}, \hat{\boldsymbol{e}}_{\eta})$ is obtained from $(\hat{\boldsymbol{e}}_{\xi^A}, \hat{\boldsymbol{e}}_{\eta^A})$ by a rotation of α_{zll} about $\left(\hat{\boldsymbol{e}}_{\eta^A} \times \hat{\boldsymbol{e}}_{\xi^A}\right)$ followed by a translation of the origin to the mid-chord.

3.2.2 Airfoil Degrees of Freedom and Spanwise Flexibility

Each airfoil has three degrees of freedom (DOF) that are defined in $\xi^I - \eta^I$ on the flattened NC as shown in Figure 3.8; these are lead-lag (l), plunge (h), and pitch (α) respectively. The lead-lag and plunge DOFs are positive along $\hat{\boldsymbol{e}}_{\xi^I}$ and $\hat{\boldsymbol{e}}_{\eta^I}$ respectively, and α is positive clockwise, as indicated in Figure 3.8. The airfoil DOFs and corresponding velocities are obtained from the structural dynamic model

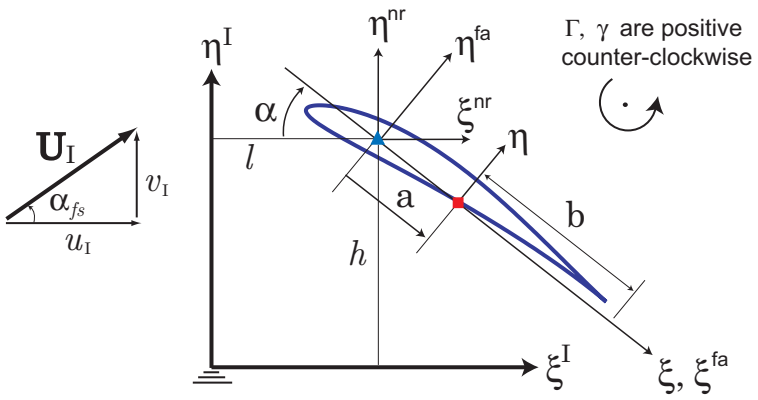

Figure 3.8: Degrees of freedom of the airfoil and coordinate systems used.

at each time step. Therefore, these quantities include the effect of wing deformation in addition to the effect of the wing kinematics. Spanwise deformation of the wing also causes a change in the radius of the NC associated with each airfoil. The change in radius due to flexibility is incorporated in an approximate manner.

Let R_j^0 and R_j^t denote the radial locations of a wing section at the start of the motion and at some subsequent time t as shown in Figure 3.9. An average radius of the NC at time t, which is used to calculate the distances on the flattened NC, is defined by

$$\bar{R}_j^t = 0.5\left(R_j^0 + R_j^t\right) \tag{3.3}$$

Geometric Parameters

The geometric parameters of the each airfoil required for the computation of the aerodynamic loads are: the radius of the circle in the complex plane (R_0), the camber (σ) and the thickness (τ) parameters. In the current study, the airfoil thickness is prescribed and assumed to be constant and the camber is approximated from the zero lift angle. Subsequently, τ and σ are calculated following the description given in pp

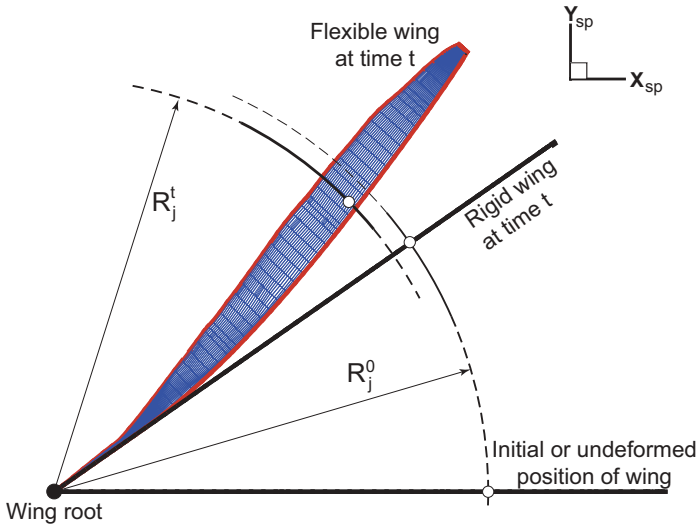

Figure 3.9: Top view of stroke plane showing the time dependent radius of normal cylindrical surface.

479-484, Ref. [92], as shown in Eq (3.4).

$$\tau = \frac{t_{h,max}^{af}}{2.6} \qquad \text{and} \qquad \sigma = -\frac{c \tan \alpha_{zll}}{4} \tag{3.4}$$

The procedure outlined above approximates a cambered airfoil as a circular arc.

The Generalized Joukowski Transformation

The conformal mapping that relates a circle to a Joukowski airfoil [62] is given by

$$\zeta = z + \frac{(1-\varepsilon)R_0^2}{z} + \frac{\varepsilon R_0^3}{2z^2} \tag{3.5}$$

where $\boldsymbol{\zeta} = \xi + \imath\eta$, $\boldsymbol{z} = R_0 e^{\imath\theta}$, and $\boldsymbol{\varepsilon} = (\tau - \imath\sigma)/R_0$. Substituting expressions for $\boldsymbol{\zeta}$, $\boldsymbol{z}$, and $\boldsymbol{\varepsilon}$, into Eq. (3.5) one obtains

$$\begin{aligned} \xi &= 2R_0\cos\theta + \sigma(\sin\theta - \frac{1}{2}\sin 2\theta) - \tau(\cos\theta - \frac{1}{2}\cos 2\theta) \\ \eta &= \tau(\sin\theta - \frac{1}{2}\sin 2\theta) + \sigma(\cos\theta - \frac{1}{2}\cos 2\theta) \end{aligned} \tag{3.6}$$

Substituting $\theta = 0$ and $\theta = \pi$ yields the coordinates of the trailing and leading edges:

$$(\xi_{te}, \eta_{te}) = (2R_0 - \frac{1}{2}\tau, \frac{1}{2}\sigma) \qquad \text{and} \qquad (\xi_{le}, \eta_{le}) = (-2R_0 + \frac{3}{2}\tau, -\frac{3}{2}\sigma) \tag{3.7}$$

The airfoil chord is defined as

$$c = \sqrt{(\xi_{le} - \xi_{te})^2 + \left(\eta_{le} - \eta_{te}\right)^2} \tag{3.8}$$

Substituting Eq. (3.7) into Eq. (3.8) and simplifying, one obtains

$$R_0 = \frac{1}{4}\sqrt{c^2 - 4\sigma^2} + \frac{1}{2}\tau \tag{3.9}$$

where the chord is calculated from the structural dynamic model as

$$c = \sqrt{\left(\bar{\xi}_1^A - \bar{\xi}_{n_c}^A\right)^2 + \left(\bar{\eta}_1^A - \bar{\eta}_{n_c}^A\right)^2} \tag{3.10}$$

Subsequently, the bound and shed vorticity and circulation are computed on this circle in the complex plane.

3.2.3 Quasi-steady Vorticity and Circulation

Quasi-steady vorticity is the sum of two components: (a) a *free stream* component that is computed from the instantaneous angle of attack and free stream velocity, and (b) an *unsteady* component that is computed from airfoil velocities.

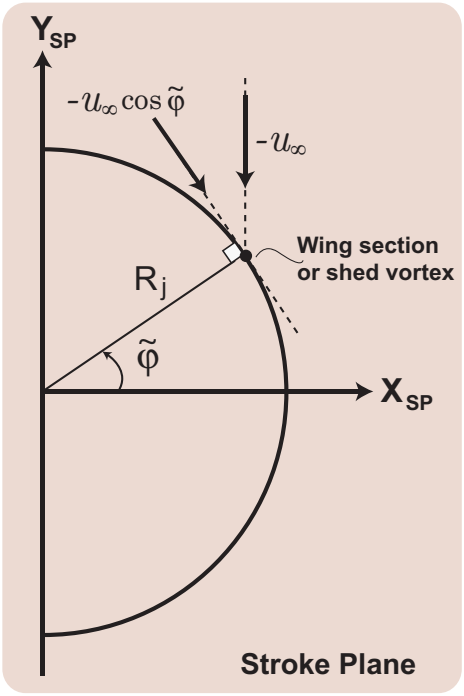

Figure 3.10: Component of u_∞ normal to the instantaneous position of the wing. .

Free stream component of vorticity

The vorticity and circulation due to a free stream, derived in Refs. [65, 67], are

$$\begin{aligned} \gamma_{fs}(\theta,t) &= -2u_I\Big[\sin(\theta-\alpha)+\sin(\alpha)\Big] \\ \Gamma_{fs}(t) &= -4\pi R_0 u_I \sin(\alpha) \end{aligned} \tag{3.11}$$

where the vorticity and circulation are positive in the counter-clockwise direction as indicated in Figure 3.8. In Ref. [62], the analysis was limited to hover; therefore, it was assumed that $u_I \equiv 0$ and Eq. (3.11) did not contribute to the quasi-steady component of vorticity. In the current study, the effect of free stream velocity is incorporated into Eq. (3.11). The free stream velocity vector, and its magnitude, at each wing section

are given by

$$\begin{aligned} \boldsymbol{U}_I &= -u_\infty \cos\tilde{\varphi}_w \, \hat{\boldsymbol{e}}_{\xi^I} + v_\infty \hat{\boldsymbol{e}}_{\eta^I} \\ U_I &= \left|\boldsymbol{U}_I\right| = \sqrt{\left(u_\infty \cos\tilde{\varphi}_w\right)^2 + v_\infty^2} \end{aligned} \tag{3.12}$$

where $\tilde{\varphi}$ is depicted in Figure 3.10 and subscript w indicates wing section. The instantaneous angle of attack of the airfoil, which is equal to the angle between the free stream velocity vector and $\hat{\boldsymbol{e}}_\xi$ is shown in Figure 3.8 and is given by:

$$\alpha_{tot} = \alpha + \alpha_{fs} \qquad \text{where} \qquad \alpha_{fs} = \tan^{-1}\left(\frac{v_I}{u_I}\right) = \tan^{-1}\left(-\frac{v_\infty}{u_\infty \cos\tilde{\varphi}_w}\right)$$

Thus, the modified expressions for vorticity and circulation due to the free stream velocity and angle of attack are given by

$$\begin{aligned} \gamma_{fs}(\theta,t) &= -2U_I\left[\sin(\theta - \alpha - \alpha_{fs}) + \sin\left(\alpha + \alpha_{fs}\right)\right] \\ \Gamma_{fs}(t) &= -4\pi R_0 U_I \sin\left(\alpha + \alpha_{fs}\right) \end{aligned} \tag{3.13}$$

Vorticity due to Airfoil Velocities

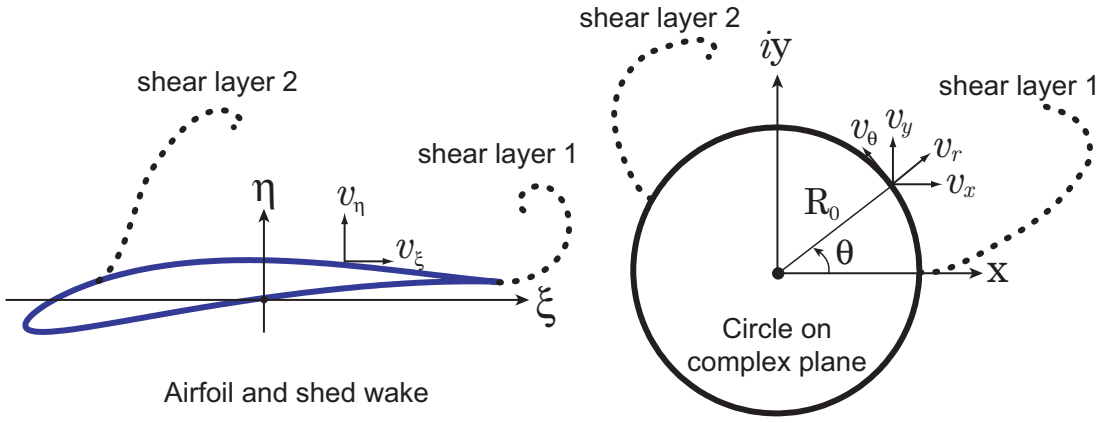

Figure 3.11: Airfoil and corresponding circle showing shear layers.

The unsteady component of vorticity is computed by enforcing the normal flow boundary condition on the circle. Derivation for a rigid airfoil is given in Ref. [62], and the extension for the flexible airfoil case is described next. The components of velocities on the surface of a flexible airfoil in the $\xi - \eta$ coordinate system, shown in Figure 3.8, are given by

$$\begin{aligned} v_\xi^{flex} &= v_\xi^{rigid} + \Delta v_\xi^{flex} \\ v_\eta^{flex} &= v_\eta^{rigid} + \Delta v_\eta^{flex} \end{aligned} \tag{3.14}$$

where the velocities for a rigid airfoil [62] are given by

$$\begin{aligned} v_\xi^{rigid} &= \dot{l}\cos\alpha - \dot{h}\sin\alpha + \eta\dot{\alpha} \\ v_\eta^{rigid} &= \dot{l}\sin\alpha + \dot{h}\cos\alpha - (\xi + a)\dot{\alpha} \end{aligned} \tag{3.15}$$

The fluid does not penetrate the surface of the airfoil; therefore, the normal velocity of the fluid on the surface of the airfoil is given by Eq. (3.14). The polar components of velocity on the circle are obtained from the corresponding Cartesian components on the airfoil (shown in Figure 3.11) as follows:

$$\begin{aligned} v_r - \imath v_\theta = (v_x - \imath v_y)e^{\imath\theta} &= (v_\xi^{flex} - \imath v_\eta^{flex})\frac{d\boldsymbol{\zeta}}{d\boldsymbol{z}}e^{\imath\theta} \\ &= (\underline{A}v_\xi^{flex} + \underline{B}v_\eta^{flex}) + \imath(\underline{B}v_\xi^{flex} - \underline{A}v_\eta^{flex}) \end{aligned} \tag{3.16}$$

where

$$\begin{aligned} \underline{A} &= \frac{1}{R_0}[\tau(\cos\theta - \cos 2\theta) - \sigma(\sin\theta - \sin 2\theta)] \\ \underline{B} &= \frac{1}{R_0}[2R_0\sin\theta - \tau(\sin\theta - \sin 2\theta) - \sigma(\cos\theta - \cos 2\theta)] \end{aligned} \tag{3.17}$$

Thus, the normal velocity of the fluid on the circle is given by

$$v_r(\theta,t)\Big|_{us}^{flex} = (\underline{A}v_\xi^{rigid} + \underline{B}v_\eta^{rigid}) + (\underline{A}\Delta v_\xi^{flex} + \underline{B}\Delta v_\eta^{flex}) \tag{3.18}$$

The tangential component of fluid velocity on the circle is obtained from the radial velocity by applying conjugate function theory [92, 93]. Then,

$$\begin{aligned} v_\theta(\theta,t)\Big|_{us}^{flex} &= \frac{-1}{2\pi}\oint_0^{2\pi} v_r(\varsigma,t)\Big|_{us}^{flex}\cot\left(\frac{\varsigma-\theta}{2}\right)d\varsigma \\ &= v_\theta(\theta,t)\Big|_{us}^{rigid} + \Delta v_\theta(\theta,t)\Big|_{us}^{flex} \end{aligned} \tag{3.19}$$

where $v_\theta(\theta,t)\Big|_{us}^{rigid}$ was derived in Ref. [62] as

$$\begin{aligned} v_\theta(\theta,t)\Big|_{us}^{rigid} = \frac{1}{R_0}\Big[& -A_1\cos\theta - (A_2 + \frac{1}{2}A_7)\cos 2\theta + A_3\sin\theta + \\ & (A_4 - \frac{1}{2}A_5 + \frac{1}{2}A_6)\sin 2\theta - A_8\sin\theta\cos 2\theta + \\ & A_9\sin\theta\sin 2\theta - A_{10}\cos\theta\cos 2\theta + A_{11}\cos\theta\sin 2\theta\Big] \end{aligned} \tag{3.20}$$

where A_1 to A_{11}, derived in Ref. [62], are given as follows.

$$
\begin{aligned}
A_1 &= -\sigma(\dot{l}\cos\alpha - \dot{h}\sin\alpha) + (2R_0 - \tau)(\dot{l}\sin\alpha + \dot{h}\cos\alpha) + a(\tau - 2R_0)\dot{\alpha} \\
A_2 &= \sigma(\dot{l}\cos\alpha - \dot{h}\sin\alpha) + \tau(\dot{l}\sin\alpha + \dot{h}\cos\alpha) - a\tau\dot{\alpha} \\
A_3 &= \tau(\dot{l}\cos\alpha - \dot{h}\sin\alpha) - \sigma(\dot{l}\sin\alpha + \dot{h}\cos\alpha) + a\sigma\dot{\alpha} \\
A_4 &= -\tau(\dot{l}\cos\alpha - \dot{h}\sin\alpha) + \sigma(\dot{l}\sin\alpha + \dot{h}\cos\alpha) - a\sigma\dot{\alpha} \\
A_5 &= -2R_0\sigma\dot{\alpha} \\
A_6 &= 2R_0\sigma\dot{\alpha} \\
A_7 &= 4R_0(\tau - R_0)\dot{\alpha} \\
A_8 &= R_0\sigma\dot{\alpha} \\
A_9 &= -\frac{1}{2}(\tau^2 + \sigma^2 + 2R_0\tau)\dot{\alpha} \\
A_{10} &= \frac{1}{2}(\tau^2 + \sigma^2 - 4R_0\tau)\dot{\alpha} \\
A_{11} &= -2R_0\sigma\dot{\alpha}
\end{aligned}
\tag{3.21}
$$

Note that

$$
\Delta v_\theta(\theta,t)\Big|_{us}^{flex} = \frac{-1}{2\pi}\oint_0^{2\pi}\left(\underline{A}\Delta v_\xi^{flex} + \underline{B}\Delta v_\eta^{flex}\right)\cot\left(\frac{\varsigma-\theta}{2}\right)d\varsigma \tag{3.22}
$$

In this study, Δv_ξ^{flex} and Δv_η^{flex} are assumed to be averaged quantities that are independent of the ς in Eq. (3.22). However, the contributions are computed by substituting the time dependent values of these components at each time step to capture the variation of velocities in an approximate manner. It is important to note that this assumption has to be re-examined if the contribution of chordwise velocities to the vorticity is comparable to the vorticity due to rigid body motion and wake

interactions.

$$\Delta v_\theta(\theta,t)\big|_{us}^{flex} = -\frac{1}{2\pi}\left(\oint_0^{2\pi} \underline{A}\cot\left(\frac{\varsigma-\theta}{2}\right)d\varsigma\right)\Delta v_\xi^{flex} - \frac{1}{2\pi}\left(\oint_0^{2\pi} \underline{B}\cot\left(\frac{\varsigma-\theta}{2}\right)d\varsigma\right)\Delta v_\eta^{flex} \tag{3.23}$$

The evaluation of the integrals in Eq. (3.23) is described in Appendix A. The final form of Eq. (3.23) is obtained as

$$\begin{aligned}\Delta v_\theta(\theta,t)\big|_{us}^{flex} = &\frac{1}{R_0}\Big[\tau\big(\sin\theta-\sin 2\theta\big)+\sigma\big(\cos\theta-\cos 2\theta\big)\Big]\Delta v_\xi^{flex}(\theta,t) \\ &+\frac{1}{R_0}\Big[-2R_0\cos\theta+\tau\big(\cos\theta-\cos 2\theta\big)-\sigma\big(\sin\theta-\sin 2\theta\big)\Big]\Delta v_\eta^{flex}(\theta,t)\end{aligned} \tag{3.24}$$

Combining Eqs. (3.19), (3.20), and (3.24), the expression for the tangential velocity of the fluid on the surface of the airfoil is given as:

$$\begin{aligned}v_\theta(\theta,t)\big|_{us}^{flex} = &\frac{1}{R_0}\Big[-A_1\cos\theta-(A_2+\frac{1}{2}A_7)\cos 2\theta+A_3\sin\theta+(A_4-\frac{1}{2}A_5+\frac{1}{2}A_6)\sin 2\theta \\ &-A_8\sin\theta\cos 2\theta+A_9\sin\theta\sin 2\theta-A_{10}\cos\theta\cos 2\theta+A_{11}\cos\theta\sin 2\theta\Big] \\ &+\frac{\Delta v_\xi^{flex}}{R_0}\Big[\tau(\sin\theta-\sin 2\theta)+\sigma(\cos\theta-\cos 2\theta)\Big]+ \\ &+\frac{\Delta v_\eta^{flex}}{R_0}\Big[-2R_0\cos\theta+\tau(\cos\theta-\cos 2\theta)-\sigma(\sin\theta-\sin 2\theta)\Big]\end{aligned} \tag{3.25}$$

Subsequently, the vorticity on the circle [62] is obtained as

$$\gamma_{us}^{flex}(\theta,t) = v_\theta(\theta,t)\big|_{us}^{flex} + \frac{\Gamma_0}{2\pi R_0} \tag{3.26}$$

where

$$\Gamma_0 = 2\pi\left[2R_0\left(\dot{l}\sin\alpha+\dot{h}\cos\alpha\right)+\dot{\alpha}\left(\frac{1}{2}\tau^2+\frac{1}{2}\sigma^2-2R_0(R_0+a)\right)\right]$$

3.2.4 Effect of Fluid Viscosity

In a viscous fluid, the influence of shed vorticity at a point decays with increase in distance as well as the age of the vortex. At sufficiently large Reynolds numbers, the temporal decay of the vortex strength is slow enough compared to the time of simulation so that one may assume that the strength of the vortex is constant with respect of time. However, this effect needs to re-examined at lower Reynolds number.

In this study, the decay of vortex strength is incorporated in the expression of induced velocity due to shed vorticity. From Ch. 13, Ref. [94], the induced velocity due to a Lamb-Oseen vortex, which arises as an exact solution of the NS equations for 2D viscous flow, is given by:

$$\begin{aligned} v_{ind}\Big|_{viscous} = v_{ind}\Big|_{inviscid}\left(1-e^{-\frac{r_v^2}{4\nu_\infty t_v}}\right) &= v_{ind}\Big|_{inviscid}\left(1-e^{-Re\frac{r_v^2}{4t_v}}\right) \qquad (3.27) \\ \text{and} \qquad \Gamma\Big|_{viscous} &= \Gamma\Big|_{inviscid}\left(1-e^{-\frac{r_v^2}{4\nu_\infty t_v}}\right) \end{aligned}$$

where r_v denotes the distance between the vortex and the point at which induced velocity is computed, t_v denotes the age of the vortex, and

$$Re = \frac{U_{ref}c}{\nu_\infty} \quad ; \quad \underline{r}_v = \frac{r_v}{c} \quad ; \quad \underline{t}_v = \frac{t_v U_{ref}}{c}$$

Incorporating this effect into the aerodynamic model modifies the constraint conditions used to determine the shed vorticity, the expressions used to computed wake induced and bound vorticity, the evolution of the wake, and the calculation of the pressure using the unsteady Bernoulli equation.

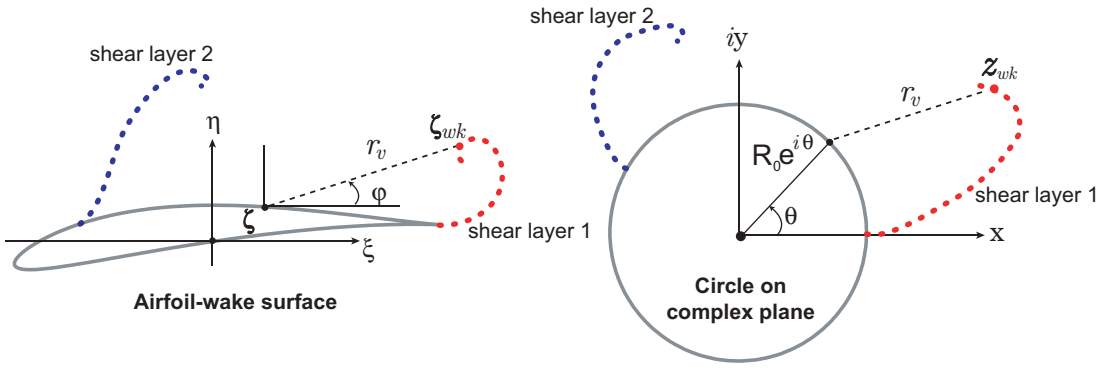

Figure 3.12: Distances and angles that are used in the computation of velocity potential.

3.2.5 Determination of Shed Vorticity

Following Ref. [62], the induced velocity on the circle due to an inviscid 2D vortex shed into the wake is:

$$v_{ind}(\theta,t)\Big|_{inviscid} = -\frac{1}{2\pi R_0}\oint_{wk}\mathscr{R}\left(\frac{\boldsymbol{z}_{wk}+R_0e^{\imath\theta}}{\boldsymbol{z}_{wk}-R_0e^{\imath\theta}}\right)d\Gamma_{wk} \tag{3.28}$$

where, $\mathscr{R}$ denotes real part, $wk = wk1 + wk2$, and $wk1$ and $wk2$ denote shear layers emanating from the airfoil shown in Figure 3.12. Combining Eqs. (3.27) and Eq. (3.28), the induced velocity becomes

$$\begin{aligned} v_{ind}(\theta,t)\Big|_{viscous} &= -\frac{1}{2\pi R_0}\oint_{wk}\left[\mathscr{R}\left(\frac{\boldsymbol{z}_{wk}+R_0e^{\imath\theta}}{\boldsymbol{z}_{wk}-R_0e^{\imath\theta}}\right)d\Gamma_{wk}\left(1-e^{-\frac{r_v^2}{4\nu_\infty t_v}}\right)\right] \\ &\text{where} \quad r_v = \left|\boldsymbol{z}_{wk}-R_0e^{\imath\theta}\right| \end{aligned} \tag{3.29}$$

where, r_v is depicted in Figure 3.12, and the effect of viscosity is included inside the integral on the right hand side (RHS). At each time step, the strengths of the vortices shed from the edges of the airfoil are determined from the Kutta condition at

the TE and a stagnation condition at the LE on the circle in the complex plane [62]. These constraint conditions on induced velocity, originally derived in Ref. [62] for inviscid flow, are based on the assumptions: a streamline that has separated at the LE re-attaches further downstream, and flow leaves the TE smoothly. Inclusion of the effect of viscosity modifies the expressions.

The stagnation condition at the LE:

$$\frac{1}{R_0}\left[A_1-\left(A_2+\frac{1}{2}A_7\right)+A_{10}\right]-2U_I\sin\left(\alpha+\alpha_{fs}\right) = \frac{1}{2\pi R_0}\oint_{wk}\left[\mathscr{R}\left(\frac{\boldsymbol{z}_{wk}-R_0}{\boldsymbol{z}_{wk}+R_0}\right)\mathrm{d}\Gamma_{wk}\left(1-e^{-\frac{r_v^2}{4\nu_\infty t_v}}\right)\right] \quad (3.30)$$

$$\text{where} \qquad r_v=|\boldsymbol{z}_{wk}+R_0|$$

The Kutta condition at the TE:

$$\Gamma_0=-\oint_{wk}\left[\mathscr{R}\left(\frac{\boldsymbol{z}_{wk}+R_0}{\boldsymbol{z}_{wk}-R_0}\right)\mathrm{d}\Gamma_{wk}\left(1-e^{-\frac{r_v^2}{4\nu_\infty t_v}}\right)\right] \quad \text{where} \quad r_v=|\boldsymbol{z}_{wk}-R_0| \quad (3.31)$$

where, the effect of viscosity is included inside the integrals on the RHS of Eqs. (3.30) and (3.31). In Eqs. (3.30) and (3.31), the positions of the most recent shed vortices as well as the strengths are unknown. The position vectors of the most recent shed vortices are determined using a vortex placement scheme in which shed vortices are placed at specified distances from the TE and LE [64]. Position vectors of the vortices shed at the end of the first time step are given by

$$\begin{aligned}\text{At the LE :} \qquad \boldsymbol{\zeta}^I\left(\mathrm{d}\Gamma_{wk2,1}\right) &= \boldsymbol{\zeta}^I_{le}-\frac{1}{2}\left(\boldsymbol{q}^I_{le}-\boldsymbol{U}_I\right)\Delta t\\ \text{At the TE :} \qquad \boldsymbol{\zeta}^I\left(\mathrm{d}\Gamma_{wk1,1}\right) &= \boldsymbol{\zeta}^I_{te}-\frac{1}{2}\left(\boldsymbol{q}^I_{te}-\boldsymbol{U}_I\right)\Delta t\end{aligned}$$

Position vectors of the vortices shed at any subsequent time step are given by:

$$\begin{aligned} \text{At the LE :} \qquad \boldsymbol{\zeta}^I\left(\mathrm{d}\Gamma_{wk2,j}\right) &= \boldsymbol{\zeta}^I_{le} - \frac{1}{3}\left(\boldsymbol{\zeta}^I_{le} - \boldsymbol{\zeta}^I\left(\Gamma_{wk2,j-1}\right)\right) \\ \text{At the TE :} \qquad \boldsymbol{\zeta}^I\left(\mathrm{d}\Gamma_{wk1,j}\right) &= \boldsymbol{\zeta}^I_{te} - \frac{1}{3}\left(\boldsymbol{\zeta}^I_{te} - \boldsymbol{\zeta}^I\left(\Gamma_{wk1,j-1}\right)\right) \end{aligned}$$

At any time step j, $\mathrm{d}\Gamma_{wk1,j}$ and $\mathrm{d}\Gamma_{wk2,j}$ are the only remaining unknowns [64]. The positions and strengths of the previously shed vortices are known; therefore, Eqs. (3.31) and (3.30) are sufficient to determine the shed vorticity. Solution of Eqs. (3.31) and (3.30), along with history of the previously shed vortices, yields the total vorticity shed into the wake. Subsequently, the wake induced vorticity on the circle is given by:

$$\gamma_{wi}(\theta,t)\Big|_{viscous} = -\frac{\Gamma_0}{2\pi R_0} - \frac{1}{2\pi R_0}\oint_{wk}\left[\mathscr{R}\left(\frac{\boldsymbol{z}_{wk} + R_0 \mathrm{e}^{\imath\theta}}{\boldsymbol{z}_{wk} - R_0\mathrm{e}^{\imath\theta}}\right)\mathrm{d}\Gamma_{wk}\left(1 - e^{-\frac{r_v^2}{4\nu_\infty t_v}}\right)\right] \qquad (3.32)$$

$$\text{where} \quad r_v = \left|\boldsymbol{z}_{wk} - R_0\mathrm{e}^{\imath\theta}\right|$$

The airfoil bound vorticity on the circle is obtained by combining Eqs. (3.13), (3.26), and (3.32):

$$\gamma_b = \gamma_{fs} + \gamma_{us}^{flex} + \gamma_{wi}\Big|_{viscous} \qquad (3.33)$$

The Inverse Joukowski Transform

Following the calculation of bound and shed vorticity in the complex plane, the positions and strengths of vortices are transformed from the complex plane to the airfoil wake surface. The velocities and vortex strengths are transformed:

$$\mathbf{q}(\boldsymbol{\zeta}) = \frac{\mathbf{q}(\boldsymbol{z})}{d\boldsymbol{\zeta}/d\boldsymbol{z}} \quad , \quad \gamma(\boldsymbol{\zeta}) = \frac{\gamma(\boldsymbol{z})}{d\boldsymbol{\zeta}/d\boldsymbol{z}} \quad \text{, and} \quad \Gamma(\boldsymbol{\zeta}) = \Gamma(\boldsymbol{z})$$

The positions of the vortices on the NC are obtained by solving the inverse of Eq (3.5) using the procedure described in Ref. [95] pp 178-180. The inverse of Eq (3.5) is given by

$$\tilde{\boldsymbol{z}}^3 + \mathbf{a}\tilde{\boldsymbol{z}}^2 + \mathbf{b}\tilde{\boldsymbol{z}} + \mathbf{c} = 0 \tag{3.34}$$

Note, in this equation the bold symbols denote complex quantities, and

$$\tilde{\boldsymbol{z}} = \frac{\boldsymbol{z}}{R_0} \quad , \quad \mathbf{a} = -\frac{\boldsymbol{\zeta}}{R_0} \quad , \quad \mathbf{b} = (1-\boldsymbol{\varepsilon}) \quad , \quad \text{and} \quad \mathbf{c} = \frac{\boldsymbol{\varepsilon}}{2} \tag{3.35}$$

The roots of Eq (3.34) are obtained as follows: First obtain

$$\mathbf{d} = \frac{\mathbf{a}^2 - 3\mathbf{b}}{9} \qquad \text{and} \qquad \mathbf{g} = \frac{2\mathbf{a}^3 - 9\mathbf{ab} + 27\mathbf{c}}{54} \tag{3.36}$$

Then

$$\mathbf{A} = -\left[\mathbf{g} + \sqrt{\mathbf{g}^2 - \mathbf{d}^3}\right] \tag{3.37}$$

where, the sign of the square root is chosen so that

$$\mathscr{R}\left(\mathbf{g}^* \sqrt{\mathbf{g}^2 - \mathbf{d}^3}\right) \geq 0 \tag{3.38}$$

Next compute

$$\mathbf{B} = \begin{cases} \mathbf{d}/\mathbf{A} & (|\mathbf{A}| \neq 0) \\ 0 & (|\mathbf{A}| = 0) \end{cases} \tag{3.39}$$

The roots of Eq. (3.34) are given by

$$\begin{aligned} \tilde{\boldsymbol{z}}_1 &= (\mathbf{A}+\mathbf{B}) - \frac{\mathbf{a}}{3} \\ \tilde{\boldsymbol{z}}_2 &= -\frac{1}{2}(\mathbf{A}+\mathbf{B}) - \frac{\mathbf{a}}{3} + \imath\frac{\sqrt{3}}{2}(\mathbf{A}-\mathbf{B}) \\ \tilde{\boldsymbol{z}}_3 &= -\frac{1}{2}(\mathbf{A}+\mathbf{B}) - \frac{\mathbf{a}}{3} - \imath\frac{\sqrt{3}}{2}(\mathbf{A}-\mathbf{B}) \end{aligned} \tag{3.40}$$

where, the root that corresponds to a given $\boldsymbol{\zeta}$ is $\tilde{\boldsymbol{z}}_j$, where $j = 1,2,3$, that has the maximum absolute value. This is illustrated by the following example. Consider a circle with $R_0 = 0.272$, $\tau = 0.0462$, and $\sigma = 0.0462$ as shown in Figure 3.13(a). The corresponding airfoil has $c = 1$ and is shown in Figure 3.13(b). The airfoil coordinates ($\boldsymbol{\zeta}$), obtained by substituting values of R_0, τ, and σ into Eq. (3.6), are used to calculate the corresponding inverse values ($\tilde{\boldsymbol{z}}$) using Eq. (3.40). For each $\boldsymbol{\zeta}$, the roots of the inverse equation are plotted in Figure 3.13(a). Two of the three roots lie inside the circle indicating that the correct root is the one that has maximum absolute value. Similar arguments apply when computing $\tilde{\boldsymbol{z}}$ for shed vortices.

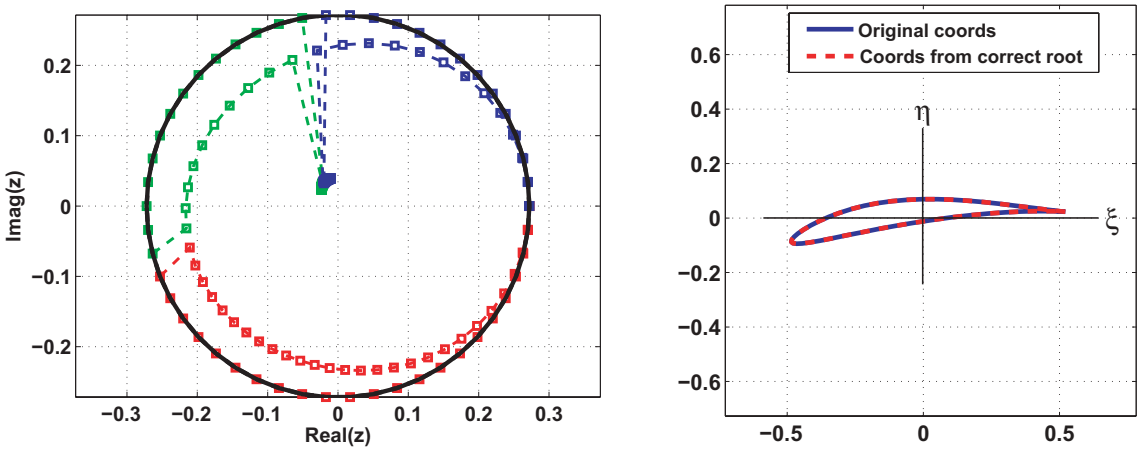

(a) Solid line indicates the circle. Squares indicate roots of the inverse transform.

(b) Original airfoil coordinates, and those generated using the correct root from the inverse transform.

Figure 3.13: Circle, corresponding airfoil, and roots of the inverse transform

3.2.6 The Vortex Wake Model

Vortices on the flattened NC are convected using the Rott-Birkhoff equation [94], which is derived from Biot-Savart law for two dimensional flow. The Rott-Birkhoff equation yields induced velocity at any point due to a vortex and it is implemented in

the $\xi^I - \eta^I$ coordinate system as shown in Eq. (3.41).

$$\mathbf{q}^*(\boldsymbol{\zeta}^I) = \sum_{j=1}^{\infty} \left[\frac{\mathrm{d}\Gamma_j}{2\pi\imath\left(\boldsymbol{\zeta}^I - \boldsymbol{\zeta}_j^I\right)} + (u_E - \imath v_E) \right] \tag{3.41}$$

where, $\boldsymbol{\zeta}_j^I \equiv \boldsymbol{\zeta}^I\left(\mathrm{d}\Gamma_j\right)$, ∞ indicates that the summation includes airfoil bound and all shed vortices in the airfoil-wake system, and u_E, v_E are components of the free stream velocity at each shed vortex. The effect of free stream velocity due to forward flight is incorporated by using

$$u_E = -u_\infty \cos\tilde{\varphi}_{\Gamma_j} \qquad \text{and} \qquad v_E = v_\infty \tag{3.42}$$

where $\tilde{\varphi}_{\Gamma_j}$ denotes the instantaneous sweep angle of the $\mathrm{d}\Gamma_j$, as depicted in Figure 3.10. Therefore, Eq. (3.41) yields

$$\mathbf{q}^*(\boldsymbol{\zeta}^I) = \sum_{j=1}^{\infty} \left[\frac{\mathrm{d}\Gamma_j}{2\pi\imath\left(\boldsymbol{\zeta}^I - \boldsymbol{\zeta}_j^I\right)} + \left(-u_\infty \cos\tilde{\varphi}_{\Gamma_j} - \imath v_\infty\right) \right] \tag{3.43}$$

Note that Eq. (3.43) becomes singular as $\left(\boldsymbol{\zeta}^I - \boldsymbol{\zeta}_j^I\right)$ approaches zero. Therefore, numerical implementation of Eq. (3.43) requires *de-singularization* of the vortex core, in which each discrete vortex is assumed to have a finite core radius. Adopting the de-singularization procedure used in Ref. [60], Eq. (3.43) is modified as follows:

$$\begin{aligned}
\mathbf{q}^*(\boldsymbol{\zeta}^I) &= \sum_{j=1}^{\infty} \left[\frac{\mathrm{d}\Gamma_j}{2\pi\imath\left(\boldsymbol{\zeta}^I - \boldsymbol{\zeta}_j^I\right)} \frac{\left(\boldsymbol{\zeta}^I - \boldsymbol{\zeta}_j^I\right)^*}{\left(\boldsymbol{\zeta}^I - \boldsymbol{\zeta}_j^I\right)^*} + \left(-u_\infty \cos\tilde{\varphi}_{\Gamma_j} - \imath v_\infty\right) \right] \\
&= \sum_{j=1}^{\infty} \left[\frac{\mathrm{d}\Gamma_j \left(\boldsymbol{\zeta}^I - \boldsymbol{\zeta}_j^I\right)^*}{2\pi\imath|\boldsymbol{\zeta}^I - \boldsymbol{\zeta}_j^I|^2} + \left(-u_\infty \cos\tilde{\varphi}_{\Gamma_j} - \imath v_\infty\right) \right] \\
&\approx \sum_{j=1}^{\infty} \left[\frac{\mathrm{d}\Gamma_k \left(\boldsymbol{\zeta}^I - \boldsymbol{\zeta}_j^I\right)^*}{2\pi\imath\left(r_c^2 + |\boldsymbol{\zeta}^I - \boldsymbol{\zeta}_j^I|^2\right)} + \left(-u_\infty \cos\tilde{\varphi}_{\Gamma_j} - \imath v_\infty\right) \right]
\end{aligned} \tag{3.44}$$

Incorporating the effect of viscosity, Eq. (3.44) yields

$$\mathbf{q}^*(\boldsymbol{\zeta}^I)\Big|_{viscous} \approx \sum_{j=1}^{\infty}\left[\frac{\mathrm{d}\Gamma_j\left(\boldsymbol{\zeta}^I-\boldsymbol{\zeta}_j^I\right)^*}{2\pi\imath\left(r_c^2+|\boldsymbol{\zeta}^I-\boldsymbol{\zeta}_j^I|^2\right)}\left(1-e^{-\frac{r_{v_j}^2}{4\nu_\infty t_{v_j}}}\right)+\left(-u_\infty\cos\tilde{\varphi}_{\Gamma_j}-\imath v_\infty\right)\right] \quad (3.45)$$

$$\text{where} \quad r_{v_j}=\left|\boldsymbol{\zeta}^I-\boldsymbol{\zeta}_j^I\right|$$

It was noted in Ref. [64] that the use of wake sub-iterations improves the quality of the solution when wake distortion due to wing-wake interaction is expected. Therefore, the Euler scheme, which was used in Ref. [64], is also used in the current study. In this scheme, the positions of the wake vortices are computed by performing several sub-iterations within each time step.

$$\boldsymbol{\zeta}^I(t+\Delta t)=\boldsymbol{\zeta}^I(t)+\sum_{j=1}^{n_{wksubit}}\mathbf{q}_j(t)\frac{\Delta t}{n_{wksubit}}$$

3.3 Calculation of Aerodynamic Loads

The unsteady aerodynamic loads can be calculated from the total vorticity using either the vortex impulse method or the unsteady Bernoulli equation. The two approaches are equivalent and derived from the Euler equations for irrotational flow; the derivations are summarized in Appendix B. The final expressions and implementation are presented next.

3.3.1 The Vortex Impulse Method

The vortex impulse method (VI) is based on Kelvin's impulse theorem that relates the aerodynamic force and moment due to a system of vortices to the impulse and moment of impulse of the vortices. Following Refs. [62, 65, 67, 90], the impulse and

moment of impulse of the vortex pairs that constitute the airfoil-wake system in a non-rotating coordinate system that is translating with the airfoil are given as follows:

$$\boldsymbol{I}^{nr} = \imath\rho_\infty \sum_{j=1}^{\infty} \mathrm{d}\Gamma_j \boldsymbol{\zeta}_j^{nr} \quad \text{and} \quad I_m^{nr} = \frac{\rho_\infty}{2} \sum_{j=1}^{\infty} \mathrm{d}\Gamma_j \left|\boldsymbol{\zeta}_j^{nr}\right|^2 \tag{3.46}$$

The force and moment on the airfoil, obtained in the non-rotating coordinate system, are given by:

$$\boldsymbol{F}^{nr} = \frac{d\boldsymbol{I}^{nr}}{dt} \qquad \text{and} \qquad M^{nr} = \frac{dI_m^{nr}}{dt} - \mathscr{I}(\boldsymbol{U}_0 \cdot \boldsymbol{I}^{nr}) \tag{3.47}$$

where $\mathscr{I}$ refers to the imaginary part and $\boldsymbol{U}_0 = (-u_I + \dot{l}) + \imath(-v_I + \dot{h})$ denotes the translational velocity of the coordinate system.

3.3.2 Unsteady Bernoulli Equation

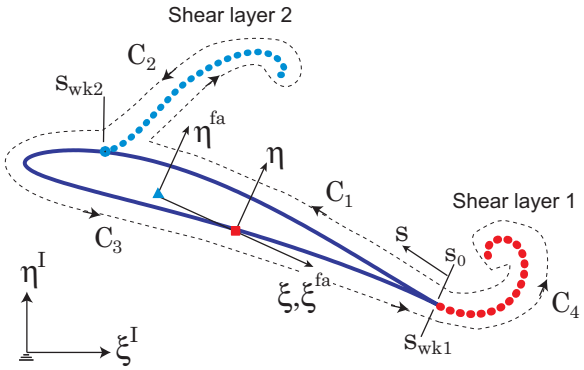

Figure 3.14: Contours of integration for computing velocity potential from bound and shed vorticity from an airfoil. For clarity, shed vortices are indicated by solid circles.

The unsteady Bernoulli principle relates the local pressure at any point to the velocity potential at that point. Following Ref. [61], the expression derived in the

$\xi^{fa}-\eta^{fa}$ coordinate system is as follows:

$$\frac{p_\infty - p}{\rho_\infty} = \frac{\partial \phi}{\partial t} + \frac{1}{2}\left[\left(\frac{\partial \phi}{\partial \xi^{fa}}\right)^2 + \left(\frac{\partial \phi}{\partial \eta^{fa}}\right)^2\right] - \left(v_{\xi^{fa}}^{rigid}\frac{\partial \phi}{\partial \xi^{fa}} + v_{\eta^{fa}}^{rigid}\frac{\partial \phi}{\partial \eta^{fa}}\right) \tag{3.48}$$

where $v_{\xi^{fa}}^{rigid}$ and $v_{\eta^{fa}}^{rigid}$ are the velocities of the airfoil resolved in the $\xi^{fa}-\eta^{fa}$ coordinate system. It is important to note that the velocity potential is discontinuous across shear layers, i.e. the wakes shed from the airfoil. Therefore, the potential is computed along piecewise continuous contours [96]. Vorticity and circulation are defined as positive when counter-clockwise; therefore, integration along the contours is performed in a counter-clockwise manner. The origin of integration is selected to be a point close to the trailing edge on the upper surface of the airfoil as shown in Figure 3.14. Furthermore, s_{wk1} and s_{wk2} denote the arc coordinates at which the shear layers are formed as indicated in Figure 3.14. Therefore, ϕ is discontinuous at s_{wk1} and s_{wk2}. For an airfoil with a sharp trailing edge, a shear layer emanates from the trailing edge; therefore, $s_{wk1} = L_C$. The total velocity potential at any point in the airfoil wake system is given by

$$\phi(s,t) = \phi_b(s,t) + \phi_{wk1}(s,t) \tag{3.49}$$

For attached flow, ϕ_b is obtained by integrating the vorticity along contour C_1 [97] shown in Figure 3.14. For separated flow, ϕ_b is obtained by integrating the vorticity along contours $C_1 - C_2 - C_3$ [96] as follows:

For $0 < s < s_{wk2}$

$$\phi_b(s,t) = \phi_0 + \int_0^s \gamma_b \, ds \tag{3.50}$$

For $s_{wk2} < s < L_C$

$$\phi_b(s,t) = \phi_0 + \int_0^{s_{wk2}-} \gamma_b \, ds + \int_{L_{wk2}} \left\{\gamma_{wk2}(\varsigma,t)\left(1 - e^{-\frac{r_v^2}{4\nu_\infty t_v}}\right)\right\} \mathrm{d}\varsigma + \int_{s_{wk2}+}^{s} \gamma_b \, ds \tag{3.51}$$

The velocity potential due to shear layer 1 is given by

$$\phi_{wk1}(s,t) = \int_{L_{wk1}} \left\{ \frac{\gamma_{wk1}(\varsigma,t)}{2\pi} \varphi(\varsigma,s,t) \left(1 - e^{-\frac{r_v^2}{4\nu_\infty t_v}} \right) \right\} \mathrm{d}\varsigma \tag{3.52}$$

where, in Eqs. (3.51) and (3.52), the effect of viscosity is included inside the integrals on the RHS and

$$r_v = \left| \boldsymbol{\zeta}_{wk}^{fa}(\varsigma,t) - \boldsymbol{\zeta}^{fa}(s) \right| \tag{3.53}$$

Moreover $\varphi \in [0, 2\pi)$, depicted in Figure 3.12, is given by

$$\varphi(\varsigma,s,t) = \text{argument}\left(\boldsymbol{\zeta}_{wk}^{fa}(\varsigma,t) - \boldsymbol{\zeta}^{fa}(s) \right) \tag{3.54}$$

Equivalence of the Approaches

The vortex impulse method and the unsteady Bernoulli equation are mathematically equivalent; however, the integrated aerodynamic forces computed using these approaches are not identical for a rigid zero thickness airfoil.

The aerodynamic force acting on an airfoil, obtained by integrating the pressure computed using the Bernoulli equation, is as follows:

$$\begin{aligned} \boldsymbol{F} &= \oiint_S p\hat{\boldsymbol{n}}\, dS \\ &= \iint_{S_\xi} p\hat{\boldsymbol{n}}_\xi\, dS_\xi + \iint_{S_\eta} p\hat{\boldsymbol{n}}_\eta\, dS_\eta \\ &= \boldsymbol{F}_\xi + \boldsymbol{F}_\eta \end{aligned} \tag{3.55}$$

For a zero thickness flat plate airfoil, the projected area parallel to the chord, i.e. S_ξ, is equal to zero. Consequently, $\boldsymbol{F}_\xi \equiv 0$. Therefore, for this case the force calculated by integrating pressure is always normal to the airfoil chord.

On the other hand, the calculation of force from the impulse and the moment of

impulse of vorticity, shown in Eqs. (3.46) and (3.47), does not require the projected areas of the airfoil. Therefore, the forces computed using Eq (3.47) may have a non zero component parallel the airfoil chord. Therefore, for a zero thickness flat plate airfoil, the vortex impulse method and the Bernoulli equation yield identical values of force normal to the airfoil chord, but do not produce identical results for force parallel to the airfoil chord.

3.4 Limitations of the modified aerodynamic model

Several modifications to enhance the capabilities of the aerodynamic model have been introduced. However, underlying assumptions and limitations need to be noted.

1. The effect of viscosity is incorporated as the decay of circulation once a vortex is shed into the wake. However, the aerodynamic formulation is fundamentally based on the assumption of potential flow and the effect of boundary layer around the airfoil is neglected.

2. The aerodynamic formulation is 2D and is applied on the wing in a strip-theory manner. Effects of spanwise flow, tip vortices, and aerodynamic interactions between the various wing sections are neglected.

3. Wing flexibility is incorporated in an averaged manner. Spanwise flexibility is incorporated by using a time dependent radius of the airfoil-wake surface. Chordwise flexibility is incorporated using a zero lift angle due to camber and the averaged effect of airfoil velocities in the calculation of the quasi-steady vorticity. The assumptions imposed during incorporation of chordwise velocities have to be re-examined if the contribution of airfoil flexibility to the unsteady loads is expected to be comparable to the contribution of LEVs and wake capture.

4. The physics of flow separation, including intermittent separation and reattachment, are not accounted for. The onset of flow separation and the separation

point are assumed in an ad hoc manner. The flow is assumed to be either attached or separated.

5. The geometry of the shed wake, in hover as well as forward flight, is approximated using a cylindrical surface that is normal to the stroke plane. For the general case, the wake is typically not confined to a normal cylinder and a more realistic representation that accounts for wake contraction, movement of vorticity out of the NC, and other 3D effects, has to be considered.

CHAPTER IV

Aeroelastic Analysis

The aeroelastic behavior of the flapping wing is modeled in MARC by coupling the structural dynamic model with the loads computed using the approximate aerodynamic model. The aeroelastic response is obtained using an updated Lagrangian (UL) approach and the coupled fluid-structure model is implemented in MARC using user defined subroutines.

4.1 The Updated Lagrangian Approach

The equations of motion representing the aeroelastic response problem are obtained using an updated Lagrangian (UL) approach [88, 98]. In this approach, an approximate solution is obtained by referring all the quantities (stress, strain and displacements) of the deformed configuration to the equilibrium configuration obtained at the previous time step, and linearizing the resulting equations of motion (EOM). Implementation of the UL formulation in MARC, which is based on the description given in Refs. [88, 98], is shown in Figure 4.1 (left) and summarized below.

Starting from the equilibrium equations, the principle of virtual work yields the

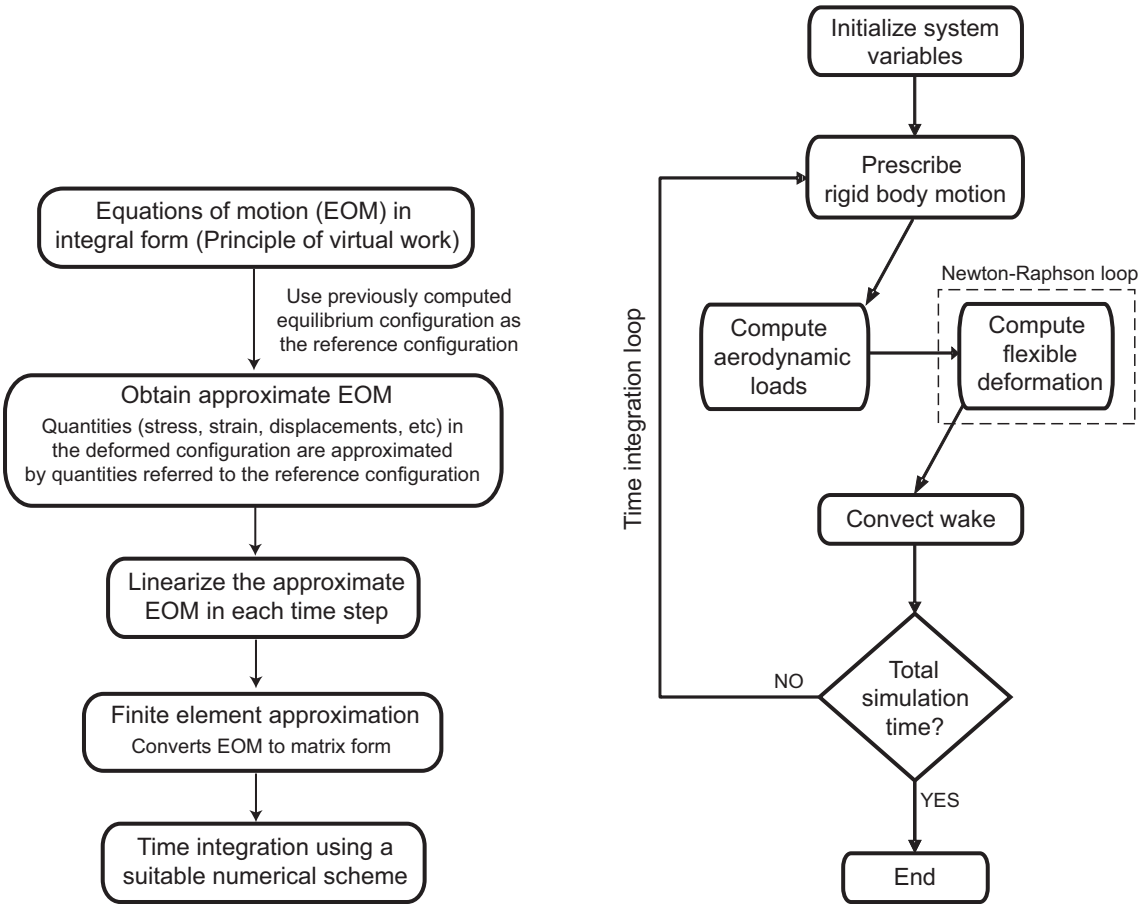

Figure 4.1: Formulation of the aeroelastic equations (left) and implementation of the aeroelastic model in MARC (right).

following integral form [88, 98]:

$$\int_{V^{t+\Delta t}} \sigma_{ij}^{t+\Delta t} \delta e_{ij}^{t+\Delta t} dV^{t+\Delta t} = \tilde{R}^{t+\Delta t} - F_{inertial}^{t+\Delta t} \tag{4.1}$$

where

$$\tilde{R}^{t+\Delta t} = \int_{A^{t+\Delta t}} T_k^{t+\Delta t} \delta u_k^{t+\Delta t} dA^{t+\Delta t} + \int_{V^{t+\Delta t}} \rho^{t+\Delta t} f_k^{t+\Delta t} \delta u_k^{t+\Delta t} dV^{t+\Delta t} \tag{4.2}$$

and

$$F_{inertial}^{t+\Delta t} = \int_{V^{t+\Delta t}} \rho^{t+\Delta t} \ {}^{(t+\Delta t)}\ddot{u}_k^{t+\Delta t} \ \delta u_k^{t+\Delta t} \ dV^{t+\Delta t} \tag{4.3}$$

where, the right superscript on the quantities indicates that the deformed configuration, i.e. the configuration at time $t+\Delta t$, is the reference configuration; ${}^{(t+\Delta t)}u_k$, ${}^{(t+\Delta t)}\ddot{u}_k$, and u_k are the Cartesian components of the accelerations and incremental displacements, and $u_k = {}^{(t+\Delta t)}u_k - {}^{t}u_k$. The left superscript indicates the total quantity at time $(t+\Delta t)$.

The deformed configuration is unknown; thus, quantities that are referred to the deformed configuration, such as $\sigma_{ij}^{t+\Delta t}$ and $e_{ij}^{t+\Delta t}$, cannot be computed exactly. Therefore, the LHS of Eq. (4.1) is approximated by an integral that uses the configuration at time t as the reference. In this approximation, $\sigma_{ij}^{t+\Delta t}$ is approximated by $S_{ij}^{t+\Delta t}$ and $e_{ij}^{t+\Delta t}$ is approximated by $\varepsilon_{ij}^{t+\Delta t}$. Therefore, Eq. (4.1) modifies to the following equation:

$$\int_{V^t} S_{ij}^{t+\Delta t}\delta\varepsilon_{ij}^{t+\Delta t} dV^t = \tilde{R}^{t+\Delta t} - F_{inertial}^{t+\Delta t} \tag{4.4}$$

Furthermore, the second Piola-Kirchoff (PK2) stress at time $t+\Delta t$ is obtained as a sum of the Cauchy stress in the reference configuration, σ_{ij}^t, and an incremental PK2 stress, $\Delta_t S_{ij}$:

$$S_{ij}^{t+\Delta t} = \sigma_{ij}^t + \Delta_t S_{ij} \tag{4.5}$$

Similarly, the Green-Lagrange strain is given by

$$\varepsilon_{ij}^{t+\Delta t} = \varepsilon_{ij}^t = e_{ij}^t + \eta_{ij}^t \tag{4.6}$$

where e_{ij}^t and η_{ij}^t are obtained from the incremental displacement as

$$\begin{aligned} e_{ij}^t &= \frac{1}{2}(u_{i,j}^t + u_{j,i}^t) \\ \eta_{ij}^t &= \frac{1}{2}u_{k,i}^t u_{k,j}^t \end{aligned} \tag{4.7}$$

Furthermore, the constitutive relations are given by

$$\Delta_t S_{ij} = C^t_{ijrs} \varepsilon^t_{rs} \tag{4.8}$$

where C^t_{ijrs} denotes the components of the tangent stiffness matrix. The final equation, obtained by substituting Eqs. (4.5), (4.6), and (4.8) into Eq. (4.4), is nonlinear in the incremental displacement u_i and is given by

$$\int_{V^t} C^t_{ijrs} \varepsilon^t_{rs} \delta \varepsilon^t_{ij} dV^t + \int_{V^t} \sigma^t_{ij} \delta \eta^t_{ij} dV^t = \tilde{R}^{t+\Delta t} - F^{t+\Delta t}_{inertial} - \int_{V^t} \sigma^t_{ij} \delta e^t_{ij} dV^t \tag{4.9}$$

Equation (4.9) is linearized by assuming that $\delta \varepsilon^t_{ij} = \delta e^t_{ij}$, so that the constitutive equation becomes $\Delta_t S_{ij} = C^t_{ijrs} e^t_{rs}$. Thus, the linearized integral equation that represents dynamics of the system is given by

$$\int_{V^t} C^t_{ijrs} e^t_{rs} \delta e^t_{ij} dV^t + \int_{V^t} \sigma^t_{ij} \delta \eta^t_{ij} dV^t = \tilde{R}^{t+\Delta t} - F^{t+\Delta t}_{inertial} - \int_{V^t} \sigma^t_{ij} \delta e^t_{ij} dV^t \tag{4.10}$$

The finite element approximation to the accelerations and incremental displacements are given by

$$^{t+\Delta t}\ddot{\mathbf{u}}^{t+\Delta t}(\boldsymbol{x}, t) = {}^{t+\Delta t}\underline{\ddot{\mathbf{u}}}^{t+\Delta t} \cdot \mathbf{N} \qquad \text{and} \qquad \mathbf{u}(\boldsymbol{x}, t) = \underline{\mathbf{u}} \cdot \mathbf{N} \tag{4.11}$$

Substituting Eqs. (4.11), (4.7), and (4.3), into Eq. (4.10), and simplifying the result yields the final form of the equation of motion for each element in the structure as:

$$(\mathbf{K}^t_L + \mathbf{K}^t_{NL})\underline{\mathbf{u}} = \tilde{\mathbf{R}}^{t+\Delta t} - \mathbf{M}\, {}^{t+\Delta t}\underline{\ddot{\mathbf{u}}}^{t+\Delta t} - \mathbf{F}^t_\sigma \tag{4.12}$$

Expressions for $\mathbf{K}_L^t$, $\mathbf{K}_{NL}^t$, $\mathbf{F}_\sigma^t$, and $\mathbf{M}$ are given below:

$$\mathbf{K}_L^t = \int_{V^t} (\mathbf{B}_L^t)^T \mathbf{C}^t \mathbf{B}_L^t \mathrm{d}V^t \tag{4.13}$$

$$\mathbf{K}_{NL}^t = \int_{V^t} (\mathbf{B}_{NL}^t)^T \sigma^t \mathbf{B}_{NL}^t \mathrm{d}V^t \tag{4.14}$$

$$\mathbf{F}_\sigma^t = \int_{V^t} (\mathbf{B}_L^t)^T \sigma^t \, \mathrm{d}V^t \tag{4.15}$$

$$\mathbf{M} = \int_{V^t} \mathbf{N}^T \rho^t \mathbf{N} \mathrm{d}V^t \tag{4.16}$$

where $\mathbf{B}_L^t$ and $\mathbf{B}_{NL}^t$ are transformation matrices obtained from the shape function matrices. The derivation of $\mathbf{B}_L^t$ and $\mathbf{B}_{NL}^t$ for various types of elements (beams, shells, etc) is described in Refs. [89, 98]. Finally, Eq. (4.12), that represents the finite element discretization of the equation of motion, is integrated forward in time using an appropriate numerical scheme.

In this approach, the true stress and strain in the deformed configuration at the beginning of each time step are approximated using incremental stress and strain measures in the reference configuration. Therefore, iterations are often required within each time step so that the approximate incremental quantities converge. The iterations are done using the Newton-Raphson (NR) method [88, 89] as follows. The residual force vector is defined as:

$${}_G^t\mathbf{E}_{elas} = {}_G\tilde{\mathbf{R}}^{t+\Delta t} - ({}_\mathbf{G}\mathbf{K}_\mathbf{L}^\mathbf{t} + {}_\mathbf{G}\mathbf{K}_\mathbf{NL}^\mathbf{t})\, {}_G\underline{\mathbf{u}} - {}_\mathbf{G}\mathbf{M}\ {}_G^{t+\Delta t}\underline{\ddot{\mathbf{u}}}^{t+\Delta t} - {}_G\mathbf{F}_\sigma^t \tag{4.17}$$

where the left subscript G implies that the matrices and vectors represent the global assembled matrices of the structure. The residual force vector for the structure

including kinematic constraints is given by

$$ {}^{t}_{G}\mathbf{E}_{res} = \begin{Bmatrix} {}^{t}_{G}\mathbf{E}_{elas} + \boldsymbol{E}^{\boldsymbol{u}}_{con} \\ \boldsymbol{E}^{\boldsymbol{\lambda}}_{con} \end{Bmatrix} \tag{4.18} $$

where, $\boldsymbol{E}^{\boldsymbol{u}}_{con}$ and $\boldsymbol{E}^{\boldsymbol{\lambda}}_{con}$ are due to the constraints and given in Eq. (2.15). The converged values of the incremental stresses, strains, and displacements, for time $t + \Delta t$ are obtained by minimizing ${}^{t+\Delta t}_{G}\mathbf{E}_{res}$. Following a first order Taylor expansion,

$$ {}^{t+\Delta t}_{G}\mathbf{E}_{res} = {}^{t}\mathbf{E}_{res} + {}^{t}_{G}\mathbf{K} \begin{Bmatrix} \Delta \underline{\mathbf{u}} \\ \Delta \boldsymbol{\lambda} \end{Bmatrix} \tag{4.19} $$

where, the tangent stiffness matrix is given by

$$ {}^{t}_{G}\mathbf{K} = \begin{bmatrix} {}^{t}\mathbf{K}_{elas} + \boldsymbol{K}_{11} & \boldsymbol{K}_{12} \\ \boldsymbol{K}_{21} & \boldsymbol{K}_{22} \end{bmatrix} \qquad \text{where} \qquad {}^{t}\mathbf{K}_{elas} = -\frac{\partial {}^{t}\mathbf{E}_{elas}}{\partial {}^{t}_{G}\underline{\mathbf{u}}} \tag{4.20} $$

and $\boldsymbol{K}_{11}, \boldsymbol{K}_{12}, \boldsymbol{K}_{21}$ and $\boldsymbol{K}_{22}$ are given in Eq. (2.18). The converged values of incremental displacements, stresses, and strains are obtained by iterating the following expressions:

$$ {}^{t+\Delta t}_{G}\mathbf{K}^{(i-1)} \begin{Bmatrix} \Delta \underline{\mathbf{u}}^{(i)} \\ \Delta \boldsymbol{\lambda}^{(i)} \end{Bmatrix} = {}^{t+\Delta t}_{G}\mathbf{E}^{(i-1)}_{res} \tag{4.21} $$

and

$$ \begin{Bmatrix} {}^{t+\Delta t}_{G}\underline{\mathbf{u}}^{(i)} \\ \boldsymbol{\lambda}^{(i)} \end{Bmatrix} = \begin{Bmatrix} {}^{t+\Delta t}_{G}\underline{\mathbf{u}}^{(i-1)} \\ \boldsymbol{\lambda}^{(i-1)} \end{Bmatrix} + \begin{Bmatrix} \Delta \underline{\mathbf{u}}^{(i)} \\ \Delta \boldsymbol{\lambda}^{(i)} \end{Bmatrix} $$

where $\quad i = 1, 2, \ldots$ denotes the iteration number

with the following initial conditions

$$\begin{Bmatrix} {}^{t+\Delta t}_{G}\underline{\mathbf{u}}^{(0)} \\ \boldsymbol{\lambda}^{(0)} \end{Bmatrix} = \begin{Bmatrix} {}^{t}_{G}\underline{\mathbf{u}} \\ \boldsymbol{\lambda}_0 \end{Bmatrix} \quad ; \qquad {}^{t+\Delta t}_{G}\mathbf{K}^{(0)} = {}^{t}_{G}\mathbf{K} \quad ; \qquad {}^{t+\Delta t}_{G}\mathbf{E}^{(0)}_{res} = {}^{t}_{G}\mathbf{E}_{res} \tag{4.22}$$

where the left and right superscripts indicate the time step and the iteration respectively, and $\boldsymbol{\lambda}_0$ is an initial guess for the Lagrange multipliers. A converged solution is obtained when an appropriate convergence criteria either on ${}^{t+\Delta t}_{G}\mathbf{E}^{(i)}_{res}$ or ${}^{t+\Delta t}_{G}\underline{\mathbf{u}}^{(i)}$ is satisfied. Two implementations of the NR method are available in MARC [83]: (1) the complete Newton-Raphson method, wherein the tangent stiffness matrix is computed for each iteration in a time step, and (2) a modified Newton-Raphson method in which the tangent stiffness matrix is computed only once at the start of the iteration. The complete Newton-Raphson method [83, 88, 89] is used in this dissertation.

Numerical Integration

The equations of motion obtained from the UL method are integrated using a single step Houbolt (SSH) scheme. The implementation of this scheme in MARC is based on the description given in Ref. [99]. The SSH scheme, which belongs to the class of Houbolt algorithms [88, 99], is an implicit and second order accurate scheme that is unconditionally stable for linear systems. By design, the algorithm incorporates numerical damping and is *asymptotically annihilating*, which implies that the high frequency response of the system is eliminated in each time step.

4.2 Fluid-structure Coupling in MARC

The implementation of the aeroelastic model is shown in the block diagram given in Figure 4.1 (right). At each time step, rigid body motion is prescribed as displacements or rotations at specified nodes. The aerodynamic loads, computed based on the wing

motion at the beginning of each time step, are applied to the structure via FORCEM user defined subroutine in MARC. This subroutine is called from the main program for each step of the Newton-Raphson iteration within a time step to ensure convergence of the structural displacements for the applied loads. Finally, the vortices shed into the wake are convected at the end of the time step.

CHAPTER V

Structural Dynamic Model: Validation and Comparisons

Validation of the capabilities of MARC and determining its suitability for modeling flexible flapping wings has been carefully done in this study. The results presented include: (1) implementation of large rigid body motions representative of wing kinematics, (2) calculations that show that the centrifugal stiffening effect is properly taken into account, (3) comparison of mode shapes and frequencies of anisotropic wings, and (4) comparison of tip displacements of anisotropic wings flapping in vacuum.

5.1 Implementation of Wing Kinematics

Implementation of large amplitude, time dependent rotations in MARC were examined by imposing 2D and 3D rotations on a rigid rectangular plate. The rigid plate, shown in Figure 5.1, has dimensions $R_{span} = 0.1$ m and $b = 0.025$ m, and is modeled using multi-point rigid body constraint type RBE2 available in MARC/NASTRAN [87]. This constraint allows the user to define a single "master" node and several "slave" nodes such that the motion of the slave nodes is linked to the motion of the master node using a rigid body link. In the plate configuration shown in Figure 5.1, the hinge

point H was chosen as the master node and all other nodes were slave nodes. Using this feature, rotations were prescribed at the master node.

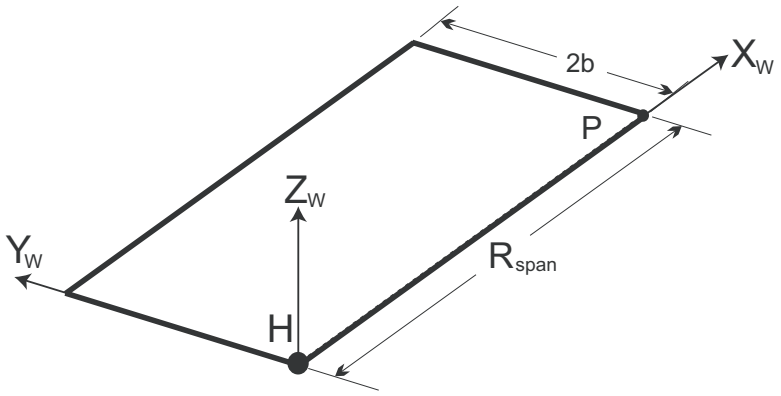

Figure 5.1: Rectangular plates.

Implementation of 2D Rotations

The results shown in Figure 5.2(a), which correspond to the implementation of 2D rotations in MARC, pertain to the motion of point P (indicated in Figure 5.1) as measured in the unrotated coordinate system. Rotations described by Eq (5.1) was used as input:

$$\boldsymbol{\psi} = \sin(2\pi f t) \begin{Bmatrix} 1 \\ 1 \\ 1 \end{Bmatrix} \tag{5.1}$$

where the angle is measured in radians, $f = 20$ Hz, and $\Delta t = 5 \times 10^{-4}$ seconds. The x, y, and z coordinates of P as functions of time are obtained from MARC and compared to the motion of P that was computed by substituting Eq. (2.4) into Eq. (2.2) and calculating the result in a simple MATLAB program. This comparison indicates that the large amplitude 2D rotations can be implemented accurately in MARC using an incremental form of the rotation vector.

Implementation of 3D Rotations using Incremental Rotation Vector

Euler angles given in Refs. [18, 44], represented as rotation vectors in Eq (5.2), are input as a time dependent rotation to the rigid plate.

$$\begin{aligned}
\boldsymbol{\psi}_1 &= 53^\circ \begin{Bmatrix} 1 \\ 0 \\ 0 \end{Bmatrix} \\
\boldsymbol{\psi}_2 &= \left[-3^\circ - 43^\circ \cos(2\pi f t)\right] \begin{Bmatrix} 0 \\ 1 \\ 0 \end{Bmatrix} \\
\boldsymbol{\psi}_3 &= \left[8^\circ - 77^\circ \cos(2\pi f t - 49^\circ) - 3^\circ \cos(2\pi f t + 67^\circ) - 8^\circ \cos(2\pi f t + 29^\circ)\right] \begin{Bmatrix} 1 \\ 0 \\ 0 \end{Bmatrix}
\end{aligned} \tag{5.2}$$

where, $f = 20$ Hz. Note that the Euler angles shown in Eq. (5.2) correspond to a large rotation at $t = 0$. In Ref. [44], this initial static rotation was required since the flapping motion was prescribed with respect to a body-fixed frame that did not initially coincide with the wing-fixed frame. One of the objectives of this study is to examine the implementation of large amplitude flapping motion. Therefore, it was assumed that the initial offset between the body-fixed and wing-fixed frames is zero. This requires elimination of the initial static rotation, and is accomplished by obtaining the Euler angles corresponding to the initial rotation, denoted by $\boldsymbol{\psi}_1^0$, $\boldsymbol{\psi}_2^0$, and $\boldsymbol{\psi}_3^0$, by substituting $t = 0$ into Eq. (5.2):

$$\boldsymbol{\psi}_1^0 = 53^\circ \begin{Bmatrix} 1 \\ 0 \\ 0 \end{Bmatrix} \qquad \boldsymbol{\psi}_2^0 = -46^\circ \begin{Bmatrix} 0 \\ 1 \\ 0 \end{Bmatrix} \qquad \boldsymbol{\psi}_3^0 = -50.7^\circ \begin{Bmatrix} 1 \\ 0 \\ 0 \end{Bmatrix} \tag{5.3}$$

Then, the modified rotation matrix, denoted by $\hat{\boldsymbol{R}}_1$, that describes the flapping motion without the initial rotation is given by

$$\hat{\boldsymbol{R}}_1 = \hat{\boldsymbol{R}}^T_{(\boldsymbol{\psi}_1^0, \boldsymbol{\psi}_2^0, \boldsymbol{\psi}_3^0)} \quad \hat{\boldsymbol{R}}_{(\boldsymbol{\psi}_1, \boldsymbol{\psi}_2, \boldsymbol{\psi}_3)} \tag{5.4}$$

where $\hat{\boldsymbol{R}}_{(\boldsymbol{\psi}_1^0, \boldsymbol{\psi}_2^0, \boldsymbol{\psi}_3^0)}$ and $\hat{\boldsymbol{R}}_{(\boldsymbol{\psi}_1, \boldsymbol{\psi}_2, \boldsymbol{\psi}_3)}$ are obtained using Eq. (2.7). For each time step, the modified rotation tensor $\boldsymbol{R}_1$ is used to compute the rotation vector implemented in MARC. The time step used to discretized the motion was 5×10^{-4} seconds. Figure 5.2(b) shows a comparison of the position of the point P that has coordinates (0.1,0,0) in (X_W, Y_W, Z_W) obtained as output from MARC with that computed using a MATLAB program. It is evident that the implementation of rotations in Marc shows considerable error. Decreasing the time step to 2.5×10^{-4} seconds did not improve the results. This result indicates that wing kinematics, which are typically 3D rotations, cannot be implemented as a time dependent rotation vector in MARC. Therefore, an alternate implementation of wing kinematics is considered.

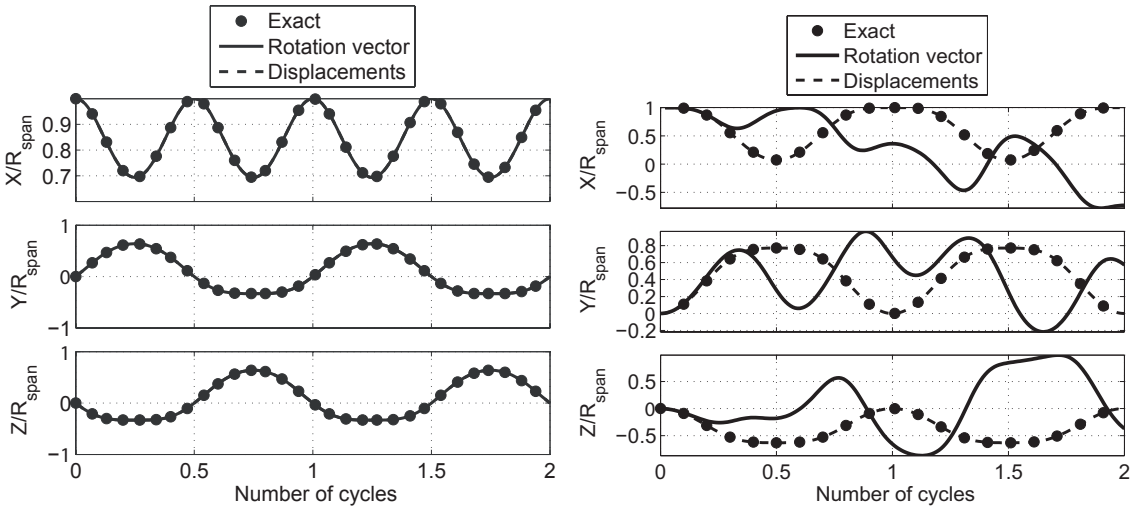

(a) 2D rotations in MARC

(b) 3D rotations in MARC

Figure 5.2: Implementation of rigid body rotations in MARC.

Implementation of Wing Kinematics as Displacements

Wing kinematics are implemented as displacements at three nodes. The RBE2 constraint was used to constrain the rotational DOF of the nodes; the displacement DOF were not constrained so that displacement boundary conditions could be prescribed at multiple nodes. Material properties were selected so as to minimize the deformation due to wing flexibility. The plate was modeled using 440 shell elements (Element type 75) and assumed to have the following properties: $t_h = 5$mm, $E = 2100$GPa, $\rho = 20$ kg/m^3, and $\nu = 0.3$. Displacements, which correspond to the rotation tensors that describe the 2D and 3D rotations, are computed for three vertices of the rectangular plate and imposed at the nodes at these locations. The displacements of the fourth vertex were obtained as output from MARC and compared to the exact solution, which is obtained from a MATLAB implementation, in order to examine if the kinematics are implemented correctly. For the test cases, displacements corresponding to the flapping motion were prescribed at three points: the hinge H is held fixed in translation but unconstrained in rotation; displacements are prescribed at points that have coordinates (0.1,0.05,0) and (0,0.05,0) respectively in (X_W, Y_W, Z_W). Subsequently, displacements are obtained at point P that has coordinates (0.1,0,0) in (X_W, Y_W, Z_W). Figures 5.2(a) and 5.2(b) show a comparison of the coordinates of point P obtained as output from MARC to the exact solution. It is evident that the displacements output from MARC are identical to the exact solution. This indicates that large amplitude 2D and 3D rotations are correctly implemented in MARC as displacements.

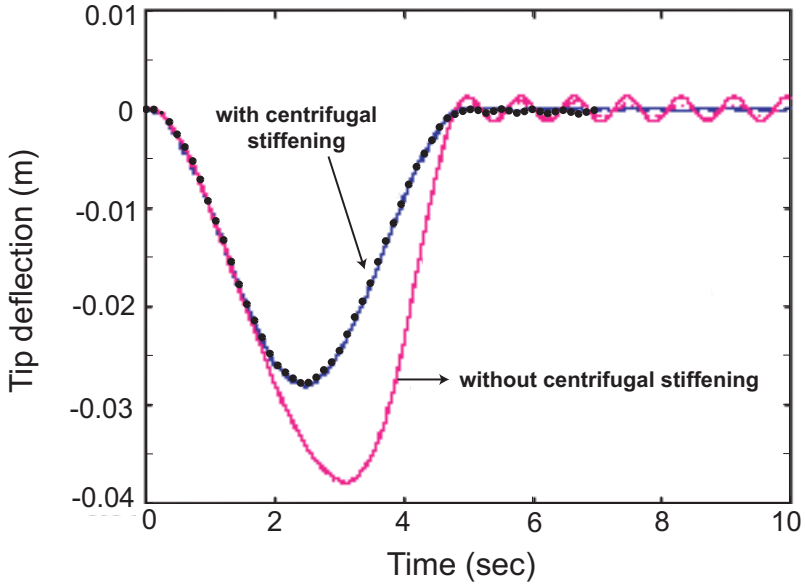

Figure 5.3: Comparison of tip displacements for an accelerating plate. Results 1 and 2 (solid lines) from Ref. [70]; result 3, circles, MARC current study .

5.2 Centrifugal Stiffening Effect

The effect of centrifugal stiffening was examined by considering the case of an isotropic plate undergoing a prescribed angular acceleration that is given by Eq. (5.5).

$$\omega = \begin{cases} \omega_s \left(\frac{t}{t_s} - \frac{1}{2\pi} \sin \frac{2\pi t}{t_s} \right) & 0 \le t \le t_s \\ \omega_s & t \ge t_s \end{cases} \tag{5.5}$$

where, $\omega_s = 10$ rad/s and $t_s = 5$ s. The properties of the plate are provided in Table 5.1. The plate was modeled in MARC using 900 shell elements (Type 75) and the results were obtained for a time step $\Delta t = 0.001$ second. A comparison of tip displacements, obtained from MARC and Ref. [70], are shown in Figure 5.3. The results indicate that the structural model in MARC incorporates the effect of centrifugal stiffening correctly.

Property	E	ρ	ν	R_{span}	b	t_h
Value	70 GPa	3000 kg/m^3	0.3	1.0 m	0.5 m	0.0025 m

Table 5.1: Geometric and material properties of the accelerating isotropic plate.

5.3 Comparison of Mode Shapes and Frequencies for Anisotropic Wings

The computed and experimentally determined [69] mode shapes and frequencies for anisotropic Zimmerman wings are compared so as to validate the structural dynamic models. The anisotropic wings, shown in Figure 5.5, are built from an unstressed CAPRAN film (membrane) supported by a carbon fiber based spar-batten skeleton. Using the notation used in Ref [69], the wings are labeled as LiBj where i and j denote the number of prepreg layers used in the construction of the LE spar and the battens, shown in Figure 5.4. The nominal elastic properties of the materials used were provided by the respective manufacturers.

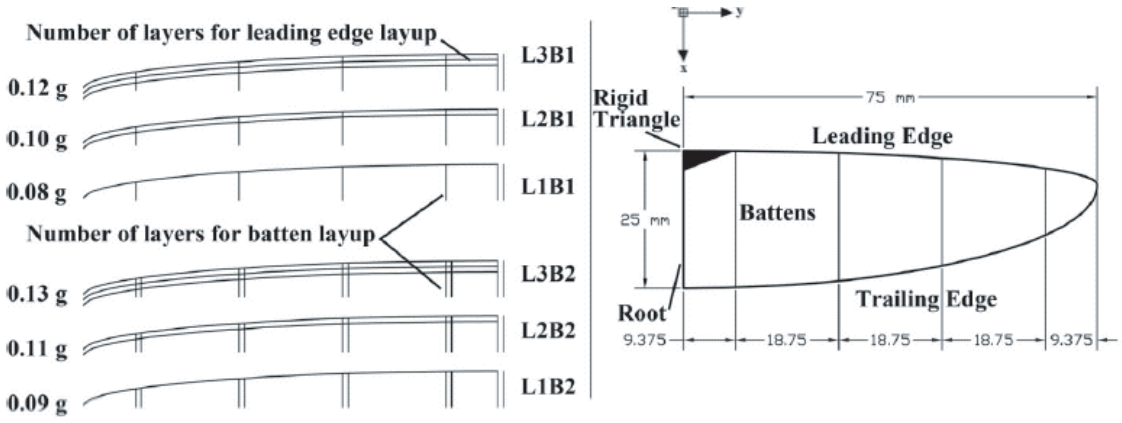

Figure 5.4: Anisotropic wing configurations, from Ref [69].

The natural frequencies of the wings were identified using a Laser Doppler Vibrometer (LDV) that uses the phase shift between the incident and reflected light to obtain a frequency response spectrum of the structure [69]. The experiments involve visual tracking of the wing surface using high speed cameras to obtain the deformation

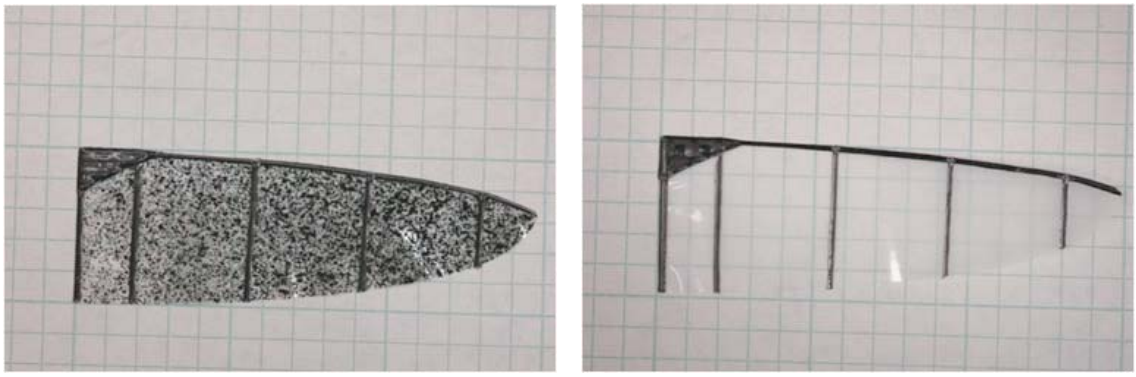

Figure 5.5: Painted (left) and unpainted wings (right).

pattern. The translucent CAPRAN film, shown in Figure 5.5 (right), is not suitable for visual tracking. Therefore, a dense speckle pattern was generated by spraying black acrylic paint, shown in Figure 5.5 (left), to facilitate tracking of the wing. The CAPRAN film is very thin, lightweight, and flexible, and the change in geometric and material properties of the film due to the paint speckle that is deposited on the film were determined experimentally, and the properties were used to generate the structural dynamic and aeroelastic results.

5.3.1 Tensile Tests on the CAPRAN Membrane

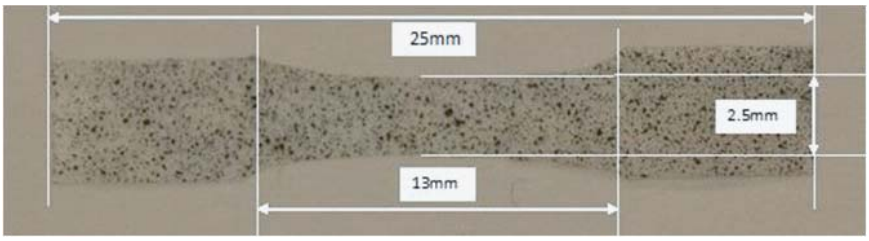

Figure 5.6: Tensile test specimens.

The Young's moduli of the films were measured by tensile tests using specimens shown in Figure 5.6. Tensile test samples are manufactured to a total length of 25 ± 1 mm, a gauge length of 13 ± 2 mm and a height of 2.5 ± 0.5 mm. The tests

were carried out under displacement control loading at a nominal rate of 0.018 mm/s. The small scale tensile tester is shown in Figure 5.7. Strains are determined using optical images taken with a high resolution camera of a speckle pattern, distributed on the surface of the film using acrylic paint applied with an airbrush or a spray can. Unpainted films could not be tracked; therefore, a light speckle pattern, expected to have an insignificant effect on the material properties of the film, was deposited on the unpainted films. Specimens of the densely and lightly painted films, labeled as Heavy dots and Light dots are shown in Figure 5.8. Thicknesses of the samples are measured with a Phillips XL30 Environmental Scanning Electron Microscope (SEM).

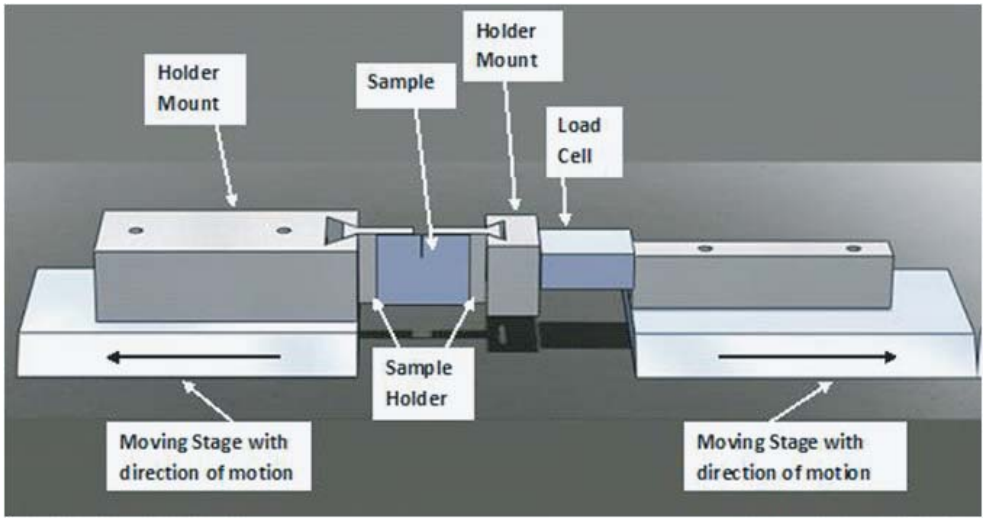

Figure 5.7: Experimental setup.

The SEM measurements indicated that there was little or no change in thickness of the film due to the paint; an average value of 15 microns is therefore used in calculations. The thicknesses are listed in Table 5.2. The characteristic stress-strain curves obtained after the post-processing of the data are shown in Figures 5.10(a) and 5.10(b). The results indicate that the elastic moduli of the painted (heavy dots) and lightly painted (light dots) films are approximately the same, where an averaged value of E = 2.74 GPa is used in calculations. However, static weight measurements show that the paint increases the weight, and the density, of the films by approximately

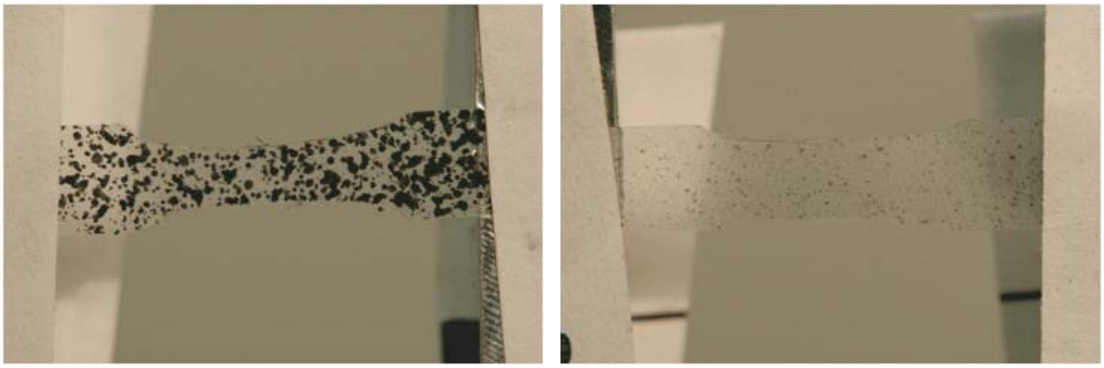

Figure 5.8: Specimens of the film. Dense speckle (heavy dots) - left and light speckle (light dots) - right.

	Unpainted Film	Painted film
Density, kg/m^3	1186.0	1383.7
Young's modulus, GPa	2.72 ± 0.16	2.76 ± 0.21
Thickness, ($\times 10^{-6}$ m)	15.17 ± 0.90	14.96 ± 0.57

Table 5.2: Density and Young's moduli of the painted and unpainted films.

16%. The densities and Young's moduli of the painted and unpainted films are given in Table 5.2.

5.3.2 Comparison of Mode Shapes and Frequencies

The experimentally determined and computed mode shapes and frequencies for anisotropic Zimmerman wings are shown in Figure 5.11 and Tables 5.5 and 5.6 respectively. The finite element models of the wings, shown in Figure 3.2, are obtained using 1263 thick shell elements (Element type 75 in MARC).

Note that the experiments [69] were conducted in air; this implies that the mode shapes and frequencies that are identified correspond to aeroelastic modes that include added mass effects [56] as well as coupling effects between bending and torsion. In an aeroelastic system, a useful indicator of the relative importance of the inertial to

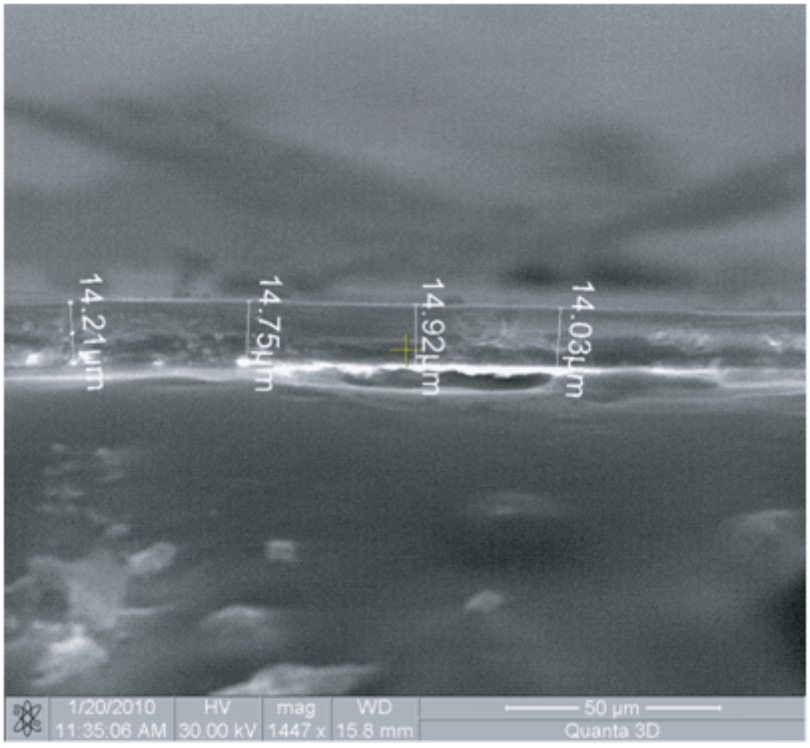

Figure 5.9: Sample image from the SEM indicating thickness of the film.

aerodynamic forces is the mass ratio [56] that is described by Eq (5.6).

$$\text{Mass ratio} = \frac{\rho t_h c_r}{0.25\pi\rho_\infty c_r^2} \tag{5.6}$$

where, the thickness of the composite and the membrane are given in Table 5.4. A lower bound of the mass ratio for the anisotropic wings is obtained by considering a representative cross section that is composed entirely of the membrane material, illustrated in Figure 5.12 (left). The mass ratio can also be computed by considering a more realistic cross section as shown in Figure 5.12 (right).

The values of the mass ratios are given in Table 5.3. The calculations indicate that the added mass effects are most likely to be significant for modes that have a predominant contribution from the membrane, and these will be relatively insignificant for modes that have a predominant contribution from the composite skeleton.

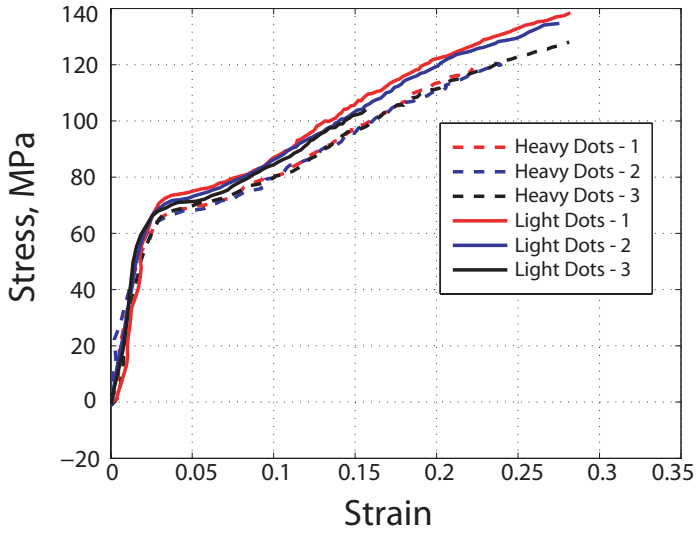

(a) Experimental stress-strain curves

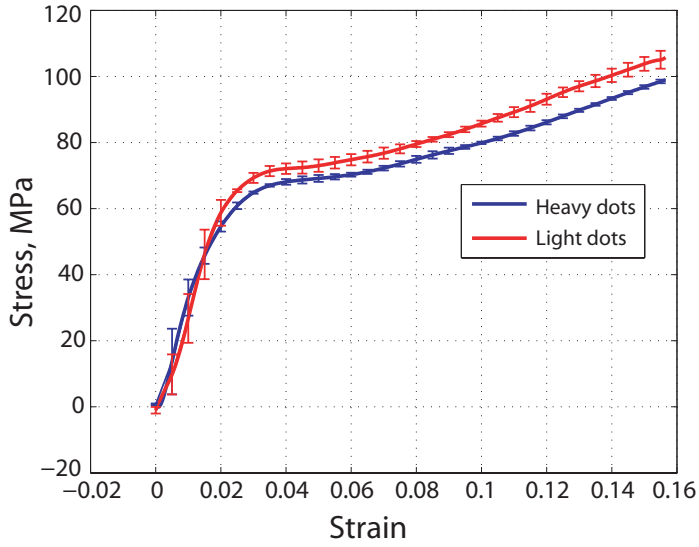

(b) Mean stress-strain curves

Figure 5.10: Stress-strain curves for the painted (heavy dots) and unpainted (light dots) films.

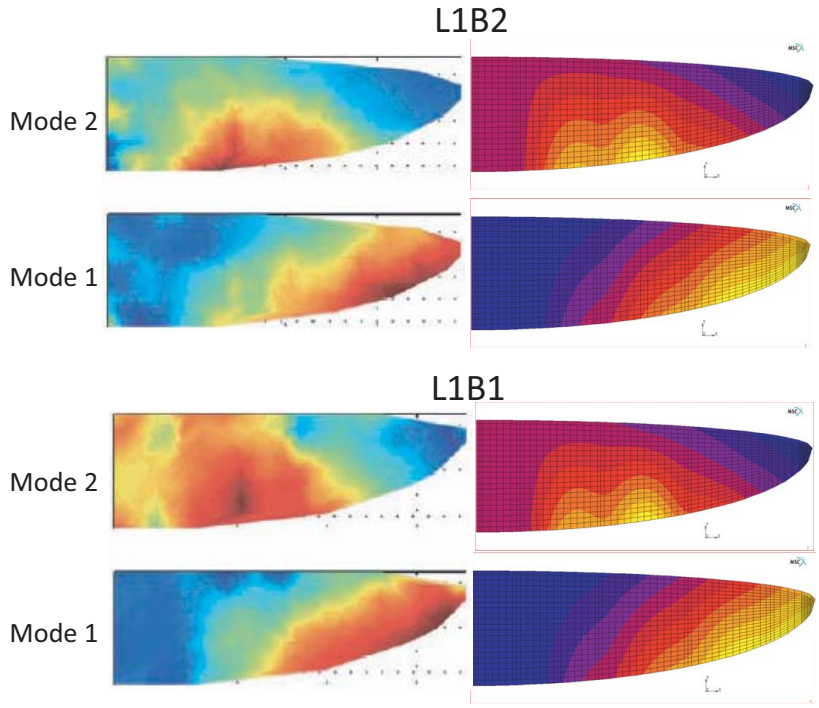

Figure 5.11: Comparison of mode shapes: Experiment [69] (left) and FE model - current study (right)

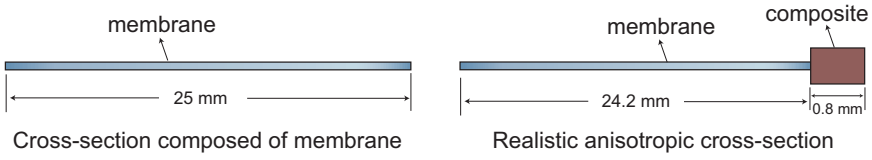

Figure 5.12: Cross sections used to compute mass ratios for the anisotropic wings.

	Mass ratio
Cross-section composed of membrane material	0.88 (lower bound)
Realistic cross-section	235 (L1B1)

Table 5.3: Mass ratios corresponding to sample cross-section of the wing

An examination of the experimentally determined mode shapes shows that the first mode has a predominant contribution from the skeleton; this indicates that the first measured frequency is a reasonable approximation to the first natural frequency.

The finite element models use the nominal values for the wing geometry, material and elastic properties. However, the elastic properties of the carbon fiber prepreg are modified by adjusting the recommended properties so as to obtain a reasonable overall correlation with experimentally obtained frequencies and mode shapes. The recommended and adjusted elastic properties are given in Table 5.4.

A comparison of the frequencies, shown in Table 5.5, indicates that there is reasonable agreement (approx 20% error) between the computed and measured values. The computations yield closely spaced modes, listed in Table 5.6, that contain a predominant contribution from the membrane. These modes were not identified in the experiments. However, the frequency spectrum obtained from the experiments [69] show several smaller peaks that were ignored. It is conceivable that these correspond to the closely spaced modes. The cases that show significantly higher error are identified in bold. The experiments indicate a decrease in the natural frequency for the second and third modes from 84 Hz and 126 Hz for L2B1 to 52 Hz and 84 Hz for L2B2. This decrease appears to be questionable based on the trends observed in the other configurations. This discrepancy may be due to the manner in which the modes were identified from the frequency response spectrum [69].

A qualitative comparison of the mode shapes obtained for L1B1 and L1B2 is shown in Figure 5.11. These results indicate that the FE model shows reasonable agreement

	Recommended values	Adjusted values used in the structural dynamic model
Carbon fiber prepreg (Properties of one layer)	$E_{11} = 233$ GPa $E_{22} = 23.1$ GPa $G_{12} = 3$ GPa G_{23}, G_{31} n/a $\nu_{12} = 0.05$ ν_{23}, ν_{31} n/a $\rho = 1740$ kg/m^3 Thickness = 0.1 mm	$E_{11} = 233$ GPa $E_{22} = 23.1$ GPa $G_{12} =$ **15.5** GPa (L1B1, L1B2) $G_{12} =$ **10.5** GPa (all other configs) $G_{23} = G_{31} = 1.7$ GPa $\nu_{12} = 0.05$ $\nu_{23} = \nu_{31} = 0.32$ $\rho = 1740$ kg/m^3 Thickness = 0.1 mm
Capran membrane (From experiments)	$E = 2.5 - 3.5$ GPa ν_{12} = n/a $\rho = 1160$ kg/m^3 Thickness = 12-20 microns	$E = 2.76$ GPa $\nu_{12} = 0.489$ (Incompressible) $\rho =$ **1384** kg/m^3 Thickness = 15 microns

Table 5.4: Material properties of the composite and membrane

Wing label		Mode 1	Mode 2
	Experiment	23	50
L1B1	FE model	21.5	49
	Experiment	22	45
L1B2	FE model	19.5	46.2
	Experiment	42	84
L2B1	FE model	47	88
	Experiment	41	**52**
L2B2	FE model	44	86.1
	Experiment	59	104
L3B1	FE model	65	107
	Experiment	67	n/a
L3B2	FE model	64	101

Table 5.5: Comparison of frequencies, in Hz, for various wing configurations

Wing label	Mode 1	Mode 2	Mode 3	Mode 4	Mode 5	Mode 6
L1B1	**21.5**	**49**	73.8	77.4	**106.5**	111.5
L1B2	**19.5**	**46.2**	74.2	78.5	**100.5**	107.5
L2B2	**47**	72	76.5	**88**	109	**118.8**
L2B2	**44**	74	78.7	**86.1**	109	**118.5**
L3B1	**65**	75.5	76.8	**107**	109	120
L3B2	**64**	78	79	**101**	109	120

Table 5.6: Computed frequencies, in Hz, for various wing configurations. Frequencies used for comparison with experiment are identified in bold.

with the experimental results for the cases considered.

The numerical simulations indicate that the in-plane shear moduli (G_{12}) of the materials used has a significant impact on the placement and spacing of frequencies. Therefore, additional studies that examine the sensitivity of the measured frequencies and the thrust generated due to variations in the material properties may be necessary.

5.4 Flapping Tests in Vacuum: Comparison of Tip Displacements

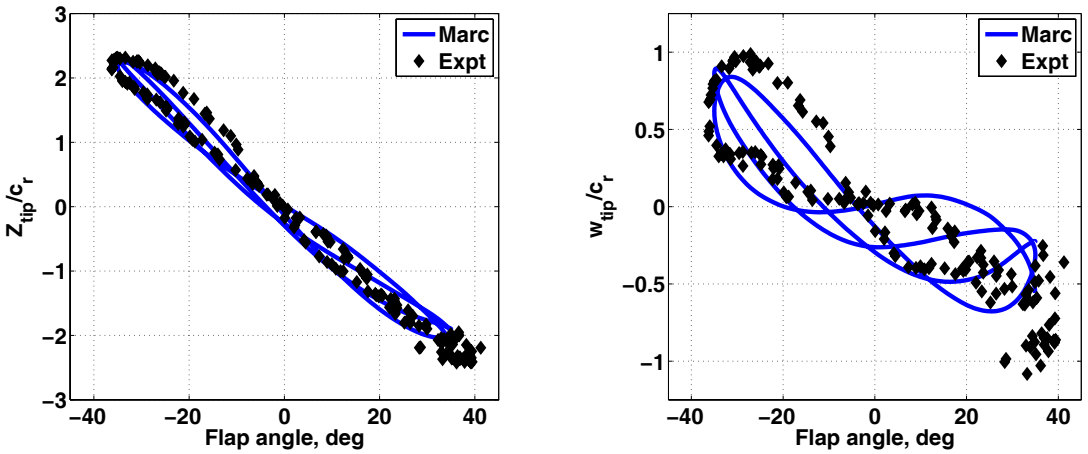

(a) Tip coordinate

(b) Tip deformation due to flexibility.

Figure 5.13: Tip coordinate and deformation due to flexibility of L2B1 flapping in vacuum.

A comparison of tip displacements of wing configurations L2B1 and L3B1 undergoing prescribed flap motion in vacuum are shown in Figures 5.13 and 5.14. The wings are undergoing a simple rotation about Y_W, shown in Figure 3.2, that is described by

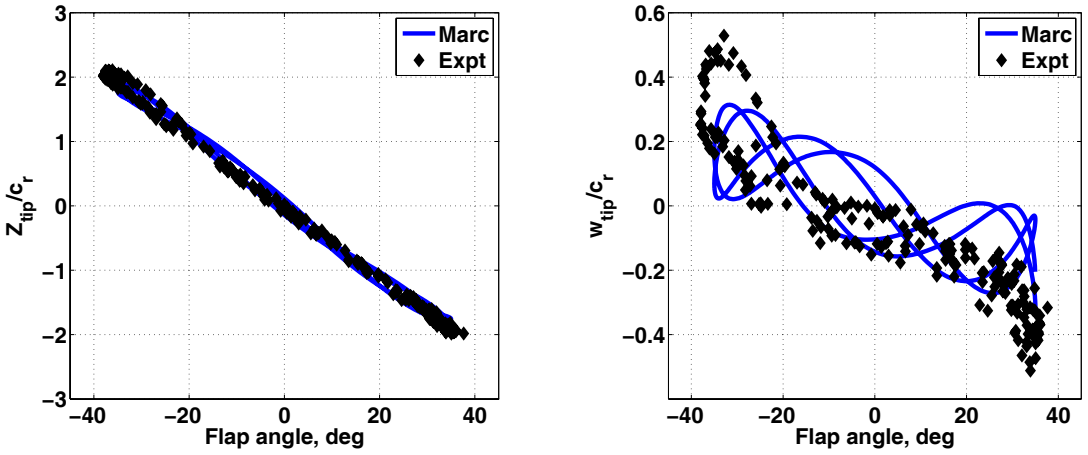

(a) Tip coordinate

(b) Tip deformation due to flexibility.

Figure 5.14: Tip coordinate and deformation due to flexibility of L3B1 flapping in vacuum.

the rotation vector shown in Eq (5.7).

$$\boldsymbol{\psi}_\beta = \beta_0 \sin(2\pi f t) \begin{Bmatrix} 0 \\ 1 \\ 0 \end{Bmatrix} \tag{5.7}$$

where $\beta_0 = 35^\circ$ and $f = 25$ Hz. Results using MARC were generated using the structural dynamic models and material properties described in the previous section and 400 time steps per flapping cycle were used to discretize the motion. The experimental results were obtained from Ref. [69]. Figures 5.13(a) and 5.14(a) show the Z coordinate of the wing tip, normalized using the root chord, measured in an inertial coordinate system that coincides with $X_W Y_W Z_W$ at the start of the motion. Figures 5.13(b) and 5.14(b) show the normalized Z coordinate of the wing tip in the instantaneous $X_W Y_W Z_W$ coordinate system. The results indicate that MARC shows reasonable agreement with the experimental measurements. Note that the experimental results were obtained by assuming that the tip deformation is periodic; consequently, the

data consists of tip displacements measured and averaged over several cycles. However, it is interesting to note that the computations show a cycle-to-cycle variation in the tip displacements. Moreover, in the experiments, the flapping stroke exceeded the intended amplitude of 35° due to uncertainties associated with the actuation mechanism [69]; this introduces additional discrepancies in the comparisons.

CHAPTER VI

Verification of the Aerodynamic Model

In this chapter, considerations involving the numerical implementation of the aerodynamic model are discussed. The results obtained are grouped as follows: (1) flat plate airfoils undergoing prescribed motion, (2) rigid Zimmerman wings in hover, and (3) rigid Zimmerman wings in forward flight. For all the cases considered, flow separation from the leading edge as represented by the leading edge vortex (LEV) is assumed to be present unless specified otherwise.

Digital Filters

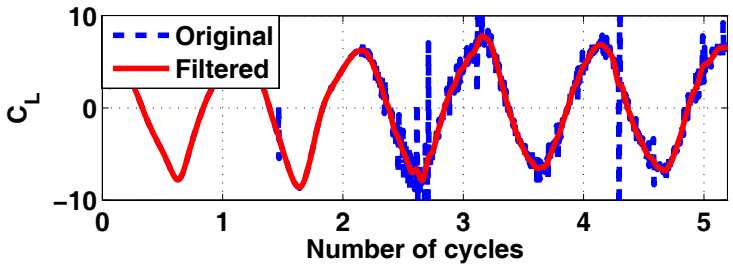

Figure 6.1: Sample comparison of original and filtered load signals

In all simulations using the approximate aerodynamic model, the unsteady force coefficients contain large amplitude high frequency oscillations caused by interaction

of the airfoil with previously shed vortices. The oscillations, which are a consequence of the discrete vortex representation of the wake, relate to two sources. First, the vortices are shed into the wake and these cluster and form regions of concentrated vorticity. These regions interact with the airfoil as it re-enters the wake to produce high frequency oscillations superimposed on the unsteady loads. Second, during numerical implementation, the boundary condition on the surface of the airfoil is enforced only at a finite number of points that is governed by the airfoil discretization (N_θ). Thus, a small number of vortices may pass through the airfoil when it enters a previously shed wake, causing an abrupt change in induced velocity and resulting in spikes in the load signal. Increasing the airfoil resolution and/or decreasing the size of the time step did not eliminate the noise. Similar problems have been noted by other researchers using discrete vortex approaches (Section 10.2, Ref. [100]). Several strategies, such as reflection of vortices when they approach too close to a body, re-discretization of the wake using sub-elements, or annihilation of vortices that pass through the airfoil, have been utilized to prevent abrupt changes in induced velocity [101]. These strategies, which introduce additional computational expense, delay but do not eliminate the problematic behavior of vortices, and are therefore not considered in this study due to their limited utility. A reduction in the magnitude of the numerical oscillations is essential before the unsteady loads can be applied on the flexible structure for aeroelastic simulation of flexible response. The numerical oscillations do not have a critical role when simulating rigid airfoils and wings. However, smoothing the signals improves clarity when comparing the time histories of the aerodynamic and aeroelastic forces with CFD based results.

The load signals, obtained from the approximate aerodynamic model for rigid cases as well as the aeroelastic calculations, are post-processed using zero-phase digital filters available in MATLAB® (version 8.0). The filters are implemented in MATLAB® using the *filtfilt* command as shown in Eq (6.1). A sample comparison of the original

and smoothed signals is shown in Figure 6.1.

$$y_{filtered} = \text{filtfilt}\left(B_f, A_f, y_{unfiltered}\right) \tag{6.1}$$

where B_f and A_f are filter coefficients based on Chebyshev functions that are arrays of length $\left(m_f + 1\right)$. The implementation of the zero-phase digital filters is summarized in Appendix C; additional information may be obtained from the extensive documentation provided in MATLAB®.

Circulation Limits and Cut-offs

A common assumption in the aerodynamic analysis of oscillating airfoils using approximate unsteady aerodynamic theories is that the flow leaves a sharp airfoil edge smoothly. However, Refs. [102, 103] note that for airfoils oscillating at sufficiently high frequencies, the flow turns around the sharp corner. This condition is applicable also to insect-like flapping wings during stroke reversal. In these situations, the stagnation condition at the LE (Eq. (3.30)) and the Kutta condition at the TE (Eq. (3.31)), which represent the constraint conditions on induced velocity derived assuming that the flow leaves the edges smoothly, are violated although the flow velocity and the strength of the shed vorticity are limited due to viscosity. Enforcing the constraint conditions in the approximate aerodynamic model (Eqs. (3.30) and (3.31)) results in the shedding of vortices that have unrealistically high circulation. These vortices cause severe wake distortion and can lead to numerical instabilities in the simulation. In this study, the constraint conditions at the LE and TE of the airfoil are relaxed during numerical implementation following Ref. [104]. The circulations of the latest shed vortices at each time step, computed using Eqs. (3.30) and (3.31), are modified using an ad hoc circulation limit, given by Eq. (6.2). The modified circulations may not satisfy the stagnation and Kutta conditions, and represent shed vorticity computed by relaxing

the constraint conditions.

$$\text{If} \quad \left| \frac{d\Gamma_{wk}^{t}}{d\Gamma_{wk}^{t-\Delta t}} \right| \geq \epsilon_{\Gamma} \quad \text{then} \quad d\Gamma_{wk}^{t} = \epsilon_{\Gamma}\, d\Gamma_{wk}^{t-\Delta t} \frac{d\Gamma_{wk}^{t}}{\left| d\Gamma_{wk}^{t} \right|} \quad \text{for} \quad d\Gamma_{wk}^{t} \neq 0 \tag{6.2}$$

where $d\Gamma_{wk}^{t-\Delta t}$ and $d\Gamma_{wk}^{t}$ denote strengths of vortices shed at consecutive time steps.

Literature indicates that caution should be exercised when using such ad hoc criteria [101]. Several simulations were conducted to determine suitable values of ϵ_{Γ} for the airfoil as well as the rigid wing cases described in this chapter. However, details of these simulations and justification for the choice of ϵ_{Γ} are provided only for the rigid wing cases (Section 6.2).

6.1 Airfoil Cases: Comparison with CFD for separated flow

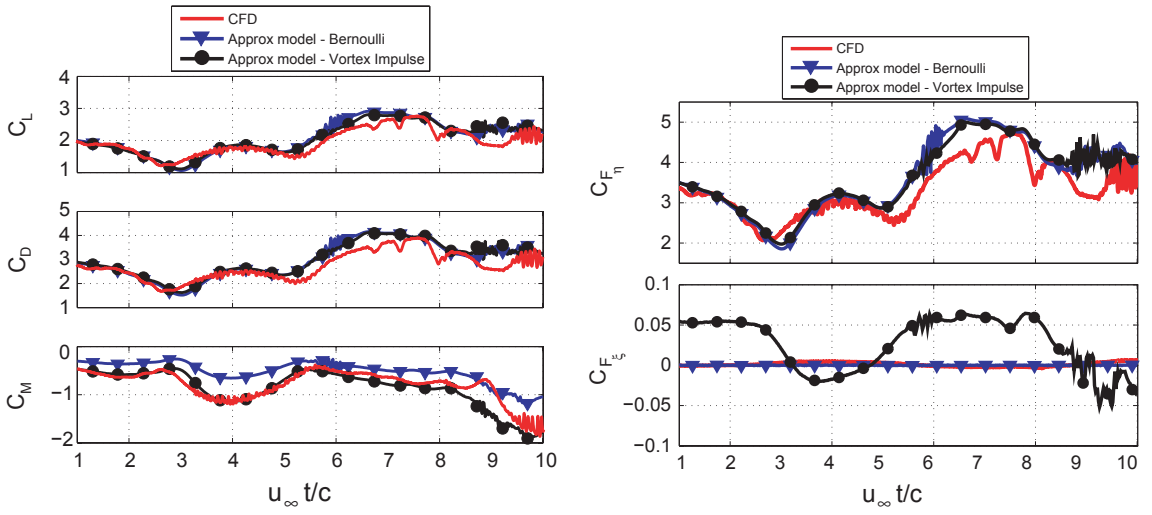

(a) Lift, drag, and moment.

(b) Forces normal and parallel to the airfoil chord.

Figure 6.2: Force coefficients for a flat plate at a fixed angle of attack in uniform flow.

A comparison of force coefficients for a zero thickness flat plate airfoil undergoing

prescribed motion are shown in Figures 6.2 and 6.3. The CFD computations were performed using the CFD++ code [105, 106], where the flow field was computed using the incompressible, unsteady, Reynolds-averaged NS equations using a finite volume formulation, on a grid that had approximately 500,000 points and 200 points on the surface of the airfoil. The CFD results were obtained by solving the laminar NS equations. Results based on the approximate model were obtained by assuming leading edge separation for the following parameters: $N_\theta = 100$, $n_{wksubit} = 4$, $r_c = 0.1c$. The unsteady loads were computed using both the vortex impulse method as well as the unsteady Bernoulli equation.

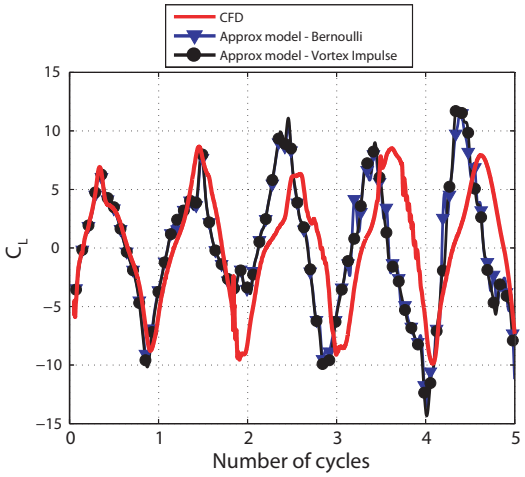

Figure 6.3: Force coefficients for a plunging airfoil.

Figure 6.2 shows the force coefficients obtained for an airfoil held at a fixed angle of attack, $\alpha = 55^o$, in a steady flow for the following parameters: $c = 1$m, $u_I = 1.5$m/s, $v_I = 0$m/s, $Re = 1.5 \times 10^6$, $\Delta t = 0.005c/u_I$. The circulation limit was fixed at 3.0. The force coefficients were defined as follows:

$$C_L = \frac{L}{\frac{1}{2}\rho_\infty U_I^2 c} \quad , \quad C_D = \frac{D}{\frac{1}{2}\rho_\infty U_I^2 c} \quad \text{,and} \quad C_M = \frac{M}{\frac{1}{2}\rho_\infty U_I^2 c^2} \tag{6.3}$$

where, the aerodynamic moment was calculated about the quarter-chord. Further-

more,

$$C_{F_\xi} = \frac{F_\xi}{\frac{1}{2}\rho_\infty U_I^2 c} \quad , \quad \text{and} \quad C_{F_\eta} = \frac{F_\eta}{\frac{1}{2}\rho_\infty U_I^2 c} \tag{6.4}$$

Figure 6.2(a) indicates that lift and drag computed using the vortex impulse method and the unsteady Bernoulli equation compare well with each other and show reasonable agreement with CFD. However, the moment computed using the vortex impulse method shows better agreement with CFD than that computed using the Bernoulli equation. This is probably due to the fact that small discrepancies in values of pressure, particularly near the edges of the airfoil, have a significant impact on calculation on moment. As discussed earlier, Figure 6.2(b) shows that the Bernoulli equation and vortex impulse method predict identical values of F_η but different values of F_ξ. Note that no filters were used for this case.

Figure 6.3 shows the force coefficients obtained for an airfoil undergoing prescribed plunge motion for the following parameters: $c = 0.1$m, $h(t) = c\sin(2\pi f t)$, $f = 1.592 \times 10^{-2}$ Hz, $\rho_\infty = 1788.92$kg/m^3, $Re = 1000$, and $\Delta t = 0.001/f$. A non-zero free stream velocity was required for the CFD simulations; therefore, $u_I = 0.0001$m/s and $v_I = 0$m/s was used so as to simulate 'near hover' conditions. The lift coefficient was defined as follows:

$$C_L = \frac{L}{\frac{1}{2}\rho_\infty U_{ref}^2 c} \quad \text{where} \quad U_{ref} = 2\pi f c$$

The results obtained from the approximate aerodynamic model were smoothed using a fourth order digital filter ($m_f = 4$) whose coefficients are given in Table 6.1. Figure 6.3 indicates that the vortex impulse method and the unsteady Bernoulli equation predict identical loads for normal to the chord. Moreover, the approximate model shows reasonable agreement with CFD for the cases considered. The differences observed can be attributed to the slightly different wake structures predicted by the approximate model and CFD computation. The wake structure affects the unsteady forces, particularly when an airfoil enters the wake shed during the previous cycles.

The forces generated by airfoils in hover are presented in Figures 6.4 and 6.5,

A_f	1	-3.0456	3.6243	-1.9780	0.4158
B_f	0.001	0.0041	0.0062	0.0041	0.001

Table 6.1: Filter coefficients

Case ID	Name	f, Hz	l_0	α_0	φ_α
1	Delayed rotation	$\frac{1}{2\pi}$	c	$\frac{\pi}{4}$	$\frac{\pi}{3}$
12	Synchronized rotation	$\frac{1}{3\pi}$	$1.5c$	$\frac{4\pi}{9}$	$\frac{\pi}{2}$

Table 6.2: Amplitudes and phase for airfoil kinematics. The case ids are obtained from Ref. [107]

whereas Figure 6.6 includes a free stream velocity and therefore corresponds to the case of forward flight. The lift and drag are components of the aerodynamic force along the η^I and ξ^I axes respectively. The airfoil kinematics are given by Eq. (6.5) and the parameters are shown in Table 6.2.

$$\begin{aligned} l(t) &= l_0 \sin(2\pi f t) \\ \alpha(t) &= \frac{\pi}{2} + \alpha_0 \sin\left(2\pi f t + \varphi_\alpha\right) \end{aligned} \tag{6.5}$$

where, the pitching is about the mid-chord. The results are obtained for $Re = 100$, $c = 1$m, $\rho_\infty = 1$ kg/m^3, $\nu_\infty = 0.01$ m^2/s, $U_{ref} = 1.0$ m/s, where Re and U_{ref} are defined as follows.

$$Re = \frac{U_{ref}\, c}{\nu_\infty} \qquad \text{and} \qquad U_{ref} = 2\pi f\, l_0 \tag{6.6}$$

The non-dimensional forces are defined as follows:

$$C_L = \frac{L}{\frac{1}{2}\rho_\infty U_{ref}^2} \quad \text{and} \quad C_D = \frac{D}{\frac{1}{2}\rho_\infty U_{ref}^2 c} \tag{6.7}$$

The CFD based results are obtained from Ref. [107]. The approximate loads, computed using the unsteady Bernoulli equation, were obtained for: $N_\theta = 200$, $r_c = 0.1\,c$, $n_{wksubit} = 4$, and circulation limit was fixed at 2.0. For both cases, CFD simulations

indicated that there was leading edge separation. However, for case 12, the vorticity shed from the LE was substantially weaker compared to that shed from the TE. Therefore, the approximate simulations for this case were also conducted assuming attached flow over the airfoil. For both cases, simulations using the approximate model were conducted assuming inviscid as well as viscous flow, wherein the effect of fluid viscosity was incorporated into the calculations as described earlier.

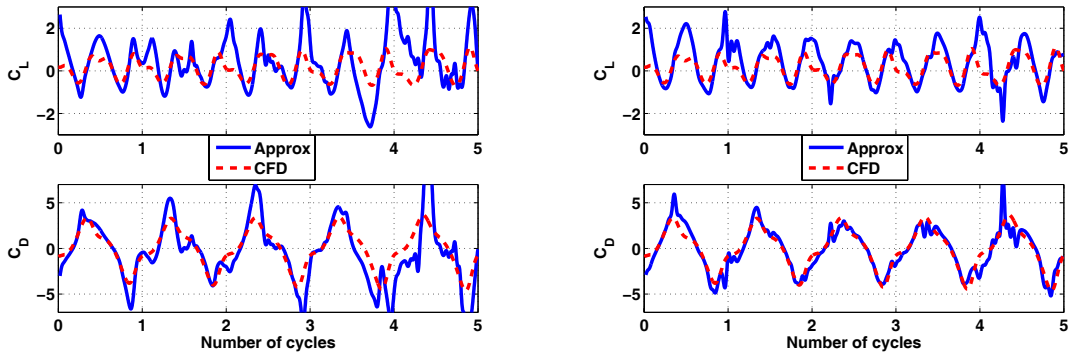

(a) Inviscid separated flow (b) Separated flow with viscous effects

Figure 6.4: Force coefficients for Case 1

The force coefficients obtained for case 1 are shown in Figure 6.4; results obtained by assuming inviscid flow and incorporating viscous effects are shown in Figures 6.4(a) and 6.4(b) respectively. Simulations with the approximate model were conducted by using 500 time steps per cycle to discretize the motion, and the load signals were smoothed using the filter described in Table 6.3. The comparisons indicate that incorporating the effect of viscosity improves correlation with CFD based results. The improvement is noticeable for C_D in particular. These results suggest that the influence of fluid viscosity in the interactions involving shed vorticity is important for this case.

The force coefficients obtained for case 12 are shown in Figure 6.5. Simulations assuming separated and attached flows were conducted by using 800 and 500 time steps per cycle respectively, and the loads obtained were smoothed using filters de-

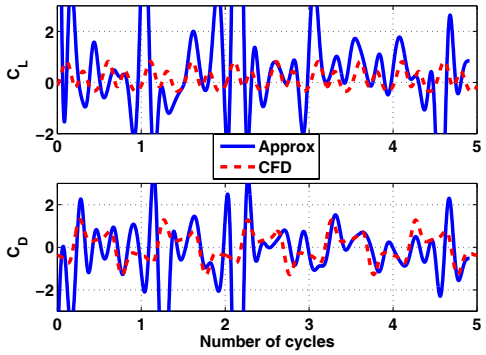

(a) Inviscid separated flow

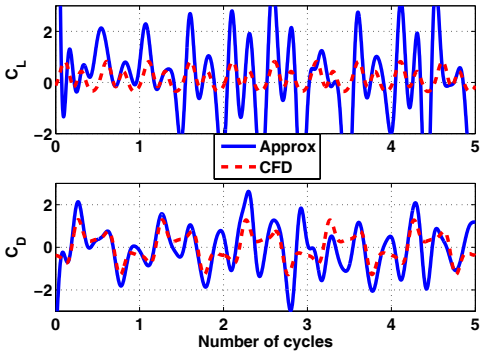

(b) Separated flow with viscous effects

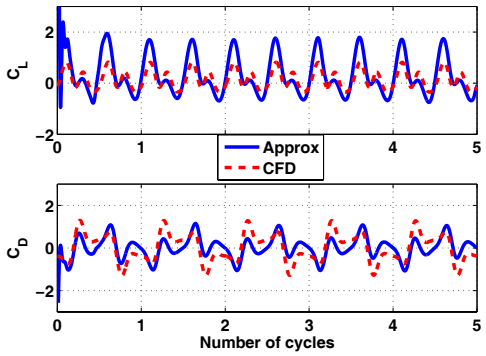

(c) Inviscid attached flow

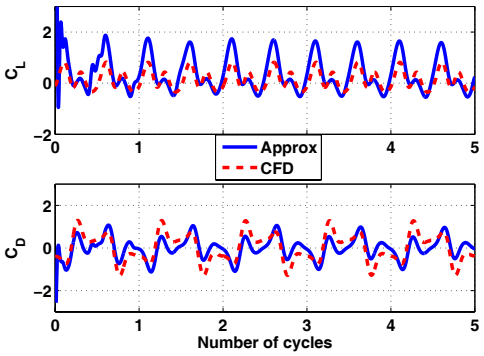

(d) Attached flow with viscous effects

Figure 6.5: Force coefficients for Case 12

scribed in Tables 6.3 and 6.4 respectively. The results with separated flow, shown in Figures 6.5(a) and 6.5(b), indicate that the inviscid approximate model does not compare well with CFD for this case. Incorporating viscous effects improves correlation slightly, as shown in Figure 6.5(b); however, the improvement is most noticeable in the first and second cycles of C_D. Results obtained by assuming attached flow, shown in Figures 6.5(c) and 6.5(d), show that the approximate results agree with CFD based results. However, some of the peaks in C_D are not adequately captured. Incorporating viscous effects improves correlation slightly, but the effect seems to be minor for this case. These results suggest that when the vortical generation from the LE is weak, a dominant contribution to the aerodynamic loads is from the TE vortices.

The forces generated by the airfoils in the presence of a free stream are shown

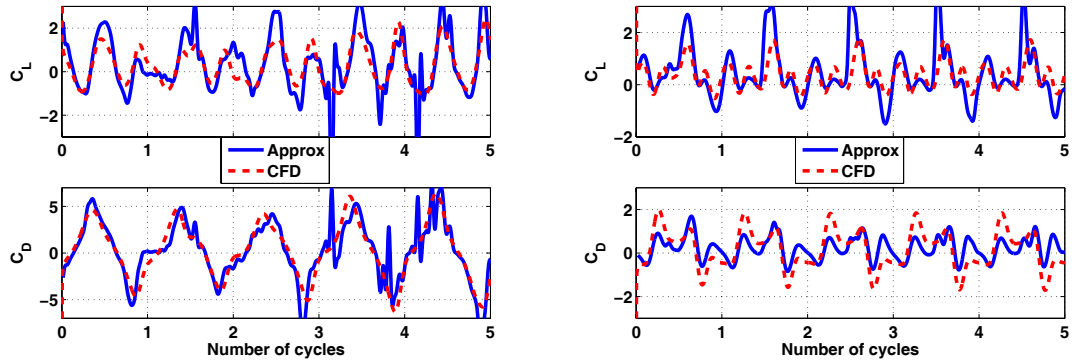

(a) Case 1: separated flow with viscous effects (b) Case 12: attached flow with viscous effects

Figure 6.6: Force coefficients for Cases 1 and 12 with free stream

in Figure 6.6. The kinematics are the same as those used in cases 1 and 12, and a free stream velocity vector that is parallel to ξ^I is now introduced. The free steam velocity is equal to $0.2U_{ref}$, where U_{ref} is given in Eq. (6.7). Simulations using the approximate model were conducted by assuming separated flow for case 1, attached flow for case 12, and including the effect of viscosity. The results were obtained by using 500 time steps per cycle, and subsequently smoothed using the filter described in Table 6.3. The comparisons indicate that the approximate model shows reasonable agreement with CFD for the cases considered. In particular, comparisons for case 12, shown in Figure 6.6(b), indicate that the discrepancy in the peaks of C_D is somewhat larger compared to the discrepancy observed for case of hover; this may be attributed to the increased contribution of vorticity shed from the LE.

A_f	1.0000	-3.5379	4.7367	-2.8414	0.6439
B_f ($\times 10^{-3}$)	0.0797	0.3186	0.4779	0.3186	0.0797

Table 6.3: Filter coefficients

A_f	1.0000	-3.9109	5.7376	-3.7423	0.9156
B_f ($\times 10^{-6}$)	0.1517	0.6067	0.9101	0.6067	0.1517

Table 6.4: Filter coefficients

6.2 Rigid Zimmerman Wings in Hover

The forces generated by rigid Zimmerman wings undergoing prescribed flapping motion are shown in Figures 6.7, 6.8, 6.9 and 6.10. Note that the lift and thrust are the components of the aerodynamic force resolved along Y_{SP} and Z_{SP}, shown in Figure 3.5 respectively; the corresponding non-dimensional quantities are defined in Eq (6.8). Furthermore, X_W and Y_W, shown in Figure 3.2, coincide with X_{SP} and Z_{SP}, respectively at the start of the motion. The flapping motion, which corresponds to a simple rotation about Y_W, is described by the rotation vector shown in Eq. (5.7). Furthermore, the transient aerodynamic loads obtained using the approximate model, for the rigid as well as subsequent flexible cases considered, are calculated using Bernoulli equation.

$$C_L = \frac{L}{\frac{1}{2}\rho_\infty U_{ref}^2 R_{span} c_r} \quad \text{and} \quad C_T = \frac{T}{\frac{1}{2}\rho_\infty U_{ref}^2 R_{span} c_r} \quad \text{where} \quad U_{ref} = 4R_{span}\beta_0 f \tag{6.8}$$

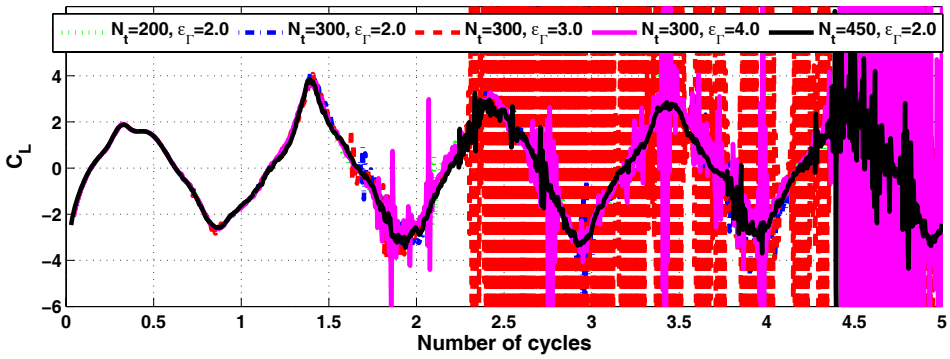

Figure 6.7: Lift coefficients for $\beta_0 = 35°$, $f = 10$ Hz for various N_t and ϵ_Γ

Simulations were conducted to determine the impact of ϵ_Γ, $N_{section}$, N_θ, and N_t on the forces generated by flapping wings. The unfiltered non-dimensional lift, obtained for $\beta_0 = 35°$ and $f = 10$ Hz, are shown in Figures 6.7 and 6.8. Comparisons for thrust are similar and therefore not presented. The numerical experiments were conducted in air ($\rho_\infty = 1.209$ kg/m^3 and $\nu_\infty = 1.568 \times 10^{-5}$ m^2/s). The vortex core radius

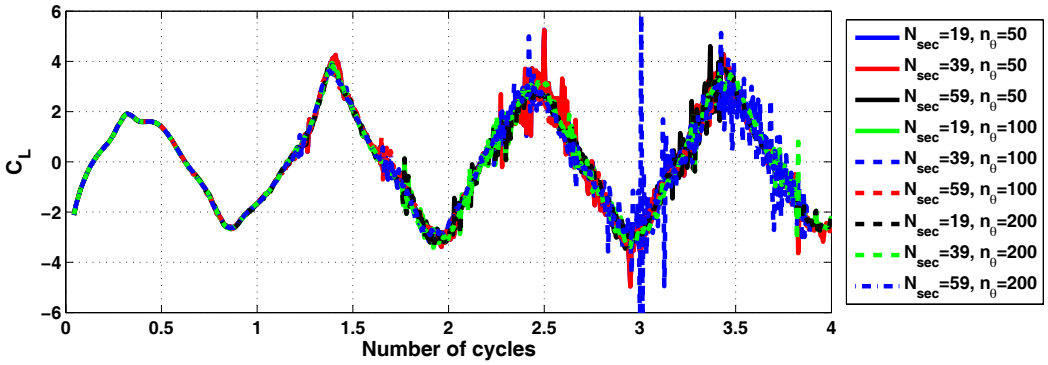

Figure 6.8: Lift coefficients for $\beta_0 = 35°$, $f = 10$ Hz for various $N_{section}$ and n_θ

and number of sub-iterations in the wake were fixed at $r_c = 0.1c$ and $n_{wksubit} = 4$ respectively. Comparisons of C_L for various combinations of N_t and ϵ_Γ are shown in Figure 6.7. The loads generated over one and half cycles are nearly identical for all the combinations considered. However, the amount of noise in the signal is significant for $\epsilon_\Gamma = 3.0$ and $\epsilon_\Gamma = 4.0$. The results indicate that $\epsilon_\Gamma = 2.0$ adequately captures the loads generated by the wing while limiting the noise to reasonable levels. Therefore, the circulation limit used in all subsequent simulations, using rigid as well as flexible wings, is fixed at 2.0. Figure 6.7 also shows that the loads generated for various values of N_t are nearly identical. Note that $N_t = 200$ and $N_t = 450$ represent discretizations in which incremental rotations per time step at the root are 0.7° and 0.31° respectively. Therefore, the values of N_t in subsequent simulations are chosen so that the incremental rotations lie in this range.

The unfiltered loads generated by the wings for various combinations of $N_{section} = \{19, 39, 59\}$ and $N_\theta = \{50, 100, 200\}$ are shown in Figure 6.8. It is evident that the differences in the loads are relatively minor, indicating that any combination of $N_{section}$ and N_θ may be chosen without a significant loss in accuracy. Note that increasing N_θ reduces the noise in the signal. Due to the limited number of cases considered in this dissertation, results were obtained using a somewhat conservative choice of $N_{section} = 59$ and $N_\theta = 100$. A lower resolution, which is computationally

less expensive (see Appendix D), may be used when conducting extensive parametric studies.

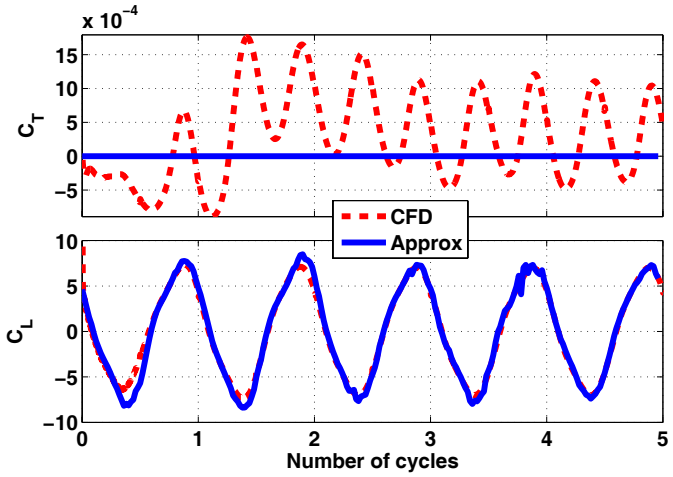

Figure 6.9: Force coefficients generated by a rigid wing undergoing prescribed flapping motion with amplitude of 5°

Figure 6.9 shows the non-dimensional lift and thrust generated by the wing for $\beta_0 = 5°$ and $f = 10$ Hz. For this case $Re = 426$, where the Reynolds number is calculated using the root chord and maximum tip speed based on the flapping motion of the rigid wing as shown in Eq. (6.9).

$$Re = \frac{U_{tip} c_r}{\nu_\infty} \quad \text{where} \quad U_{tip} = 2\pi f R_{span} \beta_0 \tag{6.9}$$

The CFD based results, which are presented in Ref. [82], were computed using the numerical framework that is described in Refs. [78, 79]. Simulation using the approximate model was conducted using 200 time steps per flapping cycle to discretize the motion. Subsequently, a fourth order filter ($m_f = 4$) described in Table 6.5 was used to smooth the results. The results, shown in Figure 6.9, indicate that the lift computed using the approximate aerodynamic model compares well with the corresponding CFD based quantity for the case considered. Note that due to the lack of wing pitch or twist, the thrust corresponds to aerodynamic force parallel to the chordwise direction of the

wing. In the approximate computations, the wing is assumed to have zero thickness; consequently, the force parallel to the wing chord is equal to zero. In the CFD based computations, this quantity is equal to the sum of viscous forces on the wing surface and the suction pressure on the edges of the wing; the results indicate that the thrust obtained from CFD based calculations is several orders of magnitude lower than the lift.

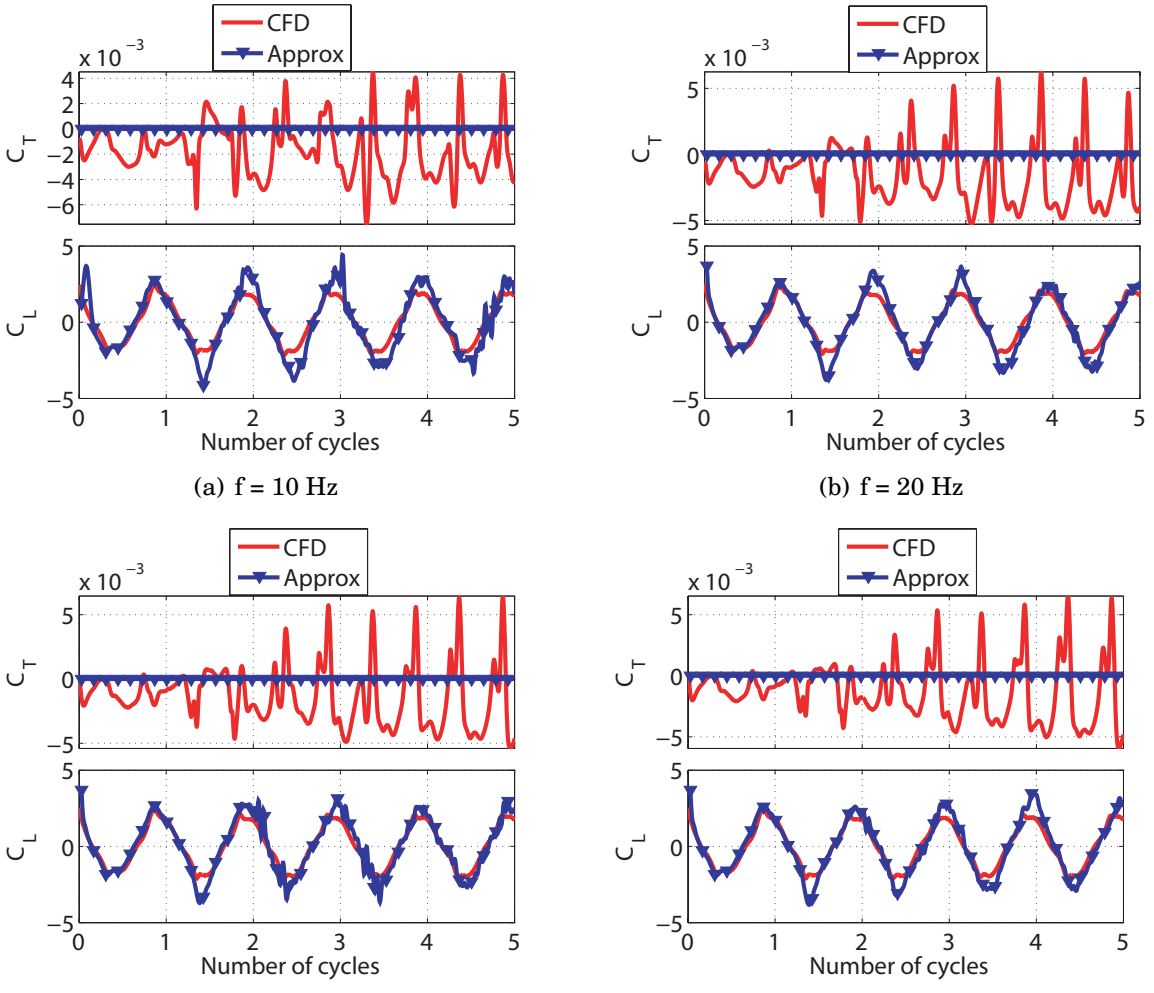

(a) f = 10 Hz

(b) f = 20 Hz

(c) f = 30 Hz

(d) f = 40 Hz

Figure 6.10: Force coefficients generated by rigid wings undergoing prescribed flapping motion with amplitude of 35°

The non-dimensional lift and thrust for $\beta_0 = 35°$ and $f = \{10, 20, 30, 40\}$ Hz are shown in Figures 6.10 and 6.11. The Reynolds numbers for these cases, calculated

A_f	1	-2.0345	1.9478	-0.9135	0.1766
B_f	0.0110	0.0441	0.0661	0.0441	0.0110

Table 6.5: Filter coefficients

using Eq. (6.9), are 4387, 8775, 13163, and 17550 respectively. The CFD simulations were conducted using the numerical framework described in Refs. [46, 108]. Simulations using the approximate and CFD based models were conducted using 300 and 500 time steps per flapping cycle to discretize the motion respectively. Subsequently, a fourth order filter ($m_f = 4$) described in Table 6.6 was used to smooth the signals obtained using the approximate model. The results indicate that the approximate model over-predicts the lift compared to CFD simulation; the mean and maximum errors in the peak lift are 50% and 100% respectively. The discrepancy may be attributed to the spanwise flow and tip vortices that may be important for the combination of amplitude and flapping frequencies considered; note that these aspects are not incorporated in the approximate aerodynamic model.

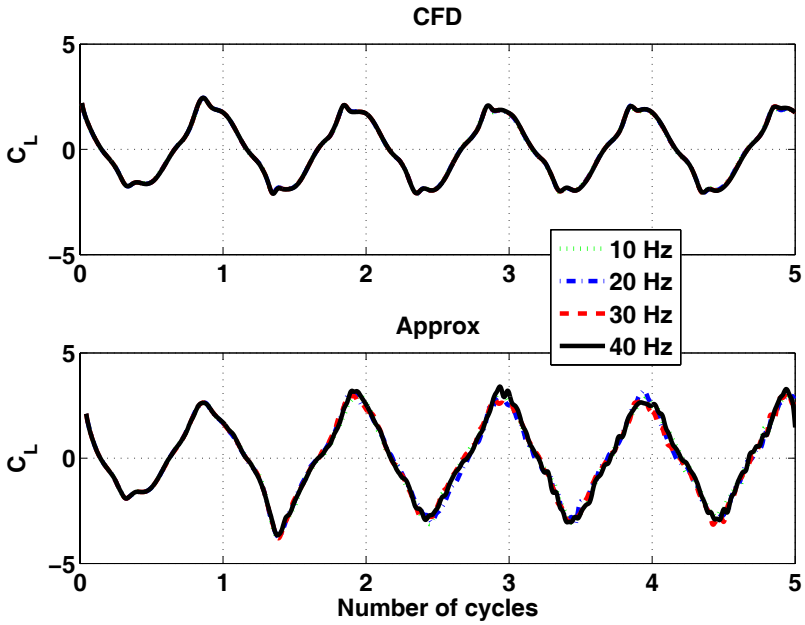

Figure 6.11: Lift coefficients generated by rigid wings for $\beta_0 = 35°$.

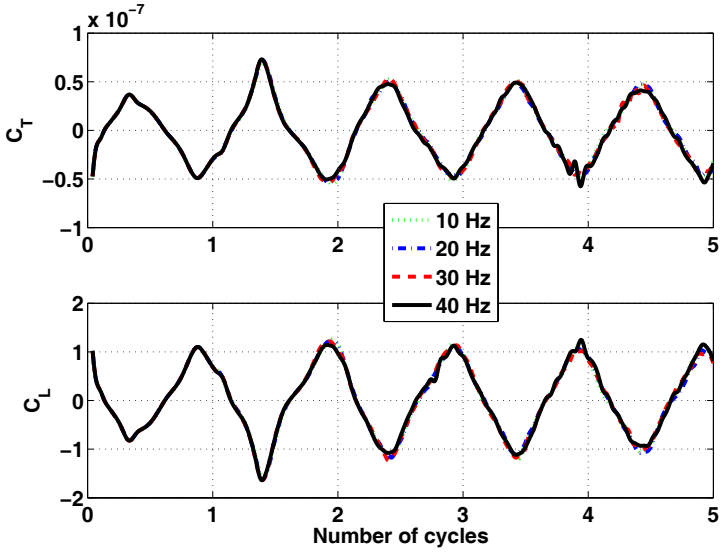

Figure 6.12: Lift and thrust coefficients, calculated using the approximate model, generated by rigid wings for $\beta_0 = 18°$.

The time histories of C_L for all the flapping frequencies considered is shown in Figure 6.11, wherein the CFD based and approximate results are shown on separate plots. The thrust was several orders of magnitude lower than lift; consequently comparisons involving this quantity are not shown. It is interesting to note that the lift coefficients, computed for various frequencies, are very similar. This trend indicates that C_L is somewhat insensitive to Reynolds number. Furthermore, based on the definition of C_L in Eq. (6.8), it follows that the peak lift is proportional to the square of the flapping frequency. Similar trends are obtained from simulations using the approximate model for $\beta_0 = 18°$, as shown in Figure 6.12, indicating that the relation between the lift and flapping frequency is insensitive to flapping amplitude.

A_f	1	-3.0456	3.6243	-1.9780	0.4158
B_f	0.0010	0.0041	0.0062	0.0041	0.0010

Table 6.6: Filter coefficients

The forces generated by rigid wings undergoing prescribed combined flap-pitch motion are shown in Figures 6.13, 6.14, 6.15, and 6.16. The wing kinematics are

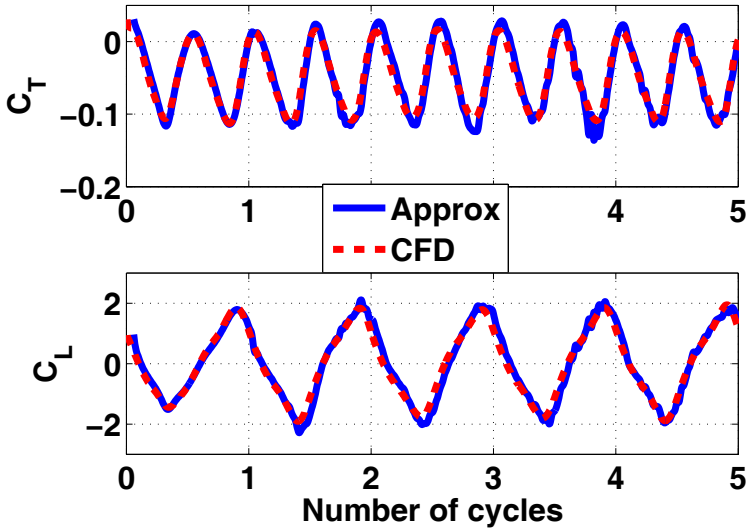

Figure 6.13: Force coefficients generated by a rigid wing undergoing combined pitch-flap motion. $\beta_0 = 10°$, $\alpha_0 = 5°$

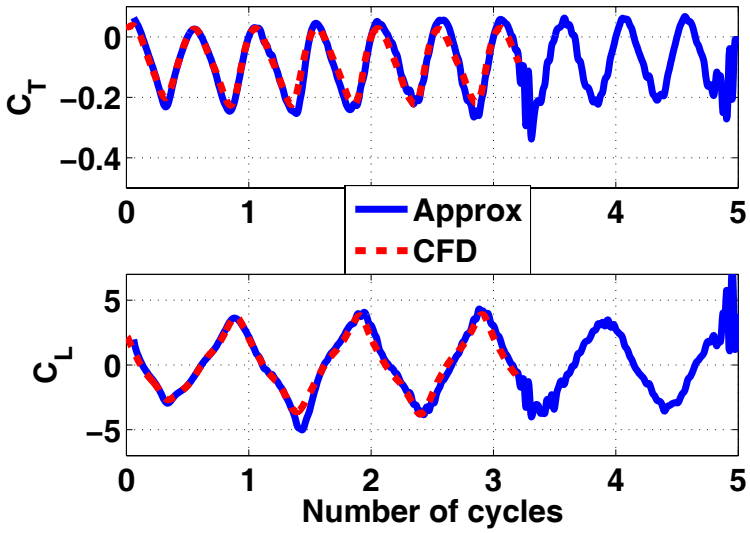

Figure 6.14: Force coefficients generated by a rigid wing undergoing combined pitch-flap motion. $\beta_0 = 15°$, $\alpha_0 = 5°$

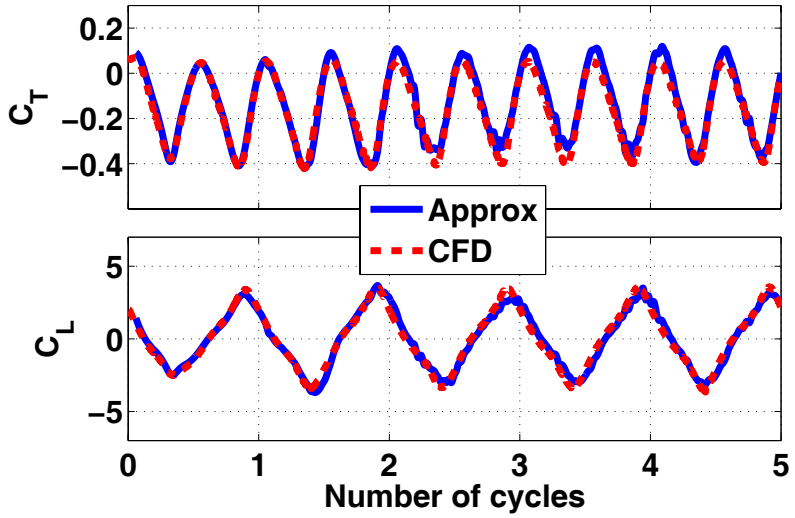

Figure 6.15: Force coefficients generated by a rigid wing undergoing combined pitch-flap motion. $\beta_0 = 15°$, $\alpha_0 = 10°$

described by the following Euler rotations: a flapping rotation about Y_W described by Eq. (5.7) followed by a feathering motion about X_W described by Eq. (6.10); where, X_W, indicated in Figure 3.2, originates at the quarter-chord point of the root. The parameters for which the results are obtained are summarized in Table 6.7. For all the results presented, the approximate simulations and CFD were conducted by using 500 and 200 time steps per flapping cycle respectively. Comparisons, shown in Figures 6.13, 6.14, and 6.15, indicate that the approximate model shows reasonable correlation with CFD for the cases considered. The time histories of C_L and C_T, computed using the approximate model for f = 10 Hz, 20 Hz, 30 Hz, and 40 Hz, are shown in Figure 6.16. The Reynolds numbers for these cases, calculated using Eq. (6.9), are 1880, 3761, 5641, and 7520 respectively. The results clearly show that the force coefficients computed at various flapping frequencies are very similar, indicating that the aerodynamic forces scale with f^2. Note that a similar trend was obtained for rigid wings undergoing prescribed flap motion.

$$\boldsymbol{\psi}_\alpha = -\alpha_0 \sin(2\pi f t) \begin{Bmatrix} 1 \\ 0 \\ 0 \end{Bmatrix} \tag{6.10}$$

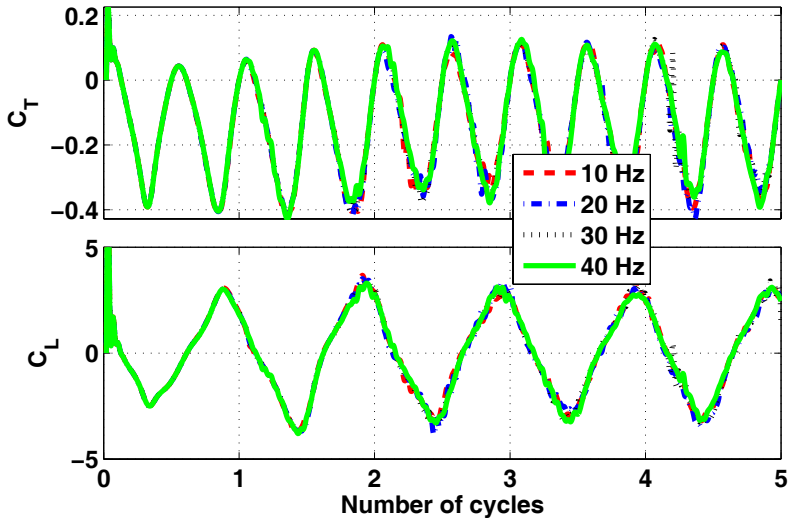

Figure 6.16: Force coefficients generated using the approximate aerodynamic model for rigid wings undergoing combined pitch-flap motion. $\beta_0 = 15°$, $\alpha_0 = 10°$, for various frequencies

Figure Number	Flap amplitude	Pitch amplitude	f
6.13	10°	5°	10 Hz
6.14	15°	5°	10 Hz
6.15	15°	10°	10 Hz
6.16	15°	10°	10,20,30,40 Hz

Table 6.7: Figures corresponding to various combined flap-pitch cases.

6.3 Rigid Zimmerman Wing in Forward Flight

The forces generated by rigid wings in forward flight are presented. As mentioned, forward flight is characterized by a free stream velocity vector that is assumed to lie in the $Y_{SP} - Z_{SP}$ plane as indicated in Figure 3.4. The components of the free stream

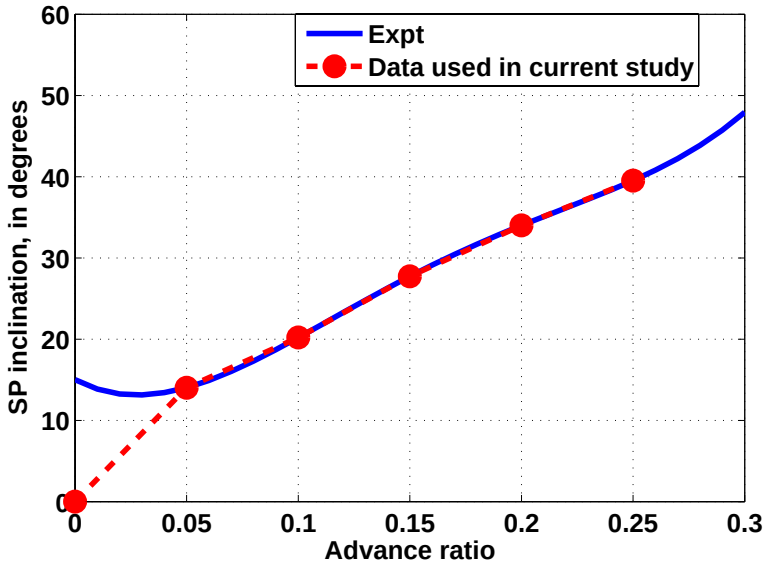

Figure 6.17: Combinations of advance ratio and SP inclination: Expt - Experimental data [21].

velocity are determined from the tip speed, advance ratio, and stroke plane inclination angle, using Eq. (3.1) as described earlier. The results are generated for combinations of μ and β_{sp} that are based on experimentally obtained data for hawkmoths in forward flight [21]. The specific combinations used in the current study, which are based on the data obtained for Moth M1 in Ref. [21], are shown in Figure 6.17 and listed in Table 6.8.

μ	0	0.05	0.10	0.15	0.20	0.25
β_{sp}	0°	14°	21.2°	27.7°	34°	40°

Table 6.8: Combination of advance ratios and stroke plane inclinations used in the current study

The non-dimensional lift generated by rigid wings for $\beta_0 = 35°$, $f = 10$ Hz, and various advance ratios, are shown in Figure 6.18. The thrust generated was several orders of magnitude lower than lift; therefore, comparisons involving this quantity are not presented. The CFD and approximate simulations were conducted by using 500 and 300 time steps per flapping cycle respectively and results obtained using the

approximate model were smoothed using the filter described in Table 6.6. Comparisons indicate that the approximate model shows reasonable agreement with CFD based results for the cases considered. The correlation between the results improves as advance ratio increases. The time histories indicate that the peak-to-peak forces decreases with increasing advance ratio. A comparison of the mean lift coefficients, which represent the time averaged values of C_L, is shown in Figure 6.19. This result indicates that the mean lift decreases (becomes more negative) with increase in forward flight speed; furthermore, the approximate model shows reasonable agreement with the CFD based result and also captures the trend. The results shown in Figures 6.18 and 6.19 demonstrate that the modified aerodynamic model can be used to conduct trend type studies for wings in forward flight despite of the simplifying assumptions.

The non-dimensional forces generated by rigid wings for $\beta_0 = 20°$, $\mu = 0.25$, for various flapping frequencies are shown in Figures 6.20, 6.21, and 6.22. The Reynolds numbers corresponding to f = 2.5 Hz and 10 Hz, calculated using Eq. (6.9), are 626 and 2507 respectively. The CFD and approximate simulations were conducted by using 500 and 200 time steps per flapping cycle respectively; results obtained using the approximate model were smoothed using the filter described in Table 6.6. Comparisons indicate that the approximate model shows reasonable agreement with CFD based results for the cases considered. The time histories of C_L for f = 2.5 Hz and 10 Hz are shown in Figure 6.16. It is evident that the force coefficients computed at various flapping frequencies are very similar, indicating that the aerodynamic forces scale with f^2. This result, combined with the trends obtained previously for wings in hover, seem to imply that the predominant unsteady aerodynamic force generating mechanisms for flapping wings in hover and forward flight are somewhat insensitive to Reynolds number and the forces scale with the square of frequency for a given kinematic pattern. However, the impact of wing planform on this finding has to be examined.

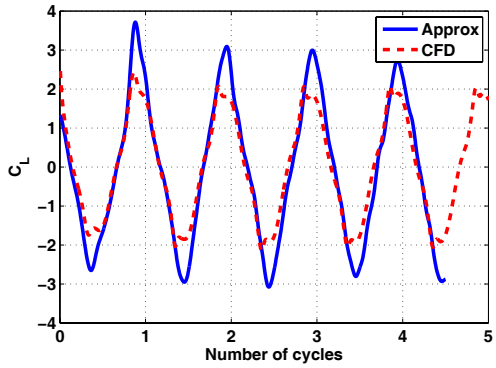

(a) $\mu = 0.0$

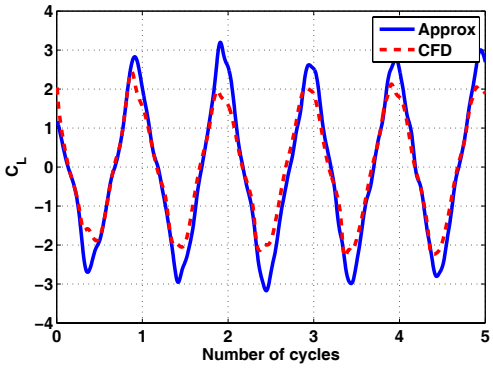

(b) $\mu = 0.05$

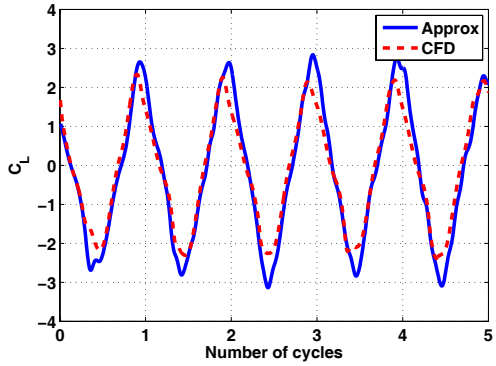

(c) $\mu = 0.10$

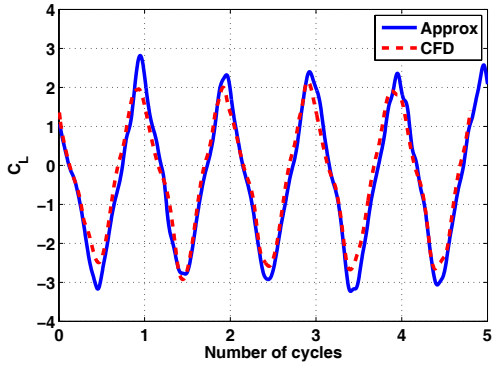

(d) $\mu = 0.15$

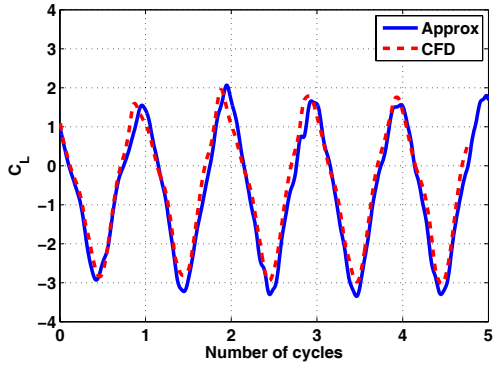

(e) $\mu = 0.20$

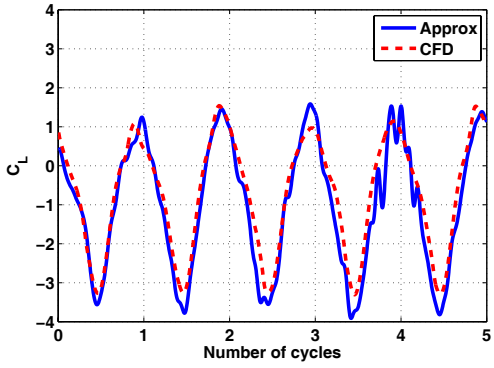

(f) $\mu = 0.25$

Figure 6.18: Force coefficients generated by rigid wings in forward flight: $\beta_0 = 35°$, $f = 10$ Hz

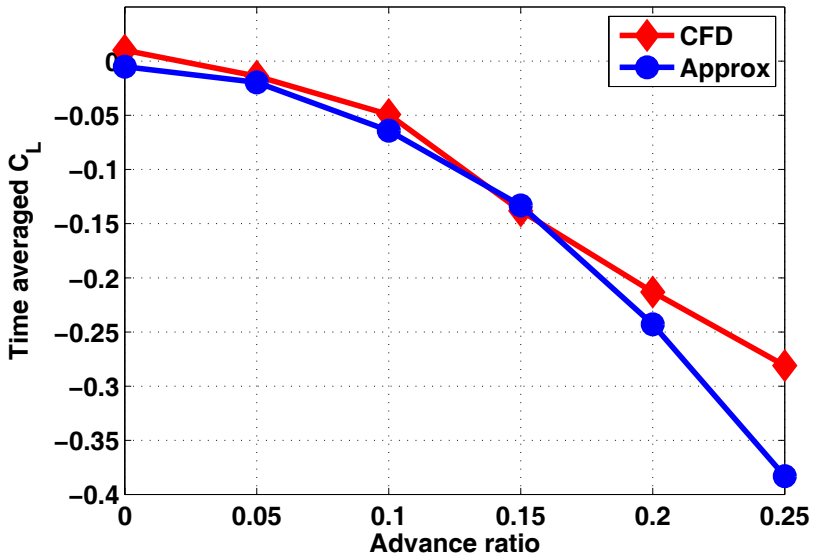

Figure 6.19: Mean lift generated by rigid wings in forward flight.

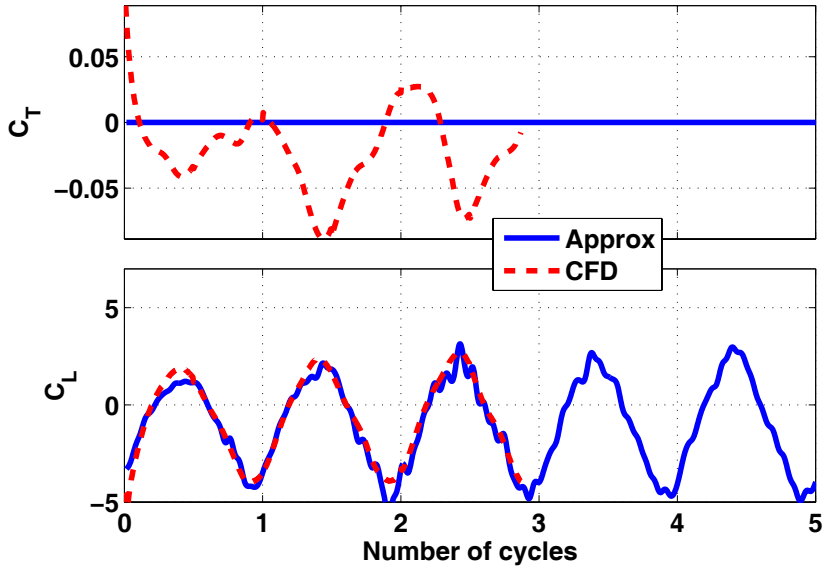

Figure 6.20: Force coefficients generated by rigid wings in forward flight: $\beta_0 = 20°$, $f = 2.5$ Hz, $\mu = 0.25$

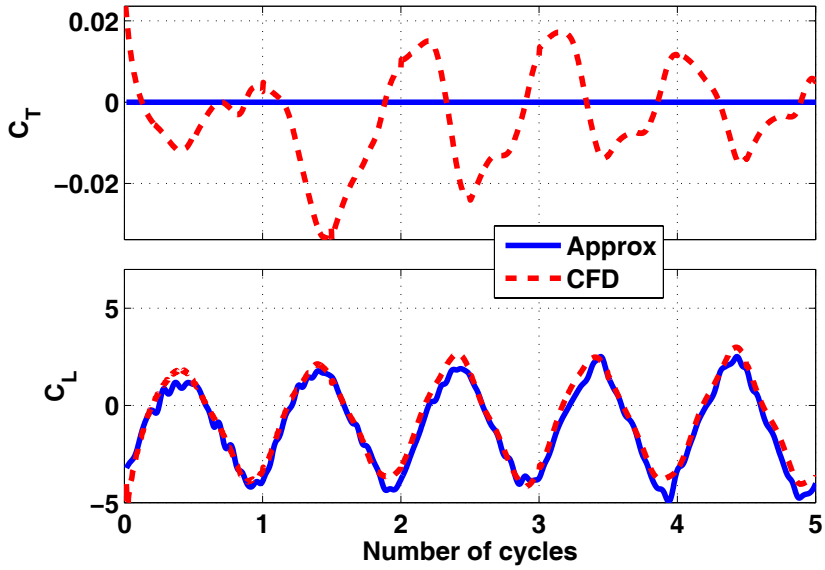

Figure 6.21: Force coefficients generated by rigid wings in forward flight: $\beta_0 = 20°$, $f = 10$ Hz, $\mu = 0.25$

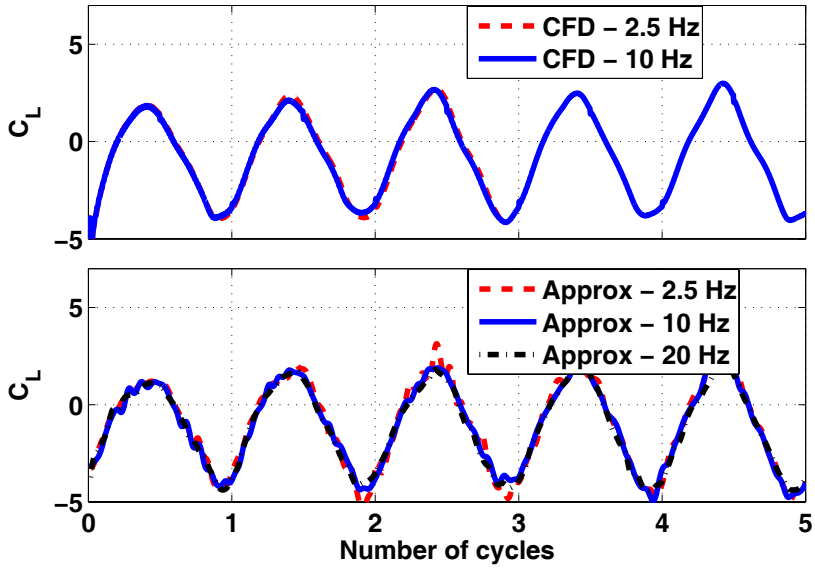

Figure 6.22: Force coefficients generated by rigid wings in forward flight: $\beta_0 = 20°$, $\mu = 0.25$

CHAPTER VII

Aeroelastic Studies

Aeroelastic studies were conducted using isotropic and anisotropic wings in hover and forward flight for a variety of wing kinematics. The studies are separated as follows: (1) preliminary tests on the aeroelastic interface, (2) flexible wings in hover, and (3) flexible wings in forward flight.

7.1 Preliminary Calculations using the Aeroelastic Interface

The results presented in this section are used to determine whether MARC can be used to impose pressure loads, which can later be replaced with aerodynamic loads, on a plate that is undergoing prescribed large amplitude rigid body motion. First, the simultaneous application of a uniform pressure load and large amplitude rigid body motion on a plate is examined.

A plate with dimensions $R_{span} = 0.1$ m, $b = 0.025$ m, and $t_h = 0.001$ m, was chosen. The plate is assumed to be made of a hypothetical material that has elastic modulus $E = 2.1 \times 10^{10}$ N/m^2, Poisson's ratio $\nu = 0.3$, and density $\rho = 20$ kg/m^3. The finite element model of the plate was composed of 440 shell elements (Element type 75 in MARC). A low value of density was selected so as to reduce the effect of inertial loads due to flapping motion thus guaranteeing that the flexible deformation of the flapping

Pressure N/m^2	Flapping case $\times 10^{-3}$ m	Static case $\times 10^{-3}$ m
500	3.352	3.353
10,000	61.79	61.59

Table 7.1: Comparison of tip displacement for static and flapping case.

plate is due mainly to the externally applied load. This implies that the displacements obtained for a flapping plate with external load can be compared to those obtained for a static plate that is cantilevered along the flapping edge with the same applied load. Two cases of uniform pressure loads, $\Delta p_1 = 500$ N/m^2 and $\Delta p_2 = 10,000$ N/m^2, which resulted in small and large edge displacements respectively were examined. Here, "small" displacements imply displacements that are of the order of the plate thickness. For the flapping plate, the pressure loads were superimposed with large amplitude 2D rotations, described by the rotation vector in Eq. (5.1) where $f = 5$ Hz. A time step of $\Delta t = 2 \times 10^{-3}$ seconds was used. At each time step, the magnitude of the displacement at point P that has coordinates (0.1,0,0) in (X_W, Y_W, Z_W) due to flexibility is obtained. The results obtained for the static plate with pressure load and flapping plate with pressure load are summarized in Table 7.1. The results indicate that pressure loads can successfully be imposed on a plate that is flapping with large amplitude rigid body motion.

7.2 Flexible Flapping Wings in Hover

The results are obtained for isotropic and anisotropic wings that were based on the Zimmerman planform [69]. The finite element models of the wings, shown in Figure 3.2, were obtained using 1263 thick shell elements (Element type 75 in MARC). The wing sections described by the structural mesh, shown in Figure 3.2, are conveniently used as the spanwise stations during the aerodynamic analysis. The

airfoil discretization for the aerodynamic analysis is typically more refined than the number of elements along the chord in the structural dynamic model. Therefore, the chordwise distributions of deformation and velocities are linearly interpolated to obtain the corresponding quantities for the airfoil. The pressure distribution imposed on each structural element along the chord is assumed to be constant, and is computed from the pressure distribution on the airfoil using Eq. (7.1).

$$p_j\Big|_{struc} = \frac{\int_{\xi_j}^{\xi_{j+1}} p(\xi)\Big|_{aero} d\xi}{\left(\xi_{j+1} - \xi_j\right)} \qquad \text{for} \quad j = 1, 2, \cdots, (n_c - 1) \tag{7.1}$$

Pressure Limits

During the simulations, a pressure based filter that is described by Eq. (7.2) was used to limit the magnitude of numerical noise that is transmitted to the flexible wing; note that the limit should be sufficiently high so as not to introduce significant errors during calculations.

$$p_{applied} = \begin{cases} -p_{limit} & \text{if} \quad p_{calculated} \le -p_{limit} \\ p_{calculated} & \text{if} \quad -p_{limit} \le p_{calculated} \le p_{limit} \\ p_{limit} & \text{if} \quad p_{calculated} \ge p_{limit} \end{cases} \tag{7.2}$$

The limiting pressure is given by $p_{limit} = n_{press} p_{ref}$, where p_{ref} is defined in Eq. (7.3).

$$p_{ref} = \frac{1}{2}\rho_\infty U_{tip}^2 \quad \text{where} \quad U_{tip} = 2\pi f \beta_0 R_{span} \tag{7.3}$$

The impact of the pressure limit on the aeroelastic calculations was examined using L1B1 and L3B1 in hover at $f = 10$ Hz and $f = 40$ Hz respectively. The flapping motion is described by the rotation vector given by Eq. (5.7) for $\beta_0 = 35°$ and simulations

were conducted using 300 time steps per flapping cycle. Based on the experiments described in Ref. [69], these cases are expected to have maximum aerodynamic loading at the corresponding frequencies. It is reasonable to assume that a pressure limit that is determined based on these cases would be adequate for the other configurations. The time averaged lift and thrust forces generated by the wings for various values of n_{press} are shown in Figures 7.1 and 7.2. The results clearly show that the aeroelastic forces are under-predicted if the pressure limit is not sufficiently high. Based on the trends obtained, the variation in mean lift and thrust is minor (difference < 15%) for $n_{press} \geq 30$. Therefore, n_{press} is fixed at 36 for all the simulations involving flexible wings undergoing simple flap motion.

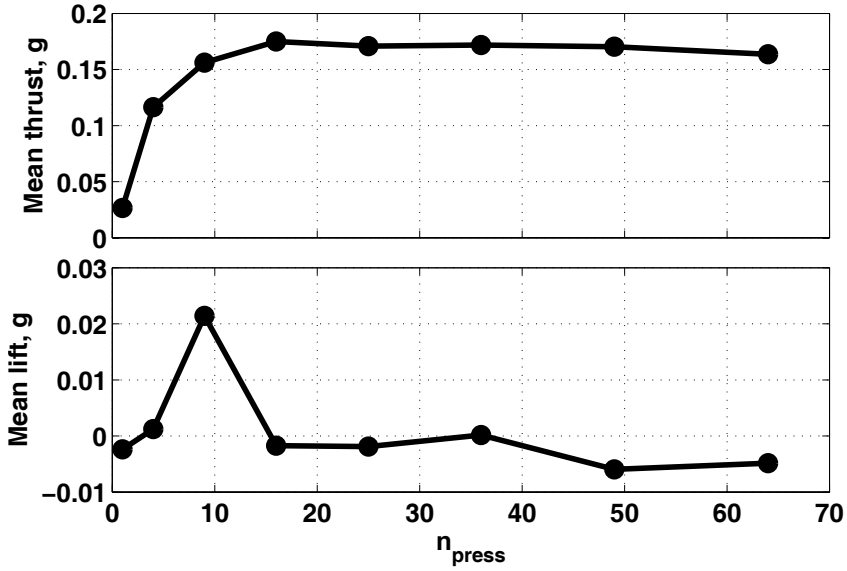

Figure 7.1: Mean forces generated for various pressure limits, L1B1 in hover at 10 Hz.

Simulations of rigid wings in forward flight, described in Section 6.3, indicate that the magnitude of maximum aerodynamic force is similar to that generated by wings in hover. This suggests that the maximum loading on the wings is similar. Therefore, it is assumed that a pressure limit that is suitable for wings in hover will also be adequate for wings in forward flight. This is verified by considering the case of L3B1

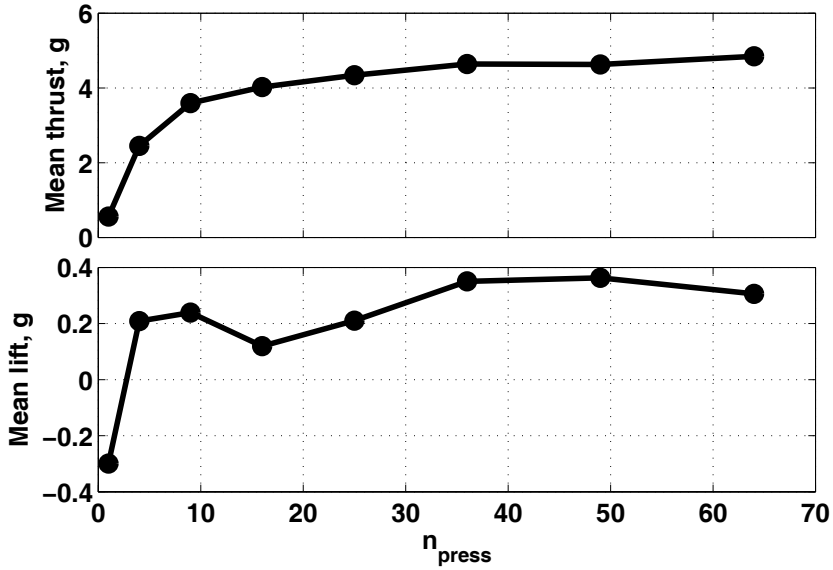

Figure 7.2: Mean forces generated for various pressure limits, L3B1 in hover at 40 Hz.

for $\beta_0 = 35°$, $f = 40$ hz, and $\mu = 0.25$. The time histories of the thrust and lift for 3 cycles, which were smoothed using filter in Table 6.1, are shown in Figure 7.3 and the mean quantities are listed in Table 7.2. Note that simulations for $n_{press} = 64$ and 100 terminated after the 3rd cycle due to excessive local deformation caused by the noise. Figure 7.3 indicates that the differences in the overall time histories for various values of n_{press} are similar. The maximum difference in the mean quantities is less than 15%, which is considered to be acceptable.

n_{press}	Mean lift, g	Mean thrust, g
36	-4.8994	5.2331
49	-4.2935	5.3998
64	-4.8973	5.7890
100	-4.3969	5.6732

Table 7.2: Mean lift and thrust generated by L3B1 for $\beta_0 = 35°$, f = 40 Hz, and $\mu = 0.25$, for various pressure limits.

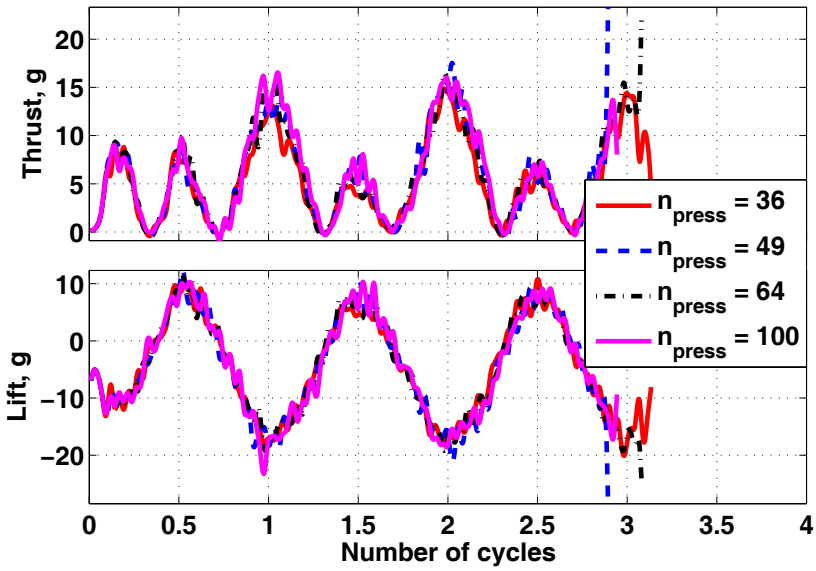

Figure 7.3: Time histories of lift and thrust generated by L3B1 for $\beta_0 = 35°$, f = 40 Hz, and $\mu = 0.25$, for various pressure limits.

Isotropic Flapping Wings in Hover

The lift and thrust generated by isotropic wings undergoing prescribed flapping motion are shown in Figures 7.4, 7.5, and 7.6. The flapping motion is given by the rotation vector in Eq (5.7) for $\beta_0 = 5°$ and $f = 10$ Hz. The wing thickness, density, and Poisson's ratio were 0.4mm, 2700 kg/m^3, and 0.3 respectively. In the simulations using the approximate model, 50 time steps per flapping cycle were used to discretize the motion. The CFD based results, presented in Ref. [82], were computed using the aeroelastic model that is described in Refs. [78, 79]. The lift and thrust were non-dimensionalized as indicated by Eq (6.8). The load signals obtained from the approximate model were smoothed using digital filters described in Table 6.5.

The results, shown in Figures 7.4, 7.5, and 7.6, indicate that the lift and thrust computed using the approximate aeroelastic model show reasonable agreement with the CFD based results for the cases considered. Note that a periodic or steady state solution was not observed for the case of $E = 0.1$ GPa. Therefore, an accurate

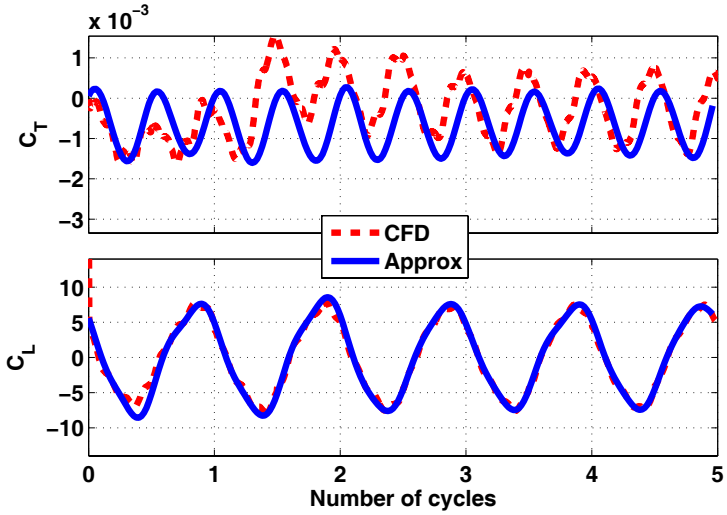

Figure 7.4: Force coefficients generated by isotropic wings undergoing prescribed flapping motion, $E = 70$ GPa

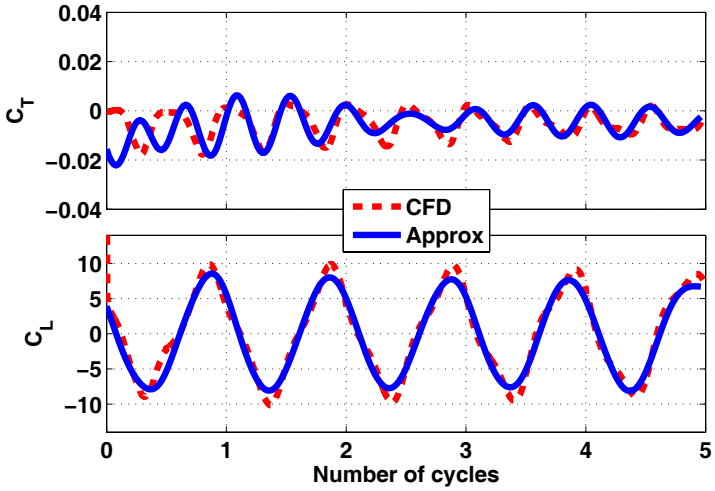

Figure 7.5: Force coefficients generated by isotropic wings undergoing prescribed flapping motion, $E = 10$ GPa

assessment of the differences between the CFD and approximate result is difficult for this case.

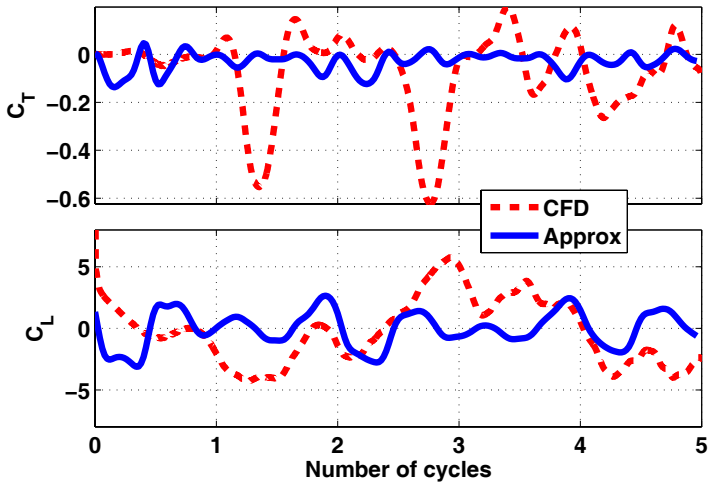

Figure 7.6: Force coefficients generated by isotropic wings undergoing prescribed flapping motion, $E = 0.1$ GPa

Anisotropic Flapping Wings in Hover

The computed and experimentally measured magnitudes of thrust generated by anisotropic wings are compared next. The results, obtained for $\beta_0 = 35^\circ$ for a range of flapping frequencies, are shown in Figures 7.7, 7.8, and 7.9 respectively. A relative comparison of thrust generated by one-layer batten configurations is shown in Figure 7.10. The experimental results were obtained from Ref. [69] and computations are based on the approximate aeroelastic model. Note that the experiments were conducted using two wings undergoing symmetric flapping motion, whereas the computations were performed by considering a single wing. Therefore, the thrust obtained from the simulations was multiplied by a factor of two to facilitate comparison with the experimental result. For the approximate model, 300 time steps per flapping cycle were used to discretize the motion. The simulations, conducted for a total of 5 cycles, indicated that an approximate steady state was achieved after two cycles.

Therefore, the mean thrust was calculated by time averaging the thrust generated over cycles 2 through 5.

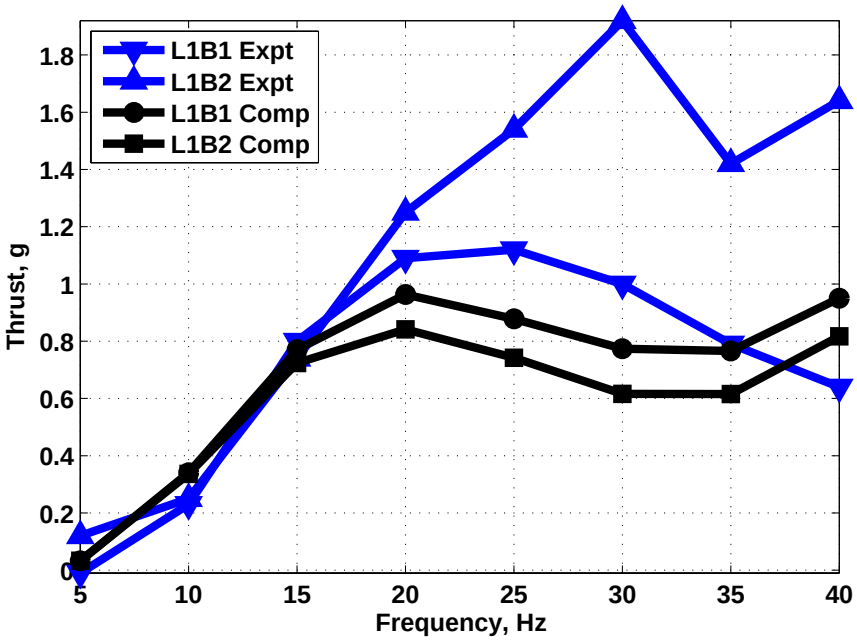

Figure 7.7: Comparison of thrust generated by L1B1 and L1B2: 'Expt' - Experiments [69], 'Comp' - computations, current study

The results show that the thrust obtained using the approximate aeroelastic model shows reasonable agreement with experimentally measured thrust for all the cases considered. This is somewhat surprising since the approximate aerodynamic model over-predicted peak lift generated by rigid wings for these combinations of flapping amplitude and frequencies. An accurate assessment of the error is difficult, since the limited amount of available experimental data does not provide any indication of the sensitivity of the thrust to variability in material and geometric properties and wing construction. Consequently, the impact of discrepancies in structural dynamic modeling on the thrust generated has to be examined before quantifying the differences in the aeroelastic results. It may also be assumed that the impact of wing flexibility on spanwise flow and tip vortices affects the discrepancy between the computational and experimental results.

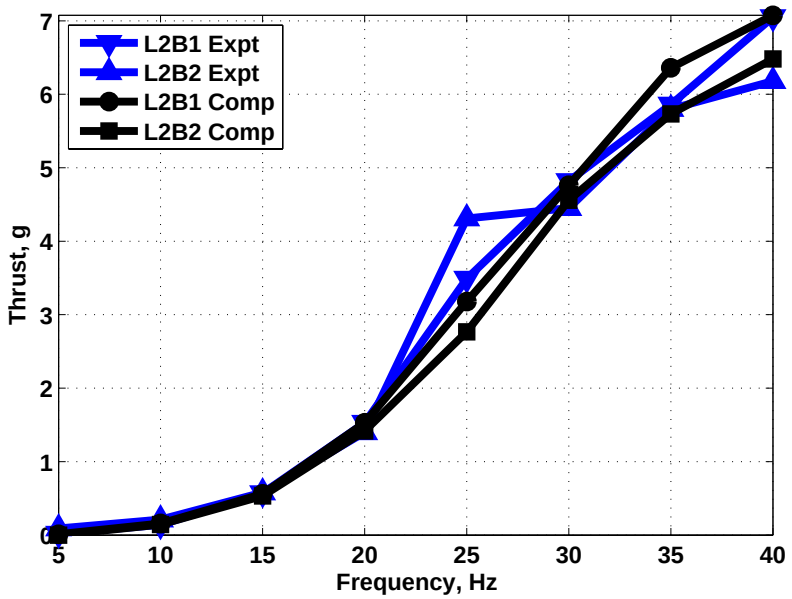

Figure 7.8: Comparison of thrust generated by L2B1 and L2B2: 'Expt' - Experiments [69], 'Comp' - computations, current study

Comparison of the thrust generated by the one and two layer batten configurations is shown in Figures 7.7, 7.8, and 7.9. The computational results indicate that the thrust generated reduces as the number of prepreg layers in the battens is increased. This may be due to the fact that reinforcing the battens increases the torsional stiffness of the wing thereby reducing the twist angle of the wing. Thus, the total force generated by the wing and its component normal to the stroke plane, i.e. thrust, are both reduced. This trend is not apparent from the experimental results.

Figure 7.10 shows the thrust generated by one-layer batten configurations. These results indicate that the approximate model predicts the trends that are observed from the experimental measurements. Different wing configurations produce maximum thrust for the range of flapping frequencies considered. The L1B1 configuration produces maximum thrust for frequencies between 5 Hz and 18 Hz, L2B1 for frequencies between 18 Hz and 35 Hz, and L3B1 for frequencies between 35 Hz and 40 Hz respectively.

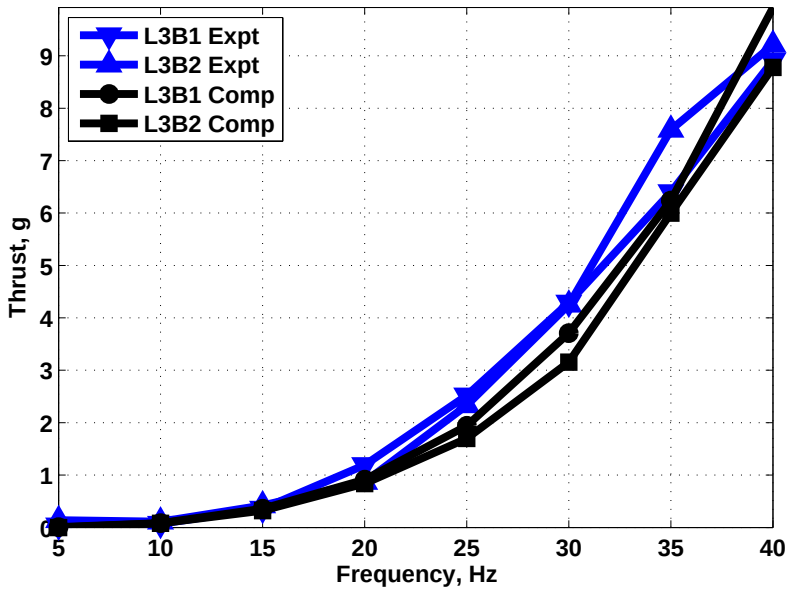

Figure 7.9: Comparison of thrust generated by L3B1 and L3B2: 'Expt' - Experiments [69], 'Comp' - computations, current study

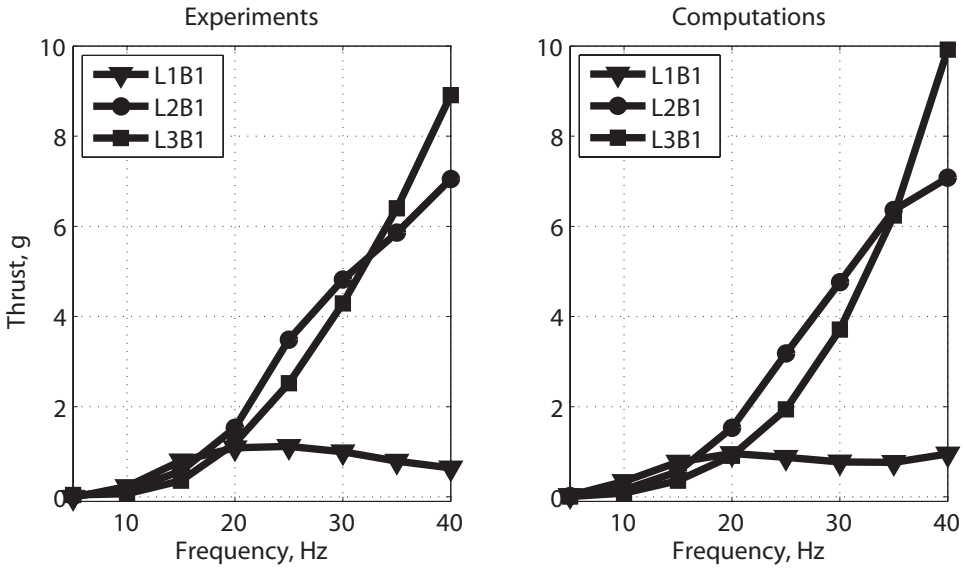

Figure 7.10: Thrust generated by one-layer batten configurations: Experiments [69], Computations - current study

The thrust generated by L1Bj configurations is shown in Figure 7.7. This result indicates that experimental measurements as well as the computations for L1B1 show a peak in thrust for a flapping frequency in the range of $20-25$ Hz. The computations for L1B2 show a similar peak. These peaks occur when the frequency of wing excitation is in the vicinity of the fundamental frequency of the wing. Additional simulations using L1B1 were conducted in order to examine the dependence of the peak in thrust on the flapping amplitude. The results, shown in Figure 7.11, indicate that a peak in thrust is obtained when the excitation frequency is close to the natural frequency of the wing for all the amplitudes considered. This is an important observation that is likely to guide subsequent efforts in wing design and selection of wing kinematics.

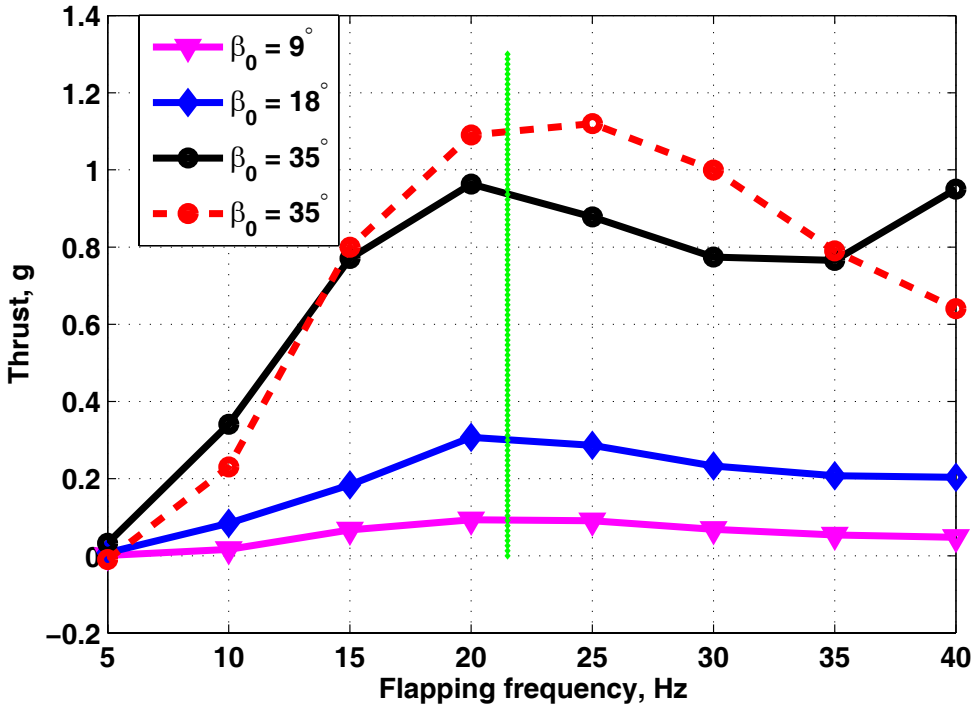

Figure 7.11: Thrust generated by L1B1 for various flapping amplitudes: Dashed line - Experiments [69], Solid lines - computations, current study. The vertical green line indicates the natural frequency of L1B1

The aerodynamic and inertia loads acting on the wings were compared. Comparisons for L1B1 for the range of frequencies considered are shown in Figure 7.12 and

7.13, where results obtained from the aeroelastic model were smoothed using the filter described in Table 6.1. The aerodynamic and inertia loads are calculated as give by Eq. (7.4). The results, which are representative of the comparisons obtained for other cases, indicate that the relative importance of inertia loads increases as flapping frequency increases, and the aerodynamic loads are comparable to inertia loads. This finding is contrary to the observations of Refs. [28, 29, 41], suggesting that the relative importance of aerodynamic to inertia loads is configuration dependent and wings that have excessive mass will produce inertia loads that will be dominant. Thus, this finding emphasizes the importance of correctly accounting for aeroelastic effects in flapping wings.

$$\mathbf{F}_{sp}\Big|_{aero} = \iint_{A_w} p\, \boldsymbol{dA}_{sp} \quad \text{and} \quad \mathbf{F}_{sp}\Big|_{inertia} = \iiint_{V_w} dm\, \ddot{\boldsymbol{x}}_{sp} \tag{7.4}$$

Wings undergoing insect-like kinematics for the case of hover

Results were obtained for rigid and flexible wings employing insect-like kinematics. The kinematics, based on the hover kinematics of hawkmoths [21], are obtained by scaling the stroke amplitudes by a factor of two. The time dependent Euler angles, prescribed about the Y_w, X_w, and Z_w axes respectively, are described by the rotation vectors in Eq. (7.5) and shown in Figure 7.14.

$$\boldsymbol{\psi}_{\Phi} = \Phi_r(t)\begin{Bmatrix} 0 \\ 1 \\ 0 \end{Bmatrix} \qquad \boldsymbol{\psi}_{\alpha} = \alpha_r(t)\begin{Bmatrix} 1 \\ 0 \\ 0 \end{Bmatrix} \qquad \boldsymbol{\psi}_{\Theta} = \Theta_r(t)\begin{Bmatrix} 0 \\ 0 \\ 1 \end{Bmatrix} \tag{7.5}$$

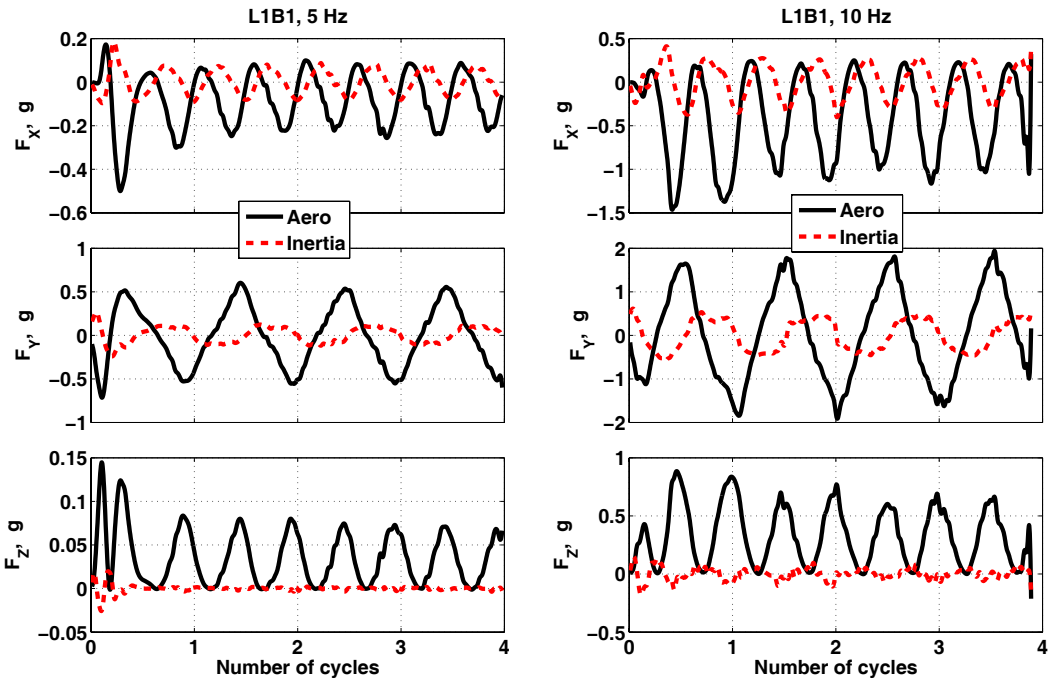

(a) f = 5 Hz (b) f = 10 hz

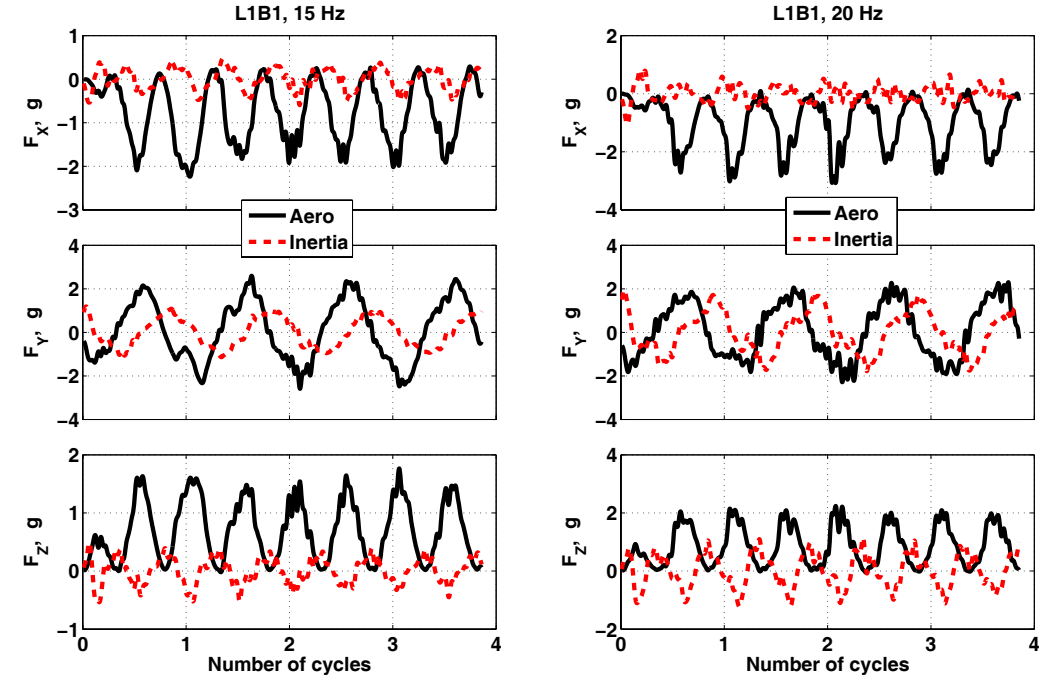

(c) f = 15 Hz (d) f = 20 hz

Figure 7.12: Aerodynamic and inertia loads acting on L1B1 in hover: $\beta_0 = 35°$, f = 5 Hz to 20 hz

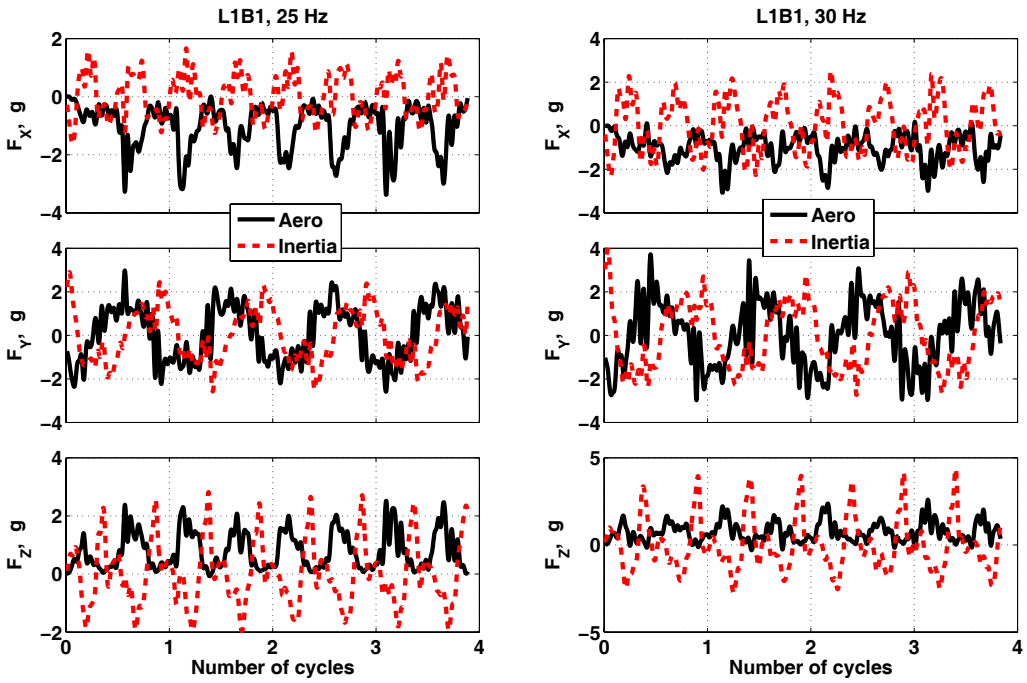

(a) f = 25 Hz (b) f = 30 hz

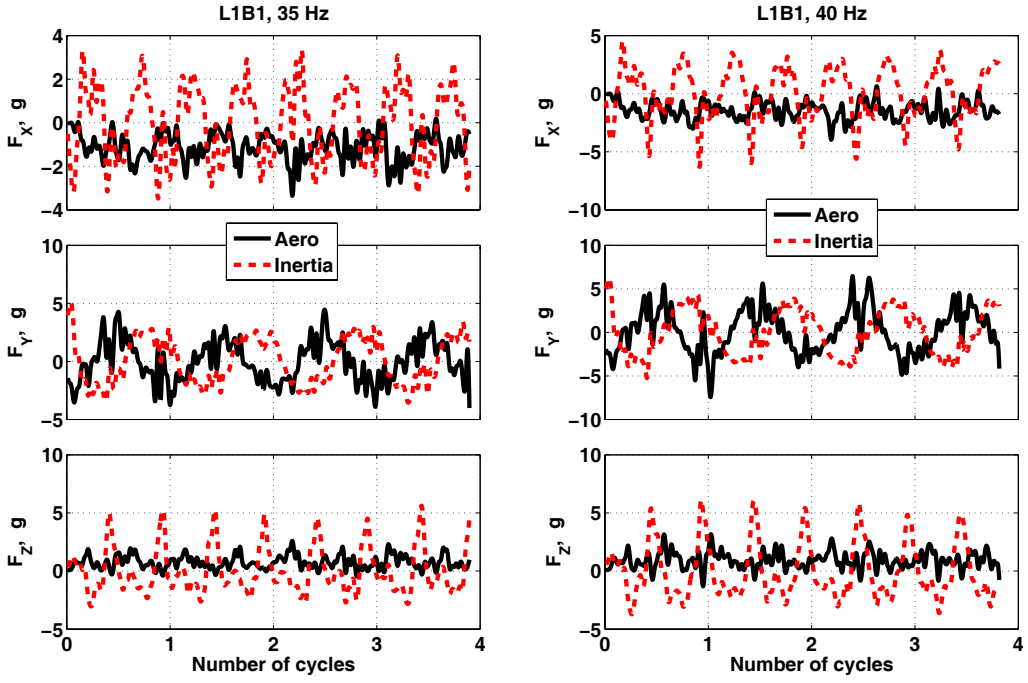

(c) f = 35 Hz (d) f = 40 hz

Figure 7.13: Aerodynamic and inertia loads acting on L1B1 in hover: $\beta_0 = 35°$, f = 25 Hz to 40 hz

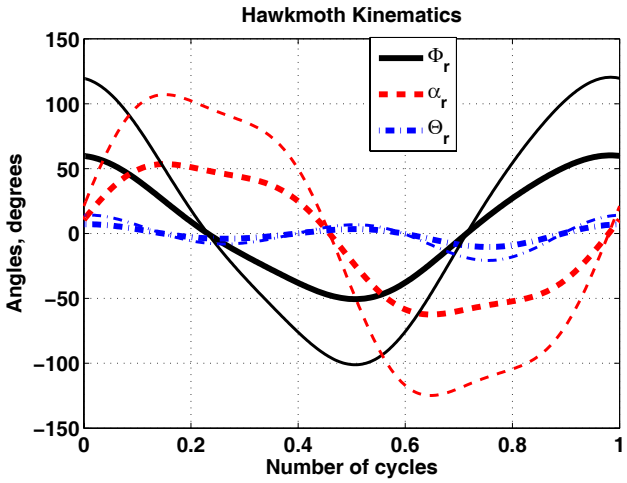

Figure 7.14: Hawkmoth kinematics: thin lines denote actual kinematics [21]; thick lines denote scaled kinematics that are used in the current study.

where

$$\begin{aligned}
\Phi_r(t) &= \frac{\Phi_0}{4} + \frac{1}{2}\sum_{j=0}^{3}\left[\Phi_{cj}\cos(2\pi jft) + \Phi_{sj}\sin(2\pi jft)\right] \\
\alpha_r(t) &= -\frac{\alpha_0}{4} - \frac{1}{2}\sum_{j=0}^{3}\left[\alpha_{cj}\cos(2\pi jft) + \alpha_{sj}\sin(2\pi jft)\right] \\
\Theta_r(t) &= \frac{\Theta_0}{4} + \frac{1}{2}\sum_{j=0}^{3}\left[\Theta_{cj}\cos(2\pi jft) + \Theta_{sj}\sin(2\pi jft)\right]
\end{aligned} \tag{7.6}$$

where α_{r1} and Θ_r are prescribed about the quarter-chord point at the root. The Fourier coefficients of the Euler angles are given in Table 7.3. The simulations were conducted using 300 time steps per flapping cycle, and the results obtained from the aeroelastic model were smoothed using a filter described by Table 6.3. The pressure limit used for this case is computed using $n_{press} = 36$ and $\beta_0 = 60^\circ$ in Eq. (7.3); this value of β_0 is expected to yield a conservative limit.

The lift and thrust, in grams, generated by rigid and anisotropic wings for $f = 10$ Hz, and $f = 20$ Hz, are shown in Figure 7.15. The results correspond to the forces generated by an isolated flapping wing. For $f = 10$ Hz, L1B1 generates higher thrust compared to the other wings, as shown in Figure 7.15(a). However, the lift generated

Φ_0	Φ_{c1}	Φ_{c2}	Φ_{c3}	Φ_{s1}	Φ_{s2}	Φ_{s3}
8.1074	52.9298	0.5959	2.2231	-6.9385	-2.6643	1.5011

Θ_0	Θ_{c1}	Θ_{c2}	Θ_{c3}	Θ_{s1}	Θ_{s2}	Θ_{s3}
-1.9395	1.4152	6.1994	0.4469	2.4752	0.5730	-0.7162

α_0	α_{c1}	α_{c2}	α_{c3}	α_{s1}	α_{s2}	α_{s3}
9.6698	-14.9886	0.5099	-0.9282	-58.9230	-0.2521	-7.6834

Table 7.3: Fourier coefficients in the hawkmoth kinematics (in degrees).

by all the configurations is somewhat similar. For $f = 20$ Hz the results in Figure 7.15(b) indicate that L1B1 generates less thrust and lift when compared to L3B1 and the rigid wing, whereas L3B1 produces the maximum thrust. Recall that for this frequency, the L1B1 and L3B1 configurations generated the maximum and minimum thrust when using a simple flap actuation. This implies that the impact of wing flexibility is kinematics dependent.

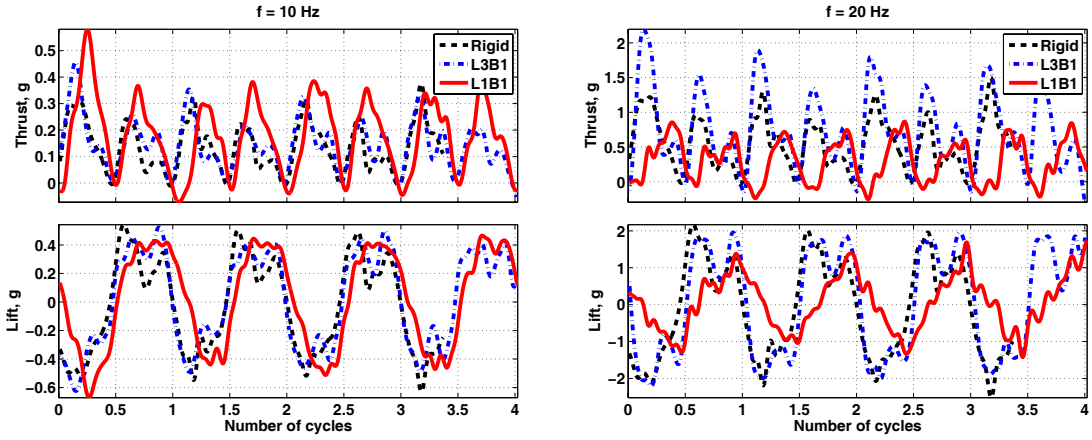

(a) (b)

Figure 7.15: Lift and thrust generated by rigid and flexible wings undergoing scaled hawkmoth kinematics

7.3 Flexible Flapping Wings in Forward Flight

The effect of forward flight on the aerodynamic forces generated by flexible wings was examined using anisotropic wings undergoing prescribed flap motion for a range of forward flight conditions. The results, shown in Figures 7.16, 7.16, 7.18, and 7.19, were obtained for L1B1 and L3B1, $\beta_0 = 35°$, $f = \{10, 40\}$ Hz, and forward flight conditions corresponding to the values given in Table 6.8. The flapping motion is given by Eq. (5.7) and the magnitude of the free stream velocities was determined based on the tip speed of a rigid wing undergoing the same kinematics. The mean forces were obtained by time averaging the transient forces over cycles 2 through 5. The mean forces computed for one wing were multiplied by a factor of two so as to approximate the force generated by a vehicle that has a pair of wings.

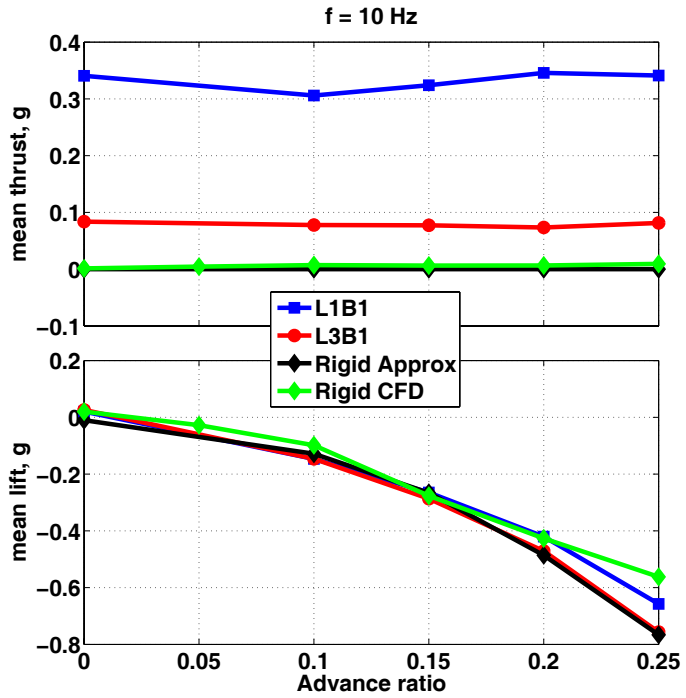

Figure 7.16: Mean lift and thrust, in grams, generated by rigid and flexible wings

The mean lift and thrust generated by rigid and flexible wings are shown in Figures 7.16 and 7.16. The results indicate that the lift decreases (becomes more

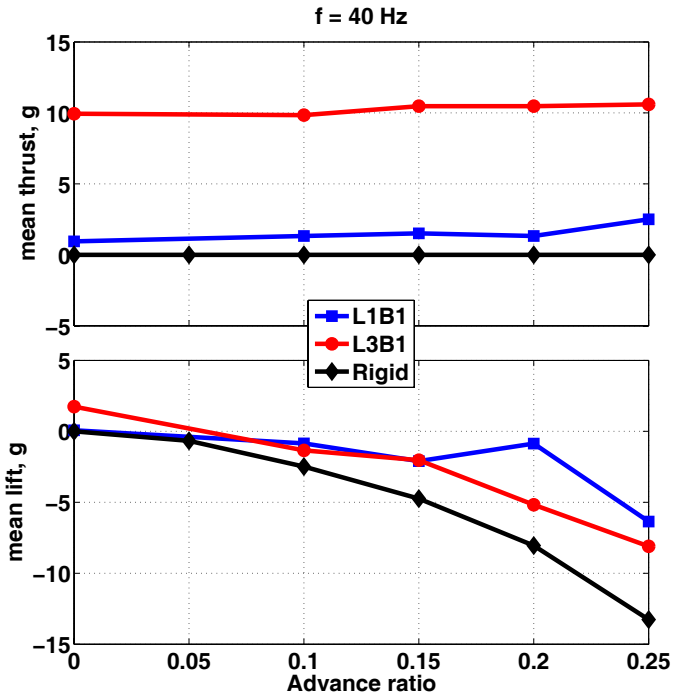

Figure 7.17: Mean lift and thrust, in grams, generated by rigid and flexible wings

negative) with increase in forward flight speed. However, the change in thrust is somewhat small. Furthermore, different wings produce maximum mean thrust at different frequencies: L1B1 produces maximum thrust at $f = 10$ Hz, whereas L3B1 produces the maximum thrust at $f = 40$ Hz. Similar trends were obtained for the case of hover.

The mean horizontal and vertical forces generated by the wings, indicative of the propulsive and payload capacity of the wings, are shown in Figures 7.18 and 7.19. The horizontal and vertical directions are shown in Figure 1.3. Note that both F_h and F_v are positive in an actual vehicle; a negative value of F_h denotes drag. The results show that F_v increases and F_h decreases with increase in forward flight speed, and wing flexibility has a beneficial influence. The flexible configurations have higher payload capacity and lower drag than rigid wings. Configurations L1B1 and L3B1 have the largest payload capacity and least drag at 10 Hz and 40 Hz respectively. These results indicate that the trends in force generation obtained for wings in hover

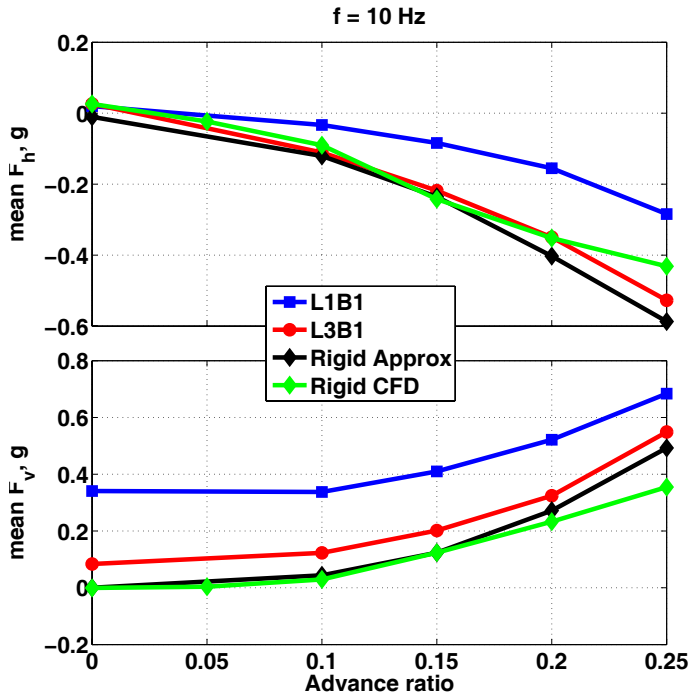

Figure 7.18: Mean horizontal and vertical forces, in grams, generated by rigid and flexible wings

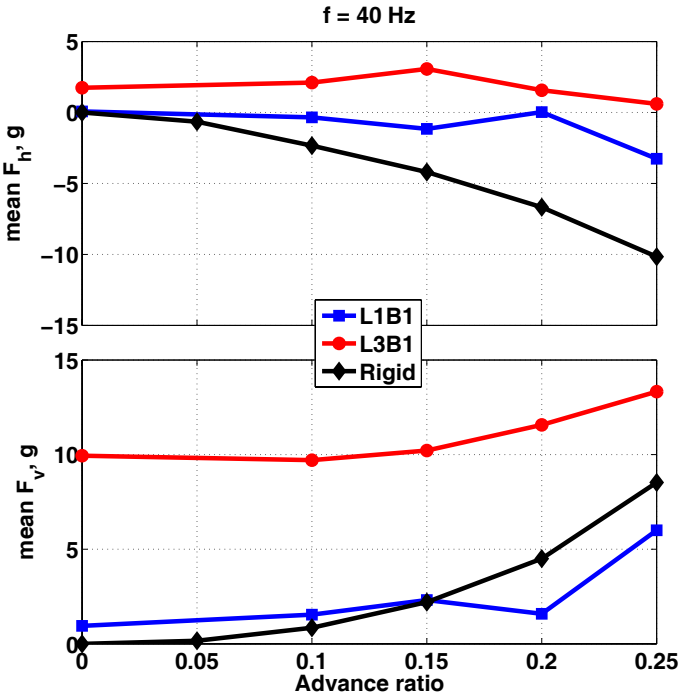

Figure 7.19: Mean horizontal and vertical forces, in grams, generated by rigid and flexible wings

also apply to forward flight.

Of the various wings and flapping frequencies considered in this study, positive values of both F_h and F_v were obtained only in the case of L3B1 at $f = 40$ Hz, as shown in Figure 7.19. Thus, this case seems to be the most effective combination of wing flexibility and kinematics encountered in this study. The payload capacity for this case, which is 12 grams, is inadequate to support the expected weight of a potential vehicle (approximately 50 grams). This implies that further exploration of the parameter space is needed. Note that typical insect kinematics include a large pitching motion during and at the ends of each flapping stroke. In the current study the wing pitch was due to wing torsion. Therefore, the interaction of wing flexibility and kinematics that include active pitching of the wing has to be explored in greater detail.

CHAPTER VIII

Conclusions and Future Work

An approximate aeroelastic model suitable for representing the behavior of flexible anisotropic flapping wings in hover and forward flight has been developed. The structural dynamic component of this flapping wing aeroelastic problem was modeled using MSC MARC, a commercially available nonlinear finite element package, and the aerodynamic loads were computed from an approximate aerodynamic model. The capability of the MARC code for modeling anisotropic bio-inspired flapping wings was carefully tested and found to be adequate. The approximate aerodynamic model, originally developed for rigid wings in hover, was modified to incorporate wing flexibility and forward flight. The effect of viscosity was also incorporated in an approximate manner by including the temporal decay of circulation once a vortex is shed into the wake. The results presented include validation studies conducted on the structural dynamic models, aerodynamic studies using rigid airfoils and wings in hover and forward flight, and aeroelastic studies on isotropic and anisotropic wings in hover and forward flight. The conclusions obtained from these studies are presented next.

8.1 Principal conclusions

Based on detailed structural dynamic studies that involved implementation of wing kinematics in MARC, modeling the centrifugal stiffening effect of an accelerating

plate, tensile tests conducted on thin films (membrane), a comparison of mode shapes, frequencies, and tip displacements in vacuum, for several anisotropic Zimmerman wings, one can conclude that,

1. Two dimensional rotations can be implemented in MARC either as rotation vectors or displacements. However, 3D rotations, which are representative of insect-like kinematics, have to be implemented as displacement boundary conditions.

2. Comparisons obtained for an accelerating plate show that MARC captures the centrifugal stiffening effect, which may be important in flapping wings, in an accurate manner.

3. Tensile tests show that paint, which is used to facilitate visual tracking of translucent membranes, has very little effect on the geometric and stiffness properties of thin films. However, a 16% increase in density is noted, implying that the impact of paint on the mass distribution and inertia properties of membrane based wings cannot be neglected.

4. Comparisons of mode shapes and frequencies indicate that the finite element wing models developed in this study show reasonable correlation (error $\leq 20\%$ in frequencies) with experimentally measured mode shapes and frequencies for all the configurations considered. However it is noted that the experiments were conducted in air which implies that the measured frequencies correspond to aeroelastic modes and not free vibration modes. The tip displacements obtained for wings flapping in vacuum show that the FE model correlates reasonably well with experiments.

Aerodynamic comparisons and trend studies were conducted for rigid airfoils and Zimmerman wings in hover and forward flight; the principal conclusions were:

1. The approximate unsteady aerodynamic loads show reasonable agreement with CFD based results for all the cases considered.

2. The unsteady Bernoulli equation and the vortex impulse method predict identical forces normal to the airfoil chord, but differ in forces that are parallel to the airfoil chord. Both approaches show reasonable correlation with CFD based computations.

3. Results for airfoils operating at low Reynolds number ($Re = 100$) show that incorporating the effect of viscosity in the approximate model improves correlation with CFD based results. When the vortical activity from the LE is strong, assuming separated flow in the approximate model is likely to yield reasonable agreement with CFD based loads. When the vortical activity from the LE is weak, approximate loads computed by assuming attached flow are likely to correlate better with CFD based results compared to those computed by assuming separated flow. However, the vorticity shed from the LE may have a significant effect on the unsteady loads during some portions of the flapping cycle.

4. Comparisons of forces generated by rigid Zimmerman wings in hover and forward flight, for a variety of wing kinematics, shows that the approximate model captures the important trends accurately. Results also indicate that the forces generated by rigid wings are insensitive to Reynolds number for the range considered in this study ($626 \leq Re \leq 17551$) and scale with the square of the flapping frequency.

Transient and time-averaged forces computed from the approximate aeroelastic model were compared with those obtained from CFD based computations using isotropic wings in hover as well as experiments conducted on several anisotropic wing configurations in hover. Trends for the mean forces were obtained for rigid and flexible wings in forward flight. Principal conclusions are:

1. High frequency large amplitude noise is an important consideration in aeroelastic simulations that employ a discrete vortex representation of the airfoil and the wake to compute the unsteady loads. The noise needs to be eliminated or reduced before the aerodynamic loads can be imposed on a flexible structure. In the current study, pressure based filters were used to limit the amplitude of noise.

2. The approximate model shows reasonable agreement with CFD based computations and experimental measurements for all the cases considered, and it predicts important trends in forces accurately. Therefore, this tool may be used to conduct trend studies on flapping wings.

3. For anisotropic wings in hover undergoing pure flapping motion, a peak in thrust was obtained when the actuation frequency was close to the natural frequency of the wing, and the location of the peak appears to be independent of the flapping amplitude. The choice of the 'best' flexible configuration was found to depend on the flapping frequency considered.

4. Increasing torsional stiffness reduces the thrust generated by the anisotropic wings in hover due to a reduction in the pitch angle caused by wing twist; this trend was not evident from the experiments.

5. The aerodynamic loads acting on the wings were found to be comparable to inertia loads. This is contrary to what was found in previous studies [28–30], which noted that aerodynamic loads are negligible compared to inertia loads. Therefore, it appears that the relative importance of aerodynamic and inertia loads in flapping wings is dependent on the configurations considered.

6. The payload capacity and propulsive capability of rigid and flexible wings in hover and forward flight were examined. It was found that flexible wings have larger payload capacity and lower drag compared to rigid wings. Also, different

flexible configurations perform better at different flapping frequencies; similar trends were noted in hover.

7. Results for rigid and flexible wings undergoing insect-like kinematics suggest that the choice of the 'best' flexible configuration also depend on the kinematics used in addition to the flapping frequency.

8.2 Recommendations for future work

With its current capabilities, the aeroelastic code developed in this dissertation may be used to explore the parameter space and identify scaling laws that are likely to guide the design of efficient flapping structures. The large parameter space associated with flapping wings implies that continued exploration is needed not only to understand the underlying physics but also to identify modifications and enhancements that will improve the predictive capabilities of approximate tools. Some recommendations are provided next:

1. Simulations of insect wings using CFD based tools indicate that spanwise flow and tip vortices may be important depending on the interplay between wing planform and kinematics. The approximate aerodynamic formulation is 2D and does not model these effects. Therefore, modifications to incorporate these effects into the formulation without an undue increase in computational expense should be pursued.

2. Comparisons for rigid airfoils demonstrate that vorticity shed from the LE may have a significant contribution to the loads only during some parts of the flapping cycle. Examples that are of practical interest include insects in forward flight wherein prominent LEVs were observed during the downstroke and only some portions of the upstroke. Accurate aerodynamic analysis of these situations would have to capture the effect of intermittent separation and re-attachment.

The approximate aerodynamic formulation is based on potential flow and therefore requires a physics based separation and re-attachment criterion that allows switching between the separated and attached flow assumptions. A useful starting point is to examine separation and re-attachment criteria that are used to model the effect of dynamic stall on helicopter blades.

3. The shed wake geometry for wings in hover and forward flight has been approximated using a normal cylindrical surface. Such an approximation appears to be reasonable for the cases considered in this thesis. However, for the general case the shed wake is typically not confined to the normal cylinder and a more realistic representation of wake geometry may have to be considered.

4. The effect of spanwise and chordwise deformations were incorporated into the aerodynamic formulation in an averaged manner. Although it appears that chordwise flexibility did not have a significant effect on the unsteady loads generated by the wings for the cases considered, a better approach to incorporate airfoil velocities is desired. For example, the chordwise velocities could be approximated as a Fourier series expansion and incorporated into the expression of quasi-steady vorticity.

5. The numerical noise that arises due to the discrete representation of the vorticity has to be reduced/eliminated in a more systematic manner. One may consider using digital filters for each spanwise station or borrow ideas from studies that use a modal representation of the structure. In the former, appropriate filters may be have to be designed on case by case basis. In the latter, the filter is determined based on the number of mode shapes used to approximate the pressure distribution.

APPENDICES

Appendix A: Incorporating Chordwise Flexibility

Derivation of Terms Incorporating Chordwise Flexibility

$$\Delta v_\theta(\theta,t)\big|_{us}^{flex} = \frac{-1}{2\pi}\oint_0^{2\pi}(\underline{A}\Delta v_\xi^{flex}+\underline{B}\Delta v_\eta^{flex})\cot\left(\frac{\varsigma-\theta}{2}\right)d\varsigma \tag{A.1}$$

Assume that Δv_ξ^{flex} and Δv_η^{flex} are independent of the coordinate θ. Then,

$$\Delta v_\theta(\theta,t)\big|_{us}^{flex} = \frac{-1}{2\pi}\left\{\left[\oint_0^{2\pi}\underline{A}\cot\left(\frac{\varsigma-\theta}{2}\right)d\varsigma\right]\Delta v_\xi^{flex}+\left[\oint_0^{2\pi}\underline{B}\cot\left(\frac{\varsigma-\theta}{2}\right)d\varsigma\right]\Delta v_\eta^{flex}\right\} \tag{A.2}$$

Substituting Eqs. (3.17) and (A.7) into Eq. (A.2) and simplifying, one has

$$\begin{aligned}
\oint_0^{2\pi}\underline{A}\cot\left(\frac{\varsigma-\theta}{2}\right)d\varsigma &= \underline{\tau}\left[I_{c,1}(\theta)-I_{c,2}(\theta)\right]-\underline{\sigma}\left[I_{s,1}(\theta)-I_{s,2}(\theta)\right]\\
\oint_0^{2\pi}\underline{B}\cot\left(\frac{\varsigma-\theta}{2}\right)d\varsigma &= 2I_{s,1}(\theta)-\underline{\tau}\left[I_{s,1}(\theta)-I_{s,2}(\theta)\right]-\underline{\sigma}\left[I_{c,1}(\theta)-I_{c,2}(\theta)\right]
\end{aligned} \tag{A.3}$$

where, the general form of $I_{s,j}$ and $I_{c,j}$ are given in Eq. (A.6). Substituting the results obtained in Eq. (A.10) into Eq. (A.3), one has

$$\begin{aligned}
-\frac{1}{2\pi}\oint_0^{2\pi}\left(\underline{A}\cot\left(\frac{\varsigma-\theta}{2}\right)\right)d\varsigma &= \underline{\tau}\left(\sin\theta-\sin 2\theta\right)+\underline{\sigma}\left(\cos\theta-\cos 2\theta\right)\\
-\frac{1}{2\pi}\oint_0^{2\pi}\left(\underline{B}\cot\left(\frac{\varsigma-\theta}{2}\right)\right)d\varsigma &= -2\cos\theta+\underline{\tau}\left(\cos\theta-\cos 2\theta\right)-\underline{\sigma}\left(\sin\theta-\sin 2\theta\right)
\end{aligned} \tag{A.4}$$

Therefore,

$$\Delta v_\theta(\theta,t)\big|_{us}^{flex} = \Big[\underline{\tau}\big(\sin\theta - \sin 2\theta\big) + \underline{\sigma}\big(\cos\theta - \cos 2\theta\big)\Big]\Delta v_\xi^{flex} + \Big[-2\cos\theta + \underline{\tau}\big(\cos\theta - \cos 2\theta\big) - \underline{\sigma}\big(\sin\theta - \sin 2\theta\big)\Big]\Delta v_\eta^{flex} \tag{A.5}$$

Evaluating $I_{s,j}$ and $I_{c,j}$

Note that

$$I_{s,j}(\theta) = \oint_0^{2\pi} \sin j\varsigma \cot\left(\frac{\varsigma-\theta}{2}\right) d\varsigma$$
$$I_{c,j}(\theta) = \oint_0^{2\pi} \cos j\varsigma \cot\left(\frac{\varsigma-\theta}{2}\right) d\varsigma \tag{A.6}$$

where, j is a non-negative integer, and

$$\cot\left(\frac{\varsigma-\theta}{2}\right) = \frac{\sin\varsigma + \sin\theta}{\cos\theta - \cos\varsigma} \tag{A.7}$$

Substituting Eq. (A.7) into (A.6), one obtains

$$I_{s,j}(\theta) = \frac{1}{2}\oint_0^{2\pi} \frac{\cos(j-1)\varsigma - \cos(j+1)\varsigma}{\cos\theta - \cos\varsigma} d\varsigma + \oint_0^{2\pi} \frac{\sin j\varsigma \sin\theta}{\cos\theta - \cos\varsigma} d\varsigma$$
$$I_{c,j}(\theta) = \frac{1}{2}\oint_0^{2\pi} \frac{\sin(j+1)\varsigma - \sin(j-1)\varsigma}{\cos\theta - \cos\varsigma} d\varsigma + \oint_0^{2\pi} \frac{\cos j\varsigma \sin\theta}{\cos\theta - \cos\varsigma} d\varsigma \tag{A.8}$$

Using the results in Eqs. (A.12) and (A.13), one has

$$\oint_0^{2\pi} \frac{\cos j\varsigma}{\cos\theta - \cos\varsigma} d\varsigma = -2\pi \frac{\sin j\theta}{\sin\theta} \quad \text{and} \quad \oint_0^{2\pi} \frac{\sin j\varsigma}{\cos\theta - \cos\varsigma} d\varsigma = 0 \tag{A.9}$$

Substituting Eq. (A.9) into (A.8)

$$I_{s,j}(\theta) = \frac{1}{2}\left[-2\pi \frac{\sin(j-1)\theta}{\sin\theta} + 2\pi \frac{\sin(j+1)\theta}{\sin\theta}\right] = 2\pi \cos j\theta$$
$$I_{c,j}(\theta) = -2\pi \sin j\theta \tag{A.10}$$

Glauert Integrals

The Glauert integrals of interest are

$$I_{GLC} = \oint_0^{2\pi} \frac{\cos j\varsigma}{\cos\theta - \cos\varsigma} d\varsigma \quad \text{and} \quad I_{GLS} = \oint_0^{2\pi} \frac{\sin j\varsigma}{\cos\theta - \cos\varsigma} d\varsigma \tag{A.11}$$

for $j = 0, 1, 2, \cdots$. I_{GLC} may be simplified as follows:

$$\oint_0^{2\pi} \frac{\cos j\varsigma}{\cos\theta - \cos\varsigma} d\varsigma = \int_0^{\pi} \frac{\cos j\varsigma}{\cos\theta - \cos\varsigma} d\varsigma + \int_{\pi}^{2\pi} \frac{\cos j\varsigma}{\cos\theta - \cos\varsigma} d\varsigma$$

Consider the second integral. Change variable of integration from ς to ϕ where $\phi = 2\pi - \varsigma$. Then

$$\int_{\pi}^{2\pi} \frac{\cos j\varsigma}{\cos\theta - \cos\varsigma} d\varsigma = -\int_{\pi}^{0} \frac{\cos(2\pi j - j\phi)}{\cos\theta - \cos(2\pi - \phi)} d\phi$$
$$= -\int_{\pi}^{0} \frac{\cos j\phi}{\cos\theta - \cos\phi} d\phi$$
$$= \int_{0}^{\pi} \frac{\cos j\phi}{\cos\theta - \cos\phi} d\phi$$

Therefore

$$\int_{0}^{2\pi} \frac{\cos j\varsigma}{\cos\theta - \cos\varsigma} d\varsigma = 2\int_{0}^{\pi} \frac{\cos j\phi}{\cos\theta - \cos\phi} d\phi$$

From Appendix E, pp. 624, of Ref. [92], note that

$$\int_{0}^{\pi} \frac{\cos j\phi}{\cos\theta - \cos\phi} d\phi = -\pi \frac{\sin j\theta}{\sin\theta}$$

Therefore

$$I_{GLC} = 2\int_{0}^{\pi} \frac{\cos j\phi}{\cos\theta - \cos\phi} d\phi = -2\pi \frac{\sin j\theta}{\sin\theta} \tag{A.12}$$

Similarly, I_{GLS} may be modified as

$$\oint_{0}^{2\pi} \frac{\sin j\varsigma}{\cos\theta - \cos\varsigma} d\varsigma = \int_{0}^{\pi} \frac{\sin j\varsigma}{\cos\theta - \cos\varsigma} d\varsigma + \int_{\pi}^{2\pi} \frac{\sin j\varsigma}{\cos\theta - \cos\varsigma} d\varsigma$$

Consider the second integral. Change variable of integration from ς to ϕ where $\phi = 2\pi - \varsigma$. Then

$$\int_{\pi}^{2\pi} \frac{\sin j\varsigma}{\cos\theta - \cos\varsigma} d\varsigma = -\int_{\pi}^{0} \frac{\sin(2\pi j - j\phi)}{\cos\theta - \cos(2\pi - \phi)} d\phi$$

$$= -\int_{\pi}^{0} \frac{-\sin j\phi}{\cos\theta - \cos\phi} d\phi$$

$$= -\int_{0}^{\pi} \frac{\sin j\phi}{\cos\theta - \cos\phi} d\phi$$

Therefore

$$I_{GLS} = \int_{0}^{2\pi} \frac{\sin j\varsigma}{\cos\theta - \cos\varsigma} d\varsigma = 0 \tag{A.13}$$

Appendix B: Unsteady Loads

The unsteady aerodynamic loads are computed using either the vortex impulse method or the unsteady Bernoulli equation, where both approaches are derived from the irrotational form of the Euler equations (Chapters 9 and 10, Ref. [92]). The vortex impulse method yields directly the integrated force and moment on the airfoil; therefore, this approach is more suitable for aerodynamic calculations involving rigid wings or aeroelastic calculations involving beam-type structural dynamic models. The unsteady Bernoulli equation is computationally more expensive and yields the pressure distribution on the airfoil; therefore, this approach is used when chordwise distribution of aerodynamic loads are of interest. The two approaches are equivalent; however, important differences during implementation due to assumptions on the geometry of the airfoil. This appendix summarizes the derivations of the two approaches.

Derivation of the Unsteady Bernoulli Equation

From Ref [109], the Newton's second law of motion or the law of conservation of momentum gives

$$\frac{D\boldsymbol{q}}{Dt} = \boldsymbol{f} - \frac{\boldsymbol{\nabla} p}{\rho} \tag{B.1}$$

where, $\boldsymbol{f}$ denotes body force per unit volume. Equation (B.1) gives [1]

$$\frac{\partial \boldsymbol{q}}{\partial t} + (\boldsymbol{q} \cdot \boldsymbol{\nabla})\,\boldsymbol{q} = \boldsymbol{f} - \frac{\boldsymbol{\nabla} p}{\rho} \tag{B.2}$$

The second term on the left hand side of the above equation can be written as

$$\boldsymbol{q} \cdot \nabla \boldsymbol{q} = \boldsymbol{\nabla}\left(\frac{q^2}{2}\right) - \boldsymbol{q} \times (\boldsymbol{\nabla} \times \boldsymbol{q}) \tag{B.3}$$

[1] The following derivation is taken from Refs [97, 109]

Substituting this into Eq (B.2), we obtain

$$\frac{\partial \boldsymbol{q}}{\partial t} + \nabla\left(\frac{q^2}{2}\right) - \boldsymbol{q} \times (\nabla \times \boldsymbol{q}) = \boldsymbol{f} - \frac{\nabla p}{\rho} \tag{B.4}$$

For irrotational flow, $\nabla \times \boldsymbol{q} = 0$. Therefore, Eq (B.4) yields

$$\frac{\partial \boldsymbol{q}}{\partial t} + \nabla\left(\frac{q^2}{2}\right) = \boldsymbol{f} - \frac{\nabla p}{\rho} \tag{B.5}$$

Assume body force is conservative, i.e. $\boldsymbol{f} = -\nabla E$, and note $\boldsymbol{q} = \nabla\phi$, then Eq (B.5) implies

$$\begin{aligned} \nabla\frac{\partial \phi}{\partial t} + \nabla\frac{q^2}{2} &= -\nabla E - \nabla\frac{p}{\rho} \\ \Rightarrow \nabla\left[\frac{\partial \phi}{\partial t} + \frac{q^2}{2} + E + \frac{p}{\rho_\infty}\right] &= 0 \end{aligned} \tag{B.6}$$

Therefore

$$\frac{\partial \phi}{\partial t} + \frac{q^2}{2} + E + \frac{p}{\rho} = C(t) \tag{B.7}$$

Where, $C(t)$ denotes an arbitrary function of time. For a reference condition $E_\infty = 0$, $\phi_\infty = const$, $\boldsymbol{q}_\infty = 0$, we obtain

$$\frac{p_\infty - p}{\rho} = \frac{\partial \phi}{\partial t} + \frac{q^2}{2} + E \tag{B.8}$$

This is the expression for the unsteady Bernoulli equation.

Derivation of the Vortex Impulse Method

The instantaneous state of an irrotational ideal fluid, or a change in such a state, may be interpreted as brought out suddenly or impulsively, and the set of forces producing them are known as impulsive forces (Ch. 9, Ref. [92], pp. 245-249). Following Ref. [92] one obtains

$$\phi = \chi - \frac{\varpi}{\rho} \tag{B.9}$$

where ϕ is the velocity potential, ϖ is known as the impulsive pressure, and χ is the potential of the impulse of body forces. Thus the velocity potential is the potential of the impulse. In the absence of body forces, $\chi = 0$ and the impulsive pressure is given by

$$\varpi = -\rho\phi \tag{B.10}$$

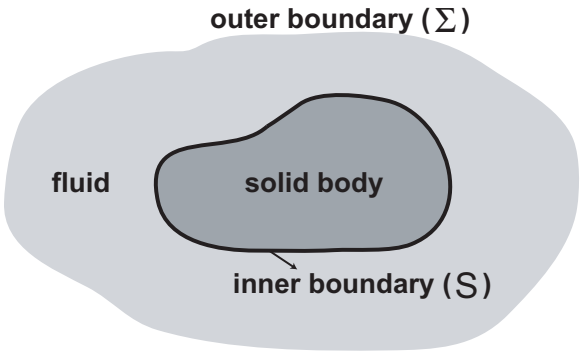

Figure B.1: Outer and inner boundaries of a solid immersed in a fluid

The force and moment applied by the body on the fluid are equal to the time derivatives of the impulses; this is shown by following the arguments presented in Refs [109, 110].

Consider a fluid that has an inner boundary S and an outer boundary Σ as shown in Figure B.1, where the velocity potential of the fluid is given by ϕ. Consider a time interval $t \in [t_0^-, t_1^+]$. Suppose the flow, which was at rest prior to t_0 is acted upon by a system of impulsive pressure $(-\rho_\infty \phi_0)$ at $t = t_0$ and by a system iof impulsive pressure $-(-\rho_\infty \phi_1)$ at $t = t_1$ so that the fluid is brought back to rest after time t_1. In summary:

Fluid is at rest prior to t_0.

Acted upon by $-\rho_\infty \phi_0$ at t_0.

Acted upon by $-\left(-\rho_\infty \phi_0\right)$ at t_1, so that

Fluid is brought back to rest after t_1.

The total time integral of the pressure is given by

$$\int_{t_0^-}^{t_1^+} p\,dt = \left(-\rho_\infty \phi_0\right) - \left(-\rho_\infty \phi_1\right) + \int_{t_0}^{t_1} p\,dt \tag{B.11}$$

From the Bernoulli equation, Eq (B.8) (Eq 2-13 from Ref [109]), we have

$$p = p_\infty - \rho_\infty \left[\frac{\partial \phi}{\partial t} + \frac{q^2}{2} + E\right] \tag{B.12}$$

Substituting Eq (B.12) into Eq (B.11), we have

$$\int_{t_0^-}^{t_1^+} p\,dt = -\rho_\infty \int_{t_0^-}^{t_1^+} \frac{\partial \phi}{\partial t} dt - \rho_\infty \int_{t_0^-}^{t_1^+} \frac{q^2}{2} dt + \text{const}[t_1 - t_0] \tag{B.13}$$

The fluid is at rest prior to the starting impulse at t_0 and after the final impulse at t_1; therefore

$$\int_{t_0^-}^{t_1^+} \frac{\partial \phi}{\partial t} dt = 0 \tag{B.14}$$

Consequently, Eq. (B.13) becomes

$$\int_{t_0^-}^{t_1^+} p\,dt = 0 - \rho_\infty \int_{t_0^-}^{t_1^+} \frac{q^2}{2} dt + \text{const}[t_1 - t_0] \tag{B.15}$$

Now, consider the resultant forces on the inner and outer boundaries by examining

the following integrals

$$\boldsymbol{F}_S = \iint_S \boldsymbol{n} \int_{t_0^-}^{t_1^+} p\, dt\, dS \quad \text{and} \quad \boldsymbol{F}_\Sigma = \iint_\Sigma \boldsymbol{n} \int_{t_0^-}^{t_1^+} p\, dt\, d\Sigma$$

Assertion: Both $\boldsymbol{F}_S$ and $\boldsymbol{F}_\Sigma$ are separately zero.

To prove this assertion, consider the following arguments. The fluid is at rest at an infinite outer boundary. Therefore, the fluid velocity tends to zero as the outer boundary is pushed to infinity, which implies

$$\iint_\Sigma \boldsymbol{n} \int_{t_0^-}^{t_1^+} p\, dt\, d\Sigma = -\rho_\infty \int_{t_0}^{t_1} \boldsymbol{n} \iint_\Sigma \frac{q^2}{2}\, d\Sigma\, dt \longrightarrow 0 \quad \text{as} \quad \Sigma \longrightarrow \infty \tag{B.16}$$

Also

$$\iint_\Sigma \boldsymbol{n} \int_{t_0}^{t_1} \text{const}[t_1 - t_0]\, dt\, d\Sigma = 0 \tag{B.17}$$

Furthermore, the overall process starts from a condition of rest and ends with a condition of rest; therefore, the resultant impulsive force exerted over the inner boundary must be zero. Equation (B.16) shows that the impulse force vanishes at the outer boundary; therefore

$$\iint_S \boldsymbol{n} \int_{t_0^-}^{t_1^+} p\, dt\, dS = 0 \tag{B.18}$$

This result implies that the left hand side of Eq (B.11) is equal to zero. Therefore,

combining with Eq (B.17), we obtain

$$\begin{aligned} 0 &= \iint_S \left[-\rho_\infty \phi_1 + \rho_\infty \phi_0\right] \boldsymbol{n}\, dS + \iint_S \boldsymbol{n} \int_{t_0}^{t_1} p\, dt\, dS + 0 \\ \Rightarrow \iint_S \boldsymbol{n} \int_{t_0}^{t_1} p\, dt\, dS &= \int_{t_0}^{t_1} F dt = \iint_S \left[-\rho_\infty \phi_1 + \rho_\infty \phi_0\right] \boldsymbol{n}\, dS = \boldsymbol{I}_{t_1} - \boldsymbol{I}_{t_0} \end{aligned} \tag{B.19}$$

Taking a time derivative on both sides of Eq (B.19), it follows that

$$\boldsymbol{F} = \frac{d\boldsymbol{I}}{dt} = \iint_S \boldsymbol{n}\, p\, dS \tag{B.20}$$

By an analogous argument, the moment is given by

$$\boldsymbol{M} = \frac{d\boldsymbol{I}_m}{dt} = \iint_S \boldsymbol{r} \times \boldsymbol{n}\, p\, dS \tag{B.21}$$

Appendix C: Implementation of Digital Filters in MATLAB

Digital filters are used to reduce or enhance certain aspects of a sampled, discrete time signal. A common application of digital filters is the selective retention or elimination of frequency content in a given signal. The filters are typically implemented as linear polynomials that are obtained as a weighted sum of the input and output signals.The coefficients in the polynomial, which correspond to the weights or filter coefficients, are determined based on the type of filter required.

Each operation of a filter on a signal is called a '*pass*' to signify that only certain frequencies are allowed to pass through. For instance, low (or high) pass filters imply that only frequencies that are lesser (or greater) than a specified value to pass through. Two types of filters, called forward and zero-phase, are relevant in the context of this study.

Forward Filters

A forward filter is implemented using an explicit relation between the input signal and the latest value of the output signal, as shown in Eq (C.1).

$$y_{filtered}(n) = \sum_{j=1}^{m_f+1} B_f(j) y_{unfiltered}(n-j+1) - \sum_{j=2}^{m_f+1} A_f(j) y_{filtered}(n-j+1) \qquad \text{(C.1)}$$

Due to the explicit nature of the forward filter, it is computationally inexpensive and can be implemented real time during a time stepping simulation. It is important to note that each pass through a forward filter introduces a reduction in magnitude and a phase shift between the input and output signals. In several applications, the phase errors introduced by the filters are undesirable, particularly when phase shifts introduced by the physical system are an important considerations. In such cases, zero phase filters, described next, are preferred.

Zero-Phase Filters

As the name indicates, zero-phase filters produce a zero phase difference between the input and output signals. These filters involve two passes through a forward filter as follows: First, using Eq (C.1) obtain y_1 as the filtered signal corresponding to y_{in}. Then define y_2 as follows:

$$y_2(j) = y_1(n+1-j) \qquad \text{for} \quad j = 1,2,\cdots,n \tag{C.2}$$

Next, using Eq (C.1) obtain y_3 as the filtered signal corresponding to y_2. Then $y_{filtered}$ is given as follows:

$$y_{unfiltered}(j) = y_3(n+1-j) \qquad \text{for} \quad j = 1,2,\cdots,n \tag{C.3}$$

In this implementation, the forward filter operates on the $y_{unfiltered}$ followed by an operation on y_2 which is the revered signal corresponding to y_1. Consequently, the phase shifts that appear due to each operation of the forward filter cancel each other. Therefore, $y_{filtered}$ has a zero phase difference with $y_{unfiltered}$.

Appendix D: Computational Expense of the Vortex Model

The computational expense of the unsteady aerodynamic model is an important consideration in aeroelastic calculations. For each wing section, the order of magnitude of the expense due to the various steps in the aerodynamic model employed in the current study are shown in Table D.1.

Terms	**Component**	**Expense**
QS vorticity		N_θ
Conformal mapping		$N_v + N_\theta$
Shed vorticity	Kutta condition	N_v
	Stagnation condition	N_v
Wake induced vorticity		$N_v N_\theta$
Inverse transform		$N_v + N_\theta$
Unsteady loads	Vortex Impulse method	$N_v + N_\theta$
	Bernoulli equation	$N_\theta + N_\theta^2 + N_\theta N_v$
Wake model	Initialize	N_v
	Vortex induced velocity	$n_{wksubit} N_v^2$
	Airfoil induced velocity	$n_{wksubit} N_\theta N_v$
	Update positions	N_v
	Misc calculations	$n_{wksubit} N_v$

Table D.1: Computational time requirements for various terms in the aerodynamic model

Terms that have highest order of magnitude are shown in Table D.2. It is evident that the wake model and the unsteady Bernoulli equation are the most expensive components of the aerodynamic model.

The computational expense for a wing that is divided into $N_{section}$ spanwise stations,

Terms	**Expense**
Wake model	$n_{wksubit}\left(N_v^2 + N_\theta N_v\right)$
Bernoulli equation (calc. of velocity potential)	$N_\theta N_v + N_\theta^2$
Wake induced vorticity	$N_v N_\theta$
Misc	$n_{wksubit} N_v$

Table D.2: Dominant contributions

is proportional to the following

$$N_{section}\left[n_{wksubit}\left(N_v^2 + N_v N_\theta\right) + N_\theta^2 + N_\theta N_v\right]$$

The above expression implies that increasing $N_{section}$ causes a linear increase in computational expense, whereas increasing N_θ has a quadratic effect.

BIBLIOGRAPHY

BIBLIOGRAPHY

[1] Pines, D. J. and Bohorquez, F., "Challenges Facing Future Micro-Air-Vehicle Development," *Journal of Aircraft*, Vol. 43, No. 2, March - April 2006, pp. 290–305.

[2] Mueller, T. J., *Fixed and Flapping Wing Aerodynamics for Micro Air Vehicle Applications*, Vol. 195, Progress in Aeronautics and Astronautics, published by AIAA, 2001.

[3] Aono, H., *A Simulation-Based Study of Flapping Flight Mechanisms in Insects*, Ph.D. thesis, Chiba University, Japan, 2008.

[4] Grasmeyer, J. M. and Keennon, M. T., "Development of the Black Widow Micro Air Vehicle," *39th AIAA Aerospace Sciences Meeting and Exhibit*, Reno, NV, 8-11 January 2001, pp. 1–9, AIAA Paper number 2001-0127.

[5] Ifju, P. G., Jenkins, D. A., Ettinger, S., Lian, Y., Shyy, W., and Waszak, M. R., "Flexible-Wing-Based Micro Air Vehicles," *40th AIAA Aerospace Sciences Meeting and Exhibit*, Reno, NV, 14-17 January 2002, pp. 1–14, AIAA Paper number 2002-0705.

[6] Moschetta, J., Bataille, B., and Thipyopas, C., "On Fixed-Wing Micro-Air Vehicles with Hovering Capabilities," *46th AIAA Aerospace Sciences Meeting and Exhibit*, Reno, Nevada, 7 - 10 January 2008, pp. 1–13, AIAA Paper number 2008-221.

[7] Bohorquez, F. and Pines, D. J., "Hover Performance of Rotor Blades at Low Reynolds Numbers for Rotary Wing Micro Air Vehicles," *2nd AIAA "Unmanned Unlimited" Systems, Technologies, and Operation- Aerospace, Land, and Sea Conference and Workshop and Exhibit*, San Diego, California, 15 - 18 September 2003, pp. 1–10, AIAA Paper number 2003-6655.

[8] Kroo, I. and Kunz, P., "Mesoscale Flight and Miniature Rotorcraft Development," *Fixed and Flapping Wing Aerodynamics for Micro Air Vehicle Applications*, edited by T. J. Mueller, Vol. 195, chap. 23, Progress in Aeronautics and Astronautics, published by AIAA, 2001, pp. 503–517.

[9] Ramasamy, M., Lee, T. E., and Leishman, J. G., "Flowfield of a Rotating-Wing Micro Air Vehicle," *Journal of aircraft*, Vol. 44, No. 4, 2007, pp. 1236–1244.

[10] Ramasamy, M., Johnson, B., and Leishman, J. G., "Understanding the Aerodynamic Efficiency of a Hovering Micro-Rotor," *Journal of the American Helicopter Society*, Vol. 53, October 2008, pp. 412–428.

[11] Lakshminarayan, V. K. and Baeder, J. D., "Computational Investigation of Micro Hovering Rotor Aerodynamics," *Journal of the American Helicopter Society*, Vol. 55, 2010, pp. 022001.

[12] Pornsin-Sirirak, T. N., Lee, S. W., Nassef, H., Grasmeyer, J., Tai, Y. C., Ho, C. M., and Keennon, M., "MEMS Wing Technology for a Battery-Powered Ornithopter," *The Thirteenth Annual International Conference on Micro Electro Mechanical Systems (MEMS 2000).*, IEEE, Miyazaki , Japan, 23-27 Jan 2000 2000, pp. 799–804.

[13] Zdunich, P., Bilyk, D., MacMaster, M., Loewen, D., DeLaurier, J., Kornbluh, R., Low, T., Stanford, S., and Holeman, D., "Development and Testing of the Mentor Flapping-Wing Micro Air Vehicle," *Journal of Aircraft*, Vol. 44, No. 5, 2007, pp. 1701–1711.

[14] de Clercq, K. M. E., de Kat, R., Remes, B., van Oudheusden, B. W., and Bijl, H., "Flow Visualization and Force Measurements on a Hovering Flapping-Wing MAV 'DelFly II'," *39th AIAA Fluid Dynamics Conference*, San Antonio, Texas, 22-25 June 2009, pp. 1–10, AIAA Paper number 2009-4035.

[15] Wood, R. J., "The First Takeoff of a Biologically Inspired At-Scale Robotic Insect," *IEEE Transactions on Robotics*, Vol. 24, No. 2, 2008, pp. 341–347.

[16] Sibiliski, K., Pietrucha, J., and Zlocka, M., "The Comparative Evaluation of Power Requirements for Fixed, Rotary, and Flapping Wings Micro Air Vehicles," *AIAA Atmospheric Flight Mechanics Conference and Exhibit*, Hilton Head, South Carolina, 20 - 23 August 2007, pp. 1–15, AiAA Paper number 2007-6498.

[17] Zhen, L. I. U. and Moschetta, J. M., "Rotary vs. Flapping-Wing Nano Air Vehicles: Comparing Hovering Power," *The European Micro Aerial Vehicle Conference and Flight Competition*, Delft, the Netherlands, 14 - 17 September 2009, pp. 1–7.

[18] Azuma, A., Azuma, S., Watanabe, I., and Furuta, T., "Flight Mechanics of a Dragonfly," *The Journal of Experimental Biology*, Vol. 116, 1985, pp. 79 – 107.

[19] Dudley, R. and Ellington, C. P., "Mechanics of forward flight in bumblebees: I. Kinematics and morphology," *The Journal of Experimental Biology*, Vol. 148, No. 1, 1990, pp. 19–52.

[20] Wakeling, J. M. and Ellington, C. P., "Dragonfly flight. II. Velocities, accelerations and kinematics of flapping flight," *Journal of experimental biology*, Vol. 200, No. 3, 1997, pp. 557–582.

[21] Willmott, A. P. and Ellington, C. P., "The Mechanics of Flight in the Hawkmoth Manduca Sexta: I. Kinematics of Hovering and Forward Flight," *The Journal of Experimental Biology*, Vol. 200, 1997, pp. 2705 – 2722.

[22] Fry, S. N., Sayaman, R., and Dickinson, M. H., "The Aerodynamics of Hovering Flight in Drosophila," *The Journal of Experimental Biology*, Vol. 208, No. 12, 2005, pp. 2303–2318.

[23] Liu, Y. and Sun, M., "Wing kinematics measurement and aerodynamics of hovering droneflies," *The Journal of Experimental Biology*, Vol. 211, No. 13, 2008, pp. 2014–2025.

[24] Zanker, J. M., "The Wing Beat of Drosophila Melanogaster. I. Kinematics," *Philosophical Transactions of the Royal Society of London. Series B, Biological Sciences*, Vol. 327, No. 1238, 1990, pp. 1–18.

[25] Altshuler, D. L., Dickson, W. B., Vance, J. T., Roberts, S. P., and Dickinson, M. H., "Short-amplitude high-frequency wing strokes determine the aerodynamics of honeybee flight," *Proceedings of the National Academy of Sciences of the United States of America*, Vol. 102, No. 50, 2005, pp. 18213–18218.

[26] Tobalske, B. W., Warrick, D. R., Clark, C. J., Powers, D. R., Hedrick, T. L., Hyder, G. A., and Biewener, A. A., "Three-Dimensional Kinematics of Hummingbird Flight," *The Journal of Experimental Biology*, Vol. 210, No. 13, 2007, pp. 2368–2382.

[27] Wootton, R. J., "Functional Morphology of Insect Wings," *Annual Review of Entymology*, Vol. 37, 1992, pp. 113 – 140.

[28] Daniel, T. L. and Combes, S. A., "Flexible Wings and Fins: Bending by Inertial or Fluid-Dynamic Forces," *Integrative and Comparative Biology*, Vol. 42, 2002, pp. 1044 – 1049.

[29] Combes, S. A. and Daniel, T. L., "Into thin air: contributions of aerodynamic and inertial-elastic forces to wing bending in the hawkmoth Manduca sexta," *The Journal of Experimental Biology*, Vol. 206, 2003, pp. 2999–3006.

[30] Singh, B. and Chopra, I., "An Aeroelastic Analysis for the Design of Insect-Based Flapping Wings," *48th AIAA/ASME/ASCE/AHS/ASC Structures, Structural Dynamics, and Materials Conference*, Honolulu, Hawaii, 23-26 April 2007, pp. 1–19, AIAA Paper Number 2007-1757.

[31] Shyy, W., Berg, M., and Ljungqvist, D., "Flapping and Flexible Wings for Biological and Micro Air Vehicles," *Progress in Aerospace Sciences*, Vol. 35, 1999, pp. 455 – 505.

[32] Platzer, M. E. and Jones, K., "Flapping Wing Aerodynamics - Progress and Challenges," *44th AIAA Aerospace Sciences Meeting and Exhibit*, Reno, Nevada, January 2006, pp. 1–19, AIAA Paper Number 2006-500.

[33] Sane, S. P., "The Aerodynamics of Insect Flight," *The Journal of Experimental Biology*, Vol. 206, 2003, pp. 4191 – 4208.

[34] Ansari, S. A., Żbikowski, R., and Knowles, K., "Aerodynamic Modelling of Insect-like Flapping Flight for Micro Air Vehicles," *Progress in Aerospace Sciences*, Vol. 42, 2006, pp. 129 – 172.

[35] Shyy, W., Lian, Y., Tang, J., Liu, H., Trizila, P., Stanford, B., Bernal, L., Cesnik, C., Friedmann, P., and Ifju, P., "Computational Aerodynamics of Low Reynolds Number Plunging, Pitching, ad Flexible Wings for MAV Applications," *48th AIAA Aerospace Sciences Meeting and Exhibit*, Reno, Nevada, January 2008, pp. 1–33, AIAA Paper No. 2008-523.

[36] Shyy, W., Lian, Y., Tang, J., Viieru, D., and Liu, H., *Aerodynamics of Low Reynolds Number Flyers*, Cambridge University Press, 2008.

[37] Shyy, W., Aono, H., Chimakurthi, S., Trizila, P., Kang, C.-K., Cesnik, C., and Liu, H., "Recent Progress in Flapping Wing Aerodynamics and Aeroelasticity," *Progress in Aerospace Sciences*, Vol. 46, No. 7, 2010, pp. 284 – 327.

[38] Wootton, R. J., Herbert, R. C., Young, P. G., and Evans, K. E., "Approaches to Modeling of Insect Wings," *Philosophical Transactions of the Royal Society of London B*, Vol. 358, 2003, pp. 1577 – 1587.

[39] Smith, M. J. C., "The Effects of Flexibility on the Aerodynamics of Moth Wings: Towards the Development of Flapping - Wing Technology," *33rd Aerospace Sciences Meeting and Exhibit*, Reno, NV, 9-12 January 1995, pp. 1–12, AlAA Paper number 1995-0743.

[40] Smith, M. J. C., "Simulating Moth Wing Aerodynamics: Towards the Development of Flapping-Wing Technology," *AIAA Journal*, Vol. 34, No. 7, 1996, pp. 1348 – 1355.

[41] Singh, B. and Chopra, I., "Dynamics of Insect-Based Flapping Wings: Loads Validation," *47th AIAA/ASME/ASCE/AHS/ASC Structures, Structural Dynamics, and Materials Conference*, Newport, Rhode Island, 1-4 May 2006, pp. 1–26, AIAA Paper number 2006-1663.

[42] Jongerius, S. R. and Lentink, D., "Structural Analysis of a Dragonfly Wing," *Experimental Mechanics*, Vol. 50, October 2010, pp. 1323–1334.

[43] Combes, S. A. and Daniel, T. L., "Flexural stiffness in insect wings II. Spatial distribution and dynamic wing bending," *The Journal of Experimental Biology*, Vol. 206, 2003, pp. 2989–2997.

[44] Barut, A., Das, M., and Madenci, E., "Nonlinear Deformations of Flapping Wings on a Micro Air Vehicle," *47th AIAA/ASME/ASCE/AHS/ASC Structures, Structural Dynamics, and Materials Conference*, Newport, Rhode Island, 1-6 May 2006, pp. 184–196, AIAA Paper Number 2006-1662.

[45] Chimakurthi, S., Cesnik, C., and Stanford, B., "Flapping-Wing Structural Dynamics Formulation Based on a Corotational Shell Finite Element," *AIAA Journal*, Vol. 49, No. 1, 2011, pp. 128–142.

[46] Aono, H., Kang, C.-K., Cesnik, C. E. S., , and Shyy, W., "A Numerical Framework for Isotropic and Anisotropic Flexible Flapping Wing Aerodynamics and Aeroelasticity," *28th AIAA Applied Aerodynamics Conference*, Chicago, Illinois, 28 June - 1 July 2010, pp. 1–25, AIAA Paper number 2010-5082.

[47] Hamamoto, M., Ohta, Y., Hara, K., and Hisada, T., "Design of Flexible Wing for Flapping Flight by Fluid-Structure Interaction Analysis," *IEEE International Conference on Robotics and Automation*, 2005, pp. 2253–2258.

[48] Hamamoto, M., Ohta, Y., Hara, K., and Hisada, T., "Application of Fluid-Structure Interaction Analysis to Flapping Flight of Insects with Deformable Wings," *Advanced Robotics*, Vol. 21, No. 1-2, 2007, pp. 1–21.

[49] Wu, P., Ifju, P., and Stanford, B., "Flapping Wing Structural Deformation and Thrust Correlation Study with Flexible Membrane Wings," *AIAA Journal*, Vol. 48, No. 9, 2011-2122, pp. 2136–2149.

[50] Baik, Y. S., Rausch, J. M., Bernal, L. P., Shyy, W., and Ol, M. V., "Experimental Study of Governing Parameters in Pitching and Plunging Airfoil at Low Reynolds Number," *48th AIAA Aerospace Sciences Meeting Including the New Horizons Forum and Aerospace Exposition*, Orlando, Florida, 4 - 7 January 2010, pp. 1–27, AIAA Paper number 2010-388.

[51] Liu, H. and Aono, H., "Size Effects on Insect Hovering Aerodynamics: An Integrated Computational Study," *Bioinspiration & Biomimetics*, Vol. 4, 2009, pp. 015002.

[52] Ramamurti, R. and Sandberg, W. C., "A Computational Investigation of the Three-dimensional Unsteady Aerodynamics of Drosophila Hovering and Maneuvering," *The Journal of Experimental Biology*, Vol. 210, 2007, pp. 881–896.

[53] Sun, M. and Tang, J., "Lift and power requirements of hovering flight in Drosophila virilis," *The Journal of Experimental Biology*, Vol. 205, No. 16, 2002, pp. 2413–2427.

[54] Trizila, P., Kang, C.-K., Visbal, M., and Shyy, W., "A Surrogate Model Approach in 2D versus 3D Flapping Wing Aerodynamic Analysis," *12th AIAA/ISSMO multidisciplinary analysis and optimization conference*, Victoria, British Columbia Canada, 10-12 September 2008, pp. 1–33, AIAA Paper number 2008-5914.

[55] Trizila, P., Kang, C.-K., Visbal, M., and Shyy, W., "Unsteady Fluid Physics and Surrogate Modeling of Low Reynolds Number, Flapping Airfoils," *38th AIAA fluid dynamics conference and exhibit*, Seattle, Washington, 23-26 June 2008, pp. 1–22, AIAA Paper number 2008-3821.

[56] Bisplinghoff, R. L., Ashley, H., and Halfman, R. L., *Aeroelasticity*, Addison Wesley Co., 1955.

[57] Polhamus, E. C., "A Concept of the Vortex Lift of Sharp Edge Delta Wings Based on a Leading-Edge Suction Analogy," Tech. Rep. NASA TN D-3767, National Aeronautics and Space Administration, 1966.

[58] Jones, M. A., "The Separated Flow of an Inviscid Fluid Around a Moving Flat Plate," *Journal of Fluid Mechanics*, Vol. 496, 2003, pp. 405–411.

[59] Pullin, D. I. and Wang, Z. J., "Unsteady Forces on an Accelerating Plate and Application to Hovering Insect Flight," *Journal of Fluid Mechanics*, Vol. 509, 2004, pp. 1–21.

[60] Shukla, R. K. and Eldredge, J. D., "An Inviscid Model for Vortex Shedding from a Deforming Body," *Theoretical and Computational Fluid Dynamics*, Vol. 21, 2007, pp. 343–368.

[61] Katz, J., "A Discrete Vortex Method for the Non-steady Separated Flow over an Airfoil," *Journal of Fluid Mechanics*, Vol. 102, 1981, pp. 315–328.

[62] Ansari, S. A., Żbikowski, R., and Knowles, K., "Non-linear Unsteady Aerodynamic Model for Insect-like Flapping Wing in the Hover. Part 1: Methodology and Analysis," *Proceedings of the I MECH E Part G Journal of Aerospace Engineering*, Vol. 220, No. 2, 2006, pp. 61–83.

[63] Zdunich, P., "Separated-Flow Discrete Vortex Model for Nano-Scale Hovering Flapping Wings," *26th AIAA Applied Aerodynamics Conference*, Honolulu, Hawaii, 18-21 August 2008, pp. 1–12, AIAA Paper number 2008-6245.

[64] Ansari, S. A., Żbikowski, R., and Knowles, K., "Non-linear Unsteady Aerodynamic Model for Insect-like Flapping Wing in the Hover. Part 2: Implementation and Validation," *Proceedings of the I MECH E Part G Journal of Aerospace Engineering*, Vol. 220, No. 2, 2006, pp. 169–186.

[65] Scott, M. T., *Nonlinear Airfoil-Wake Interaction in Large Amplitude Unsteady Flow*, Master's thesis, Massachusetts Institute of Technology, Cambridge, MA, August 1987.

[66] Benson, H. A. O., *Apparent-Mass and On-Board Circulation of Joukowski Airfoils and Cascades in Severe Unsteady Motion*, Master's thesis, Massachusetts Institute of Technology, Cambridge, MA, May 1989.

[67] Lam, C.-M. G., *Nonlinear Wake Evolution of Joukowski Airfoils in Severe Maneuver*, Master's thesis, Massachusetts Institute of Technology, Cambridge, MA, June 1989.

[68] Heathcote, S., Wang, Z., and Gursul, I., "Effect of Spanwise Flexibility on Flapping Wing Propulsion," *Journal of Fluids and Structures*, Vol. 24, No. 2, 2008, pp. 183–199.

[69] Wu, P., Ifju, P., Stanford, B., Sallstrom, E., Ukeiley, L., Love, R., and Lind, R., "A Multidisciplinary Experimental Study of Flapping Wing Aeroelasticity in Thrust Production," *50th AIAA/ASME/ASCE/AHS/ASC Structures, Structural Dynamics, and Materials Conference*, Palm Springs, California, 4-7 May 2009, pp. 1–19, AIAA Paper number 2009-2413.

[70] Singh, B., *Dynamics and Aeroelasticity of Hover Capable Flapping Wings: Experiments and Analysis*, Ph.D. thesis, University of Maryland, College Park, 2006.

[71] Mountcastle, A. M. and Daniel, T. L., "Aerodynamic and Functional Consequences of Wing Compliance," *Experiments in Fluids*, Vol. 46, No. 5, 2009, pp. 873–882.

[72] Lua, K. B., Lai, K. C., Lim, T. T., and Yeo, K. S., "On the Aerodynamic Characteristics of Hovering Rigid and Flexible Hawkmoth-like Wings," *Experiments in Fluids*, Vol. 49, No. 6, 2010, pp. 1263–1291.

[73] Agrawal, A. and Agrawal, S., "Design of Bio-inspired Flexible Wings for Flapping-Wing Micro-sized Air Vehicle Applications," *Advanced Robotics, 23*, Vol. 7, No. 8, 2009, pp. 979–1002.

[74] Hu, H., Kumar, A. G., Abate, G., and Albertani, R., "An Experimental Study of Flexible Membrane Wings in Flapping Flight," *46th AIAA Aerospace Sciences*

Meeting and Exhibit, Orlando, Florida, 5-7 January 2009, pp. 1–16, AIAA Paper number 2009-0876.

[75] Zhu, Q., "Numerical Simulation of a Flapping Foil with Chordwise or Spanwise Flexibility," *AIAA Journal*, Vol. 45, No. 10, 2007, pp. 2448–2457.

[76] Masoud, H. and Alexeev, A., "Resonance of flexible flapping wings at low Reynolds number," *Physical review. E, Statistical, nonlinear, and soft matter physics*, Vol. 81, No. 5, 2010, pp. 1–5.

[77] Du, G. and Sun, M., "Effects of wing deformation on aerodynamic forces in hovering hoverflies," *The Journal of Experimental Biology*, Vol. 213, No. 13, 2010, pp. 2273–2283.

[78] Chimakurthi, S. K., Tang, J., Palacios, R., Cesnik, C. E. S., and Shyy, W., "Computational Aeroelasticity Framework for Analyzing Flapping Wing Micro Air Vehicles," *49th AIAA/ASME/ASCE/AHS/ASC Structures, Structural Dynamics, and Materials Conference*, Schaumburg, Illinois, April 2008, pp. 1–23, AIAA Paper Number 2008-1814.

[79] Chimakurthi, S. K., Stanford, B. K., Cesnik, C. E. S., and Shyy, W., "Flapping Wing CFD/CSD Aeroelastic Formulation Based on a Co-rotational Shell Finite Element Formulation," *50th AIAA/ASME/ASCE/AHS/ASC Structures, Structural Dynamics, and Materials Conference*, Palm Springs, California, 4-7 May 2009, pp. 1–30, AIAA Paper Number 2009-2412.

[80] Gopalakrishnan, P., *Unsteady Aerodynamic and Aeroelastic Analysis of Flapping Flight*, Ph.D. thesis, Department of Mechanical Engineering, Virginia Polytechnic Institute and State University, Blacksburg, Virginia, 2008.

[81] Ho, S., Nassef, H., Pornsinsirirak, N., Tai, Y., and Ho, C., "Unsteady aerodynamics and flow control for flapping wing flyers," *Progress in Aerospace Sciences*, Vol. 39, No. 8, 2003, pp. 635–681.

[82] Aono, H., Chimakurthi, S., Wu, P., Sallstrom, E., Stanford, B., Cesnik, C., Ifju, P., Ukeiley, L., and Shyy, W., "A Computational and Experimental Study of Flexible Flapping Wing Aerodynamics," *48th AIAA Aerospace Sciences Meeting Including the New Horizons Forum and Aerospace Exposition*, Orlando, Florida, 4-7 January 2010, pp. 1–22, AIAA Paper number 2010-554.

[83] MSC. MARC, *Volumes A - D*, 2005.

[84] Bauchau, O. A. and Trainelli, L., "The Vectorial Parametrization of Rotation," *Nonlinear Dynamics*, Vol. 32, No. 1, 2003, pp. 71 – 92.

[85] Kane, T. R., Likins, P. W., and Levinson, D. A., *Spacecraft Dynamics*, Mc-Graw Hill Publications, 1983.

[86] Baruh, H., *Analytical Dynamics*, Mc-Graw Hill Publications, 1999.

[87] MSC. NASTRAN, *Reference Manual*, 2004.

[88] Bathe, K., *Finite Element Procedures*, Prentice-Hall Inc., 1996.

[89] Belytschko, T., Liu, W. K., and Moran, B., *Nonlinear Finite Elements for Continua and Structures*, Wiley & Sons Ltd., 2001.

[90] von Karman, T. and Sears, W. R., "Airfoil Theory for Non-Uniform Motion," *Journal of Aeronautical Sciences*, Vol. 5, 1938, pp. 379–390.

[91] Abbott, I. H. and von Doenhoff, A. E., *Theory of Wing Sections: Including a Summary of Airfoil Data*, Dover Publications, 1959.

[92] Karamcheti, K., *Principles of Ideal Fluid Aerodynamics*, John Wiley and Sons, Inc., 1966.

[93] Milne-Thomson, L. M., *Theoretical Aerodynamics*, Dover Publications, 1973.

[94] Saffman, P. G., *Vortex Dynamics*, Cambridge University Press, 1992.

[95] Press, W. H., Teukolsky, S. A., Vetterling, W. T., and Flannery, B. P., *Numerical Recipes in FORTRAN 77: The Art of Scientific Computing*, Cambridge University Press, 2nd ed., 1992.

[96] Gorelov, D. N., "Calculation of Pressure on an Airfoil Contour in an Unsteady Separated Flow," *Journal of Applied Mechanics and Technical Physics*, Vol. 49, No. 3, 2008, pp. 437–441.

[97] Katz, J. and Plotkin, A., *Low-Speed Aerodynamics*, Cambridge University Press, 2001.

[98] Bathe, K., Ramm, E., and Wilson, E. L., "Finite Element Formulations for Large Deformation Dynamic Analysis," *International Journal for Numerical Methods in Engineering*, Vol. 9, 1975, pp. 353 – 386.

[99] Chung, J. and Hulbert, G. M., "A Family of Single-Step Houbolt Time Integration Algorithms for Structural Dynamics," *Computational Methods in Applied Mechanics and Engineering*, Vol. 118, 1994, pp. 1 – 11.

[100] Lewis, R. I., *Vortex Element Methods for Fluids Dynamic Analysis of Engineering Systems*, Cambridge University Press, 1991.

[101] Sarpkaya, T., "Computational Methods With Vortices - The 1998 Freeman Scholar Lecture," *Journal of Fluids Engineering*, Vol. 111, 1989, pp. 6–52.

[102] Satyanarayana, B. and Davis, S., "Experimental Studies of Trailing-Edge Conditions on an Oscillating Airfoil at Frequency Parameters of Up to One," *AIAA Dynamics Specialist Conference*, San Diego, CA, 24-25 March 1977, pp. 1–23, AIAA Paper number 1977-450.

[103] Crighton, D. G., "The Kutta Condition in Unsteady Flow," *Annual Review of Fluid Mechanics*, Vol. 17, 1985, pp. 411–445.

[104] Ansari, S. A., *A Nonlinear, Unsteady, Aerodynamic Model for Insect-Like Flapping Wings in the Hover with Micro Air Vehicle Applications*, Ph.D. thesis, Department of Aerospace, Power and Sensors, Cranfield University, Swindon, England, September 2004.

[105] Peroomian, O., Chakravarthy, S., Palaniswamy, S., and Goldberg, U., "Convergence Acceleration for Unified-Grid Formulation Using Preconditioned Implicit Relaxation," *36th Aerospace Sciences Meeting and Exhibit*, Reno, NV, 12-15 January 1998, pp. 1–16, AIAA Paper number 1998-0116.

[106] Peroomian, O., Chakravarthy, S., and Goldberg, U., "A "Grid-Transparent" Methodology for CFD," *35th Aerospace Sciences Meeting and Exhibit*, Reno, NV, 6-9 January 1997, pp. 1–13, AIAA Paper number 1997-724.

[107] Trizila, P., Kang, C.-K., Aono, H., Visbal, M., and Shyy, W., "Fluid Physics and Surrogate Modeling of a Low Reynolds Number Flapping Rigid Flat Plate," *28th AIAA Applied Aerodynamics Conference*, Chicago, Illinois, 28 June - 1 July 2010, pp. 1–46, AIAA Paper number 2010-5081.

[108] Kang, C.-K., Aono, H., Cesnik, C. S., and Shyy, W., "A Scaling Parameter for the Thrust Generation of Flapping Flexible Wings," *49th AIAA Aerospace Sciences Meeting Including the New Horizons Forum and Aerospace Exposition*, Orlando, Florida, 4-7 January 2011, pp. 1–27, AIAA Paper nunmber 2011-1313.

[109] Ashley, H. and Landahl, M. T., *Aerodynamics of Wings and Bodies*, Addison-Wesley Publishing Company, Inc, 1965.

[110] Lamb, H., *Hydrodynamics*, Dover Publications, 6th ed., 1932.